2011

Application of Scanning Probe Microscopy for New Physical Measurements and Studies of Surface Chemical Reactions of Materials at the Molecular Level

Stephanie Loletha Daniels
Louisiana State University and Agricultural and Mechanical College, sdanie9@lsu.edu

APPLICATION OF SCANNING PROBE MICROSCOPY FOR NEW PHYSICAL MEASUREMENTS AND STUDIES OF SURFACE CHEMICAL REACTIONS OF MATERIALS AT THE MOLECULAR LEVEL

A Dissertation

Submitted to the Graduate Faculty of the
Louisiana State University and
Agricultural and Mechanical College
in partial fulfillment of the
requirements for the degree of
Doctor of Philosophy

in

The Department of Chemistry

by

Stephanie Loletha Daniels

B.S., Jackson State University, 2004
M.S., Jackson State University, 2006

May 2011

DEDICATION

This dissertation is dedicated to my mother, Delois Daniels, my sister, Melanie Daniels, nephew Darian Hearn, and to my family and friends who have been on this incredible journey with me. I sincerely thank you for your love and support.

ACKNOWLEDGEMENTS

This dissertation would not have been possible without the support, love and encouragement of many people. I thank GOD for giving me the strength to endure and see my dreams come true.

To my mother, Delois and my sister, Melanie, I cannot express my gratitude enough for your unwavering love, patience and support throughout this process. This work would not have been possible without you and for that reason; I am forever indebted to my family. Thank you for your encouraging words when I needed them most. Most of all, thank you for always believing in me.

I would like to thank my research advisor and mentor, Dr. Jayne C. Garno, for her guidance, patience, words of encouragement and belief in my abilities throughout my studies at Louisiana State University. I am grateful for the opportunity to have worked in your research group. Your mentorship has helped to shape me into the scientist I am today. I appreciate the valuable feedback and discussions with my committee members, Dr. Kermit K. Murray, Dr. Isiah Warner, Dr. Les Butler, and Dr. Georgios Veronis.

I am thankful to Dr. Darren Lytle, my supervisor at the U.S. Environmental Protection Agency in Cincinnati, OH. I appreciate your guidance during and after my internship. I would also like to acknowledge the staff and my colleagues at the EPA for making me feel at home while in Cincinnati.

Finally, I thank my colleagues in the Garno Research group, past and present. To Dr. Johnpeter Ngunjiri, Wilson Serem, Kathie Lusker and Dr. Zorabelle LeJeune, I greatly appreciate your friendship and I will always remember and cherish the great times we spent with each other.

TABLE OF CONTENTS

LIST OF TABLES

LIST OF FIGURES

LIST OF ABBREVIATIONS

Abbreviation	Name
3D	Three Dimensional
AC	Alternating Current
AFM	Atomic Force Microscopy
CS-AFM	Current Sensing Atomic Force Microscopy
DIC	Dissolved Inorganic Carbon
DPN	Dip Pen Nanolithography
EDS	Energy Dispersive Spectroscopy
FTIR	Fourier Transform Infrared Spectroscopy
kHz	Kilohertz
MFM	Magnetic Force Microscopy
MFRM	Magnetic Resonance Force Microscopy
MRI	Magnetic Resonance Imaging
MSM	Magnetic Sample Modulation
NEXAFS	Near Edge X-Ray Absorption Fine Structure
NRMRL	National Risk Management Research Laboratory
pA	Pico ampere
PDMS	Poly-(dimethylsiloxane)
PL	Particle Lithography
RMS	Root Mean Square
SEM	Scanning Electron Microscopy
SPL	Scanning Probe Lithography
SPM	Scanning Probe Microscopy

STM	Scanning Tunneling Microscopy
T	Tesla
XRD	X-Ray Diffraction
UHV	Ultra High Vacuum
US EPA	United States Environmental Protection Agency

ABSTRACT

Scanning probe microscopy (SPM) provides unique capabilities for surface visualization and measurements that reach atomic and molecular dimensions. My research focus is directed toward applying and developing new measurements for analytical and surface chemistry with SPM. Two distinct goals based on studies with atomic force microscopy (AFM) will be described within this dissertation. The primary goal was to develop and apply a new AFM imaging mode for ultrasensitive measurements of the superparamagnetic properties of proteins. Magnetic sample modulation (MSM)-AFM, has capabilities to investigate and map the magnetic response of nanomaterials with unprecedented spatial resolution. The second goal was to apply high resolution AFM to probe the scaling and magnitude of corrosion of copper surfaces as a function of selected chemical parameters.

Characterization of the magnetic properties of nanomaterials using a new AFM imaging mode will be described in the first part of the dissertation. Ferritin is a model nanomaterial for SPM studies because of the superparamagnetic iron-oxide (Fe_2O_3) core and ultra small dimensions of the protein, as described in Chapter 3. Periodic arrays of ferritin architectures were fabricated on surfaces and used as test platforms for measurements with magnetic sample modulation (MSM), for mapping the magnetic domains of ferritin are described in Chapters 4 and 5. The new MSM approach combines contact mode AFM with electromagnetic modulation of samples to measure the vibration and motion of nanomaterials. Proof-of-concept results demonstrate the capabilities for selective mapping of individual ferritin molecules through vibration of the superparamagnetic iron cores.

Corrosion by-products from copper plumbing that are released into tap water are known to impact water quality and are detrimental to consumer health. The second part of this dissertation (Chapter 6) presents results for surface changes caused by water chemistry

parameters typical of domestic water supplies. In this study, AFM was used to characterize nanoscale changes in surface morphology caused by chemical treatments at the earliest onset of copper corrosion as a function of pH, solution concentration and immersion intervals of copper substrates. Conclusions and future directions for the work of this dissertation will be summarized in Chapter 7.

CHAPTER 1. INTRODUCTION

Scanning probe microscopy (SPM) provides capabilities to resolve surface morphology as well as to acquire mechanical and physical measurements at the nanometer scale. Scanning probe microscopy refers collectively to methods that use a probe to scan line-by-line for mapping surfaces. The exquisite resolution and precision obtainable with SPM enables studies of molecular organization, self-assembly and chemical binding processes on surfaces. Phenomena that can be studied with SPM techniques include surface topography,[1, 2] measurements of adhesion,[3] chemical bond strength,[4, 5] nanoscale friction,[6] lubrication,[6, 7] electronic[8] and magnetic properties[9] and molecular manipulation.[10] The various modes of SPM can be accomplished at different temperatures and in different environments including ultra high vacuum (UHV) and ambient conditions in either air or liquids. The studies in this dissertation introduce a new approach for mapping and measuring the magnetic response of nanomaterials based on contact-mode atomic force microscopy (AFM) and magnetic sample modulation (MSM)[11] and the use of AFM to investigate surface reactions for corroding copper substrates exposed to certain designed water chemistries.[12]

1.1 Scanning Probe Microscopy

The first scanning probe microscopy mode, scanning tunneling microscopy (STM) was invented in 1981 by Binnig and Rohrer, earning a Nobel Prize.[13, 14] Conductive or semi-conductive surfaces can be imaged using STM with true atomic resolution. The later invention of AFM in 1986 by Binnig and Quate enabled molecular-level studies of non-conductive samples with unprecedented resolution.[15] For AFM imaging, a sharp probe is scanned across the surface to measure different types of forces between the tip and the sample.[16] Depending on the sharpness of the probe, AFM has been demonstrated to achieve molecular and atomic resolution.[17] Studies with AFM are not limited to imaging conductive samples, thus a broad

range of materials can be studied. The selection of an AFM imaging mode for characterization is based on the system being studied. In contact mode AFM, the probe is brought in contact with the sample and the laser deflection is monitored to provide surface topography information. When investigating loosely bound or biological systems with contact mode, the continuous interaction of the tip with the sample may damage and/or alter the material.[18, 19] To reduce the shearing forces between the tip and sample when imaging in contact mode, for investigations of delicate surfaces, tapping mode AFM is more suitable.[20, 21] When interrogating the surface with tapping mode, the cantilever is oscillated near its resonant frequency to maintain intermittent interaction with the sample.[22, 23] Imaging delicate samples such as DNA,[24, 25] RNA,[26] proteins[27, 28] and cells[29, 30] with AFM can be accomplished with minimal sample preparation to perform dynamic studies of conformational changes and molecular interactions in real time at the molecular level.[31]

1.2 Ferritin as a Model System for Scanning Probe Microscopy Characterizations

Ferritin is an iron storage protein found in humans, bacteria and plants.[32] Investigations of the surface assembly and nanopatterning of ferritin studied with AFM will be presented in Chapters 3, 4 and 5. Chapter 3 presents a contemporary review of SPM investigations with ferritin, entitled: "Ferritin as a model nanomaterial: Nanolithography and scanning probe microscopy studies."

Chapter 3 highlights the application of SPM for molecular-level studies of ferritin. The nanocage protein ferritin is a model nanomaterial due to its unique properties and exquisitely regular small dimensions. Several SPM modes have been applied to resolve molecular features, as well as for studies of mechanical, electronic and magnetic properties of ferritin. Well-defined nanostructures of ferritin have been prepared using approaches based on micro-contact printing, nanosphere lithography and scanning probe-based nanolithography. A range of metals and metal

oxides have been encapsulated within the core of ferritin for tailoring material properties at the nanoscale and will be discussed in Chapter 3. Ferritin also has promising potential for development of nanodevices.

1.3 A New Magnetic AFM Mode for Detecting the Vibrational Response of Nanomaterials

Chapters 4 and 5 present studies using MSM-AFM for characterizing the superparamagnetic properties of ferritin.[11] Ferritin molecules can be sensitively detected using MSM combined with contact mode AFM. To generate an oscillating magnetic field, an alternating current (AC) is applied to a solenoid placed within the base of the AFM sample stage. When a modulated electromagnetic field is applied to samples, ferromagnetic and paramagnetic nanomaterials are induced to vibrate. As a result, the ferritin samples will vibrate with corresponding rhythm and periodicity of the applied field. Changes in the phase and amplitude of the periodic motion of the sample are sensed with a *non magnetic* AFM tip to selectively map vibrating magnetic nanomaterials.

1.4. Characterization of the Superparamagnetic Properties of Ferritin Microstructures by Contact-mode AFM Combined with MSM

To address problems of self-aggregation with proteins on surfaces, nanolithography approaches can be applied to engineer surfaces with spatially well-defined structures. Micrometer scale patterning of proteins can be achieved using micro-contact printing,[33, 34] photolithography[35, 36] and capillary filling lithography.[37] In Chapter 4, capillary filling was used to create micropatterns of ferritin stripes using a poly-(dimethylsiloxane) (PDMS) stamp as a surface mold. In these experiments, this soft lithography method was used to fabricate test structures for magnetic measurements with MSM-AFM. Dynamic MSM-AFM protocols were developed using the ferritin microstructures as test platforms. Results in Chapter 4, showcase dynamic studies of the vibrational response of ferritin structures when the frequency and strength

of the electromagnetic field were changed. Systematic experiments were conducted using patterned structures of ferritin to test new protocols for dynamic MSM-AFM measurements.

1.5 Fabrication of Patterned Surfaces with Particle Lithography

To progress from micro to nano scale architectures, particle lithography can be used to pattern surfaces with nanometer dimensions. Chapter 6 demonstrates the use of particle lithography to produce ring nanostructures of ferritin with well-defined surface arrangements.[11] Particle lithography is based on the natural self-assembly processes of proteins and mesoparticles to produce exquisitely regular surface patterns with high throughput, as first introduced by Garno et al.[38] The spacing and surface coverage of protein patterns on surfaces is defined by the diameter of the mesospheres used as a structural template. Either rings or pores of nanopatterns can be formed by changing the protein-to-particle ratio, providing arrays of exquisitely uniform and regular ferritin nanostructures.[39, 40] Regularly spaced structures of proteins with precise and reproducible dimensions can be applied for multiple successive surface measurements at dimensions of tens of nanometers. The ring patterned nanostructures of ferritin were used as test platforms for MSM-AFM experiments.

1.6 Studying Copper Corrosion Phenomena at the Nanoscale with AFM

Unsafe levels of copper, due to the leaching of metal pipes, has motivated studies of the mechanism(s) of copper corrosion.[41-43] Studies of copper substrates exposed to synthetic tap water was examined with high resolution AFM as described in Chapter 6. Controlling corrosion is a major challenge for drinking water distribution facilities.[44, 45] Drinking water found at the tap, typically contains chemicals such as dissolved inorganic carbon (DIC), sulfate, chloride and chlorine.[46] Water treatment facilities also add inhibitors such as phosphate compounds or silicate to mitigate corrosion of metal pipes.[47-49] The influence of water chemistry and the addition of orthophosphate as a function of pH and time on the early stages of copper corrosion were studied

systematically using SPM. These corrosion studies were performed at the United States Environmental Protection Agency (USEPA) in Cincinnati, Ohio, under the supervision of Dr. Darren Lytle. The drinking water division of the National Risk Management Research Laboratory (NRMRL) was particularly interested in this research because the mission of the agency is to protect human health and the environment by establishing regulations and standards for public water supplies. The complex mechanism(s) of copper corrosion have been well studied at the macroscopic level, but not in detail at the nanoscale. During my research internship at the USEPA, my goal was to implement AFM for fundamental studies of surface corrosion.[12] To understand the influence of water chemistry on copper corrosion, new experiments were designed for nanoscale studies of surface changes caused by water qualities using AFM. In these investigations, synthetic water conditions were designed to mimic a range of chemical treatments commonly found in domestic water supplies.

Complementary surface characterizations of the copper samples were acquired with fourier transform infrared spectroscopy (FTIR), x-ray diffraction (XRD) and synchrotron near-edge x-ray absorption fine structure (NEXAFS) spectroscopy. These investigations were used to help elucidate the chemical composition of the copper surface. Details of laboratory protocols for the copper corrosion studies are discussed in Appendix A. Additional XRD data, scanning electron microscopy (SEM) and energy dispersive spectroscopy (EDS) of the structural composition and elemental analysis of deposits formed on the copper surfaces are presented in Appendices B-C. By combining approaches for qualitative and quantitative surface characterizations, we are working to develop a predictive molecular-level model for understanding the interplay between anions, salts, organic agents, DIC and pH for processes of surface corrosion and passivation.

1.7 Summary and Future Prospectus

Chapter 7 provides a summary and overview of the future directions for this research. Studies at the nanoscale interface show promise in multidisciplinary research, offering a wealth of opportunities for new investigations of chemical reactions and molecular interactions. As demonstrated within this dissertation, studies of fundamental reactions of surface bound molecules, including mechanisms and surface properties are valuable in areas of academic, industrial and government research. The use of micro and nano patterns of ferritin show promise in bioarrays and immunoarrays to study cell-protein and protein-protein interactions. It is with hope that the use of biomolecules such as ferritin will aid in the design of new chemical and biosensors devices with high sensitivity and accuracy. Further studies are currently being conducted to fabricate an array of individual ferritin molecules for more dynamic investigations of the protein with MSM-AFM. Studies have also begun using current sensing AFM to investigate the electron transport difference of corroding copper coupons without and with exposure to water qualities containing the inhibitor orthophosphate. Continuous research with SPM to elucidate the surface reactions of corroding copper surface will aid in the predication and modeling of the corrosion of metal pipes used for potable water. We anticipate that nanoscale research will define new directions in areas such as materials chemistry and bio-nanotechnology to give insight in fundamental interactions of materials.

CHAPTER 2. EXPERIMENTAL APPROACH: IMAGING PRINCIPLES AND MODES OF SCANNING PROBE MICROSCOPY (SPM)

2.1 History of Scanning Probe Microscopy

Over the last decade, scanning probe microscopy (SPM) techniques have become valuable tools for interdisciplinary research efforts, in chemistry, physics, engineering, life sciences, materials science, electrochemistry, polymer science, biophysics, nanotechnology and biotechnology. Since the invention of the first scanning tunneling microscope (STM) in 1981 by Gerd Binning and Heinrich Rohrer,[50] a family of scanning probe techniques have been developed for surface measurements. Atomic force microscope (AFM) was invented by Binning et al. in 1986.[1] For SPM measurements, a probe is scanned across a surface to acquire information about samples morphologies with nanoscale resolution. Topographic maps of materials can be acquired at the molecular or atomic level.[51] The ability to "feel" and "view" details at the atomic and molecular level has led to new discoveries and provided fundamental understanding of the role of structure for material properties.[52, 53] The lattice arrangement of atoms and molecules can be visualized with STM and AFM, to provide details of molecular and atomic vacancies and adatoms. Depending on the instrument set-up for SPM, information about tip-surface adhesion, magnetic forces, frictional forces, elastic compliance and sample conductance can be acquired using various AFM imaging modes. This chapter presents an overview of the operating principles for several AFM imaging modes used for the research in this dissertation. The fundamental principles and operation of contact mode, frictional force, and force microscopy, tapping mode, phase imaging, magnetic sample modulation and current sensing AFM are described.

For AFM, the tip is attached to the free end of a cantilever and is brought close to the surface. Attractive or repulsive forces resulting from interactions between the tip and the surface will cause bending of the cantilever, which can be detected. Experiments with AFM have been

demonstrated in air, liquid and vacuum environments for metals, semiconductors, non-conductive and biological samples.[54, 55] Size measurements and manipulation of materials may be accomplished from microns down to nanometer level. The capability of AFM to generate three dimensional surface profiles with minimal treatment of samples provide advantages over other imaging methods, which require staining, metallization or UHV environments. A list of common AFM imaging modes and set-up parameters are is provided in Table 2.1.

Operation for different SPM imaging modes will require certain changes to the instrument configuration, such as actuating the AFM tip or sample, or changes for the positional feedback. Depending on the imaging configuration, several different channels of information can be acquired simultaneously to enable mapping of material properties concurrently with surface topography. The nature of the sample, and the type of information to be acquired for the sample of interest will determine which imaging modes should be used. Rich information for the sample of interest can be obtained with the capabilities of more than 50 SPM imaging modes, such as elasticity, adhesion, conductivity, electronic properties and magnetic forces.[56] The main requirements for SPM studies are that the sample should be sufficiently flat and be attached to a surface to prevent detachment by the probe.

2.2 Basic Imaging Principle for SPM

The term *scanning force microscopy* (SFM) has also been used interchangeably to describe SPM imaging modes, because the imaging principle is often based on measurements of the force between a probe and the surface. There are three main categories of operation for SPM imaging modes: contact, non-contact and intermittent-contact or *tapping* mode. For contact mode, the tip is operated in continuous contact with the surface; whereas for non-contact modes, the tip is lifted a certain distance from the surface and measurements are acquired without

Table 2.1 AFM imaging modes.

SPM Imaging Mode	Year Invented/ Contributor	Feedback Mechanism	Parameter Measured	Probe Type	Ref.
Scanning tunneling microscopy (STM)	1981 G.Binning and H.Rohrer	changes in the magnitude of the tunneling current	surface profiles, morphology, changes in sample currents acquired side-by-side	metal wire	[13]
Contact-mode AFM	1986 G.Binning, C.F.Quate and C. Gerber	AFM tip deflection	surface profiles, morphology, height changes, frictional force measurements	Si/ Si_3N_4	[1]
Non-contact AFM	1987 Y. Martin	tip deflection, caused by attractive forces between the surface and probe tip held above the surface	surface topography	Si/ Si_3N_4	[57]
Magnetic force microscopy	1987 Y. Martin and H.K. Wickramasinghe	surface topography is retraced, positional control by AFM tip deflection	surface profiles, morphology, relatively long-range magnetic forces	magnetic coated probe	[58]
Electrostatic force AFM	1988 Y. Martin, D.W. Abraham and H.K. Wickramasinghe	a voltage is applied between the tip and sample, positional control by tip deflection	measures electrostatic forces between the surface and AFM cantilever	conductive metal coated probe	[59]
Kelvin probe AFM	1991 M. Nonnenmacher	scanned over a surface at a constant height in order to map the work function of the surface	composition and electronic state of the local structures on the surface of a solid	conductive metal coated probe	[60]
Tapping-mode AFM	1993 Q. Zhong	changes in the amplitude of tip oscillation	surface profiles, morphology, height changes, elastic response	Si/ Si_3N_4	[61]
Magnetic resonance force microscopy	1994 O. Zuger and D. Rugar	measures resonant frequency of the cantilever	detection of the magnetic spin of a single electron	magnetic coated probe	[62, 63]
Magnetic AC or MAC-mode	1996 W. M. Dougherty	magnetic field is used to drive a magnetically coated cantilever, maintain constant tip amplitude	surface profiles, morphology, height changes, elastic response, similar to tapping-mode AFM	magnetic coated probe	[64]
Current sensing AFM or Conductive probe AFM	1999 T. W. Kelley, E. L. Granstrom, and C. D. Frisbie	applies a voltage between the substrate and conducting tip	maps local conductivity along with topography	conductive metal coated probe	[65]
Magnetic sample modulation (MSM)	2009 J-R. Li, B.R. Lewandowski, S. Xu and J.C Garno	magnetic field drives sample actuation, positional feedback with deflection of an AFM tip	surface profiles, morphology changes in vibration amplitude and frequency	Si/ Si_3N_4 non-magnetic probe	[66]

touching the sample. With tapping mode, the tip is driven to oscillate and intermittently touch or *tap* the surface.

A major component of SPM instruments is the probe or tip that is used to interrogate the surface. Tips are usually made of silicon (Si) or silicon nitride (Si_3N_4) measuring 10 to 40 μm in width and 0.3 to 2μm in thickness. Tips can also be composed of metals, diamonds or carbon nanotubes.[67] The small sharp tip is attached to a cantilever with a reflective coating. The force constant and resonant frequency of the cantilever is selected according to requirements for the sample to be studied and imaging mode. For operation of the AFM, a laser beam is focused on the back of the cantilever with a diode laser. As the tip is raster scanned across the sample, changes in the position of the cantilever is monitored and detected with a position sensitive photodetector.[68] The basic instrument set-up is illustrated in Figure 2.1. Variations in the distance between the tip and the sample changes the deflection or oscillation of the cantilever. The distance is constantly corrected by an electronic feedback loop between the tip positioning system and a computer controlled piezoceramic element. The computer controller will adjust voltages applied to the piezoscanner to maintain a certain deflection or oscillation amplitude set-point. A 3-D image of topographical information is generated by plotting the z (vertical direction) correction signal from the feedback loop against the x and y plane. Characterization of surfaces with AFM have routinely demonstrated resolution of 1 nm or less in the lateral direction and 0.1 nm in the vertical direction.[69]

2.3 Contact and Lateral Force Modes of AFM

The first imaging mode demonstrated with AFM was contact mode.[1] For contact mode imaging, the tip is scanned in direct contact with the sample using a piezoceramic scanner. A feedback loop is used to maintain the initial deflection set-point for the force applied between the tip and sample.

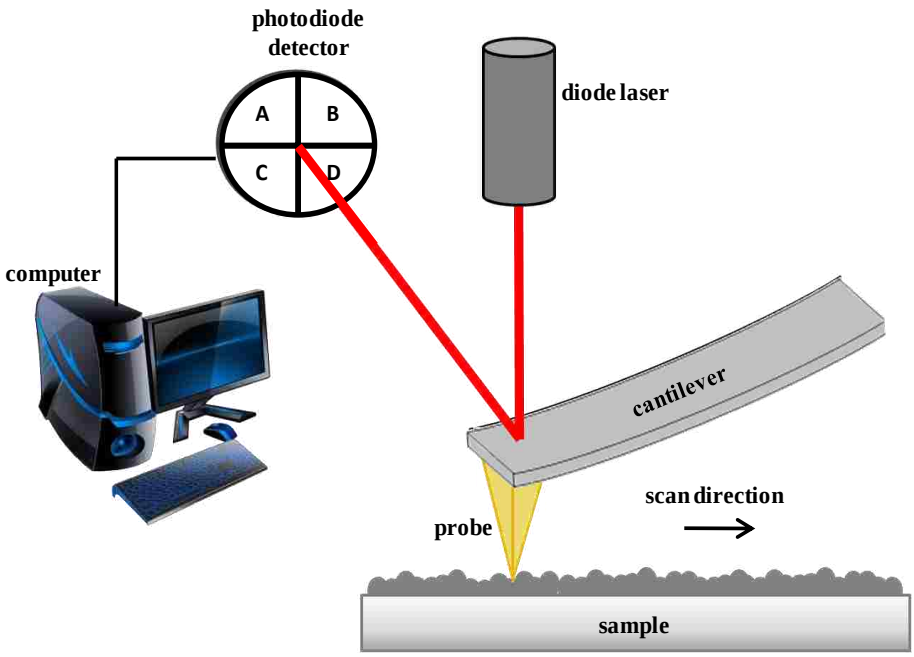

Figure 2.1 Basic instrument configuration for contact mode AFM.

Small changes in the deflection of the cantilever are mapped with the X-Y position of the tip to generate a 3-D topograph of the surface.[2, 70] The magnitude and direction of tip-sample interaction forces influence the deflection of the cantilever.[71]

For most samples, there is a hysteresis effect when the tip is scanned in different directions. At the nanoscale, it is difficult to produce a probe with perfect symmetry, and this can introduce directional differences for images. Likewise, samples may introduce anisotropic effects, for example caused by differences for the orientation of molecular headgroups. For this reason, the back-and-forth scans as the tip is rastered across the surface are sorted by direction, for example left-to-right and right-to-left images. These frames are not superimposed, and are displayed independently as separate image channels. Raw images show arrows to indicate the tip direction of each scan. The "fast" direction usually refers to the left-right direction of the linescan of the passing tip, whereas the "slow" direction refers to the tip motion for increments between linescans. Software enables control of the speed, line density, direction (left-to-right,

top-to-bottom, etc.) and sizes of the image frames. Typical scan rates are 0.5 to 2.5 μm/s with 256 or 512 linescans per image frame.

To detect the displacement of the cantilever, a laser is reflected off the back of the cantilever and collected with a quadrant photodiode detector, as shown in Figure 2.1. Changes when the laser is displaced vertically along the top (B-A) and bottom (D-C) positions result from the cantilever bending according to the topography of the sample. With contact mode imaging, topography, lateral force and force error images are simultaneously acquired for the sample. In lateral force imaging, the frictional forces between the tip and the sample produce torsional twisting of the AFM probe as it is scanned in contact with the surface. This movement of the tip is tracked by differences in the left (B-D) and right (A-C) quadrants of the detector.[72] The amount of twisting is caused by differences in frictional forces acting on the tip due to changes in the local surface chemistry of samples. Lateral force imaging is useful for investigating surface homogeneity to provide a sensitive map of variations in surface chemistry. Frictional force images and measurements can be acquired with nanoscale resolution by subtracting trace and retrace lateral force images. However, with molecularly-resolved views, the hysteresis differences between trace and retrace images can be substantial and usually require manual alignment and adjustment using surface landmarks.

With contact mode AFM, a third digital data channel known as “force error” is often acquired during experiments, but are rarely published. The force error channel is a digital representation of the changes in total signal for the feedback loop compared to a reference input. This digital error image is exquisitely sensitive to step edges and domain boundaries of surfaces but is not useful as a true representation of surface forces or properties. Raw data files for each SPM experiment for contact-mode AFM typically will contain results for six image frames, with trace and retrace images of topography, lateral force and force error channels.

A potential drawback of contact mode AFM can result from shear forces caused by movement of the tip, which can damage soft samples. Damaging of samples, can often be prevented by using ultra small forces (e.g. soft cantilevers with small spring constants) or by imaging in liquid media. An inherent advantage of SPM instruments is the exquisite control of ultra-small forces ranging from nano- to pico- Newtons. Typical force settings for AFM operation in air range from 1 to 10 nN/m, and from 0.05 to 1 nN/m for liquid media. The nature of the experiment determines what force and probe are appropriate, for interrogating the surface. A general strategy to minimize sample perturbation is to apply the minimum force necessary to tune in an image, additional force is unnecessary. Control scans to check if the tip is damaging the sample and monitoring the surface for changes after multiple successive scans.

2.3.1 Force Distance Measurements

Measurements of tip-sample interaction forces can be accomplished at the nanoscale using AFM force spectroscopy. For example, the force between the AFM tip and sample can be measured by collecting a force curve, which is a plot of cantilever deflection as a function of sample position along the z-axis. Force-distance measurements are most commonly based on a relationship based on Hooke's law between the force, **F**, and the cantilever deflection. The force is not measured directly, but rather is calculated by measuring the deflection of the lever, knowing the stiffness of the cantilever material. The Hooke's law relation used is **F = -kz,** where **F** is the force, **k** is the stiffness of the lever, and **z** is the distance the lever has bent.[73] Force-distance curves can be acquired with sensitivity of 1 pN.[74, 75] Studies of force-distance curves provide a deeper knowledge of the physics of contact. A typical force curve acquired in air for a sample of gold nanoparticles supported on mica is depicted in Figure 2.2.

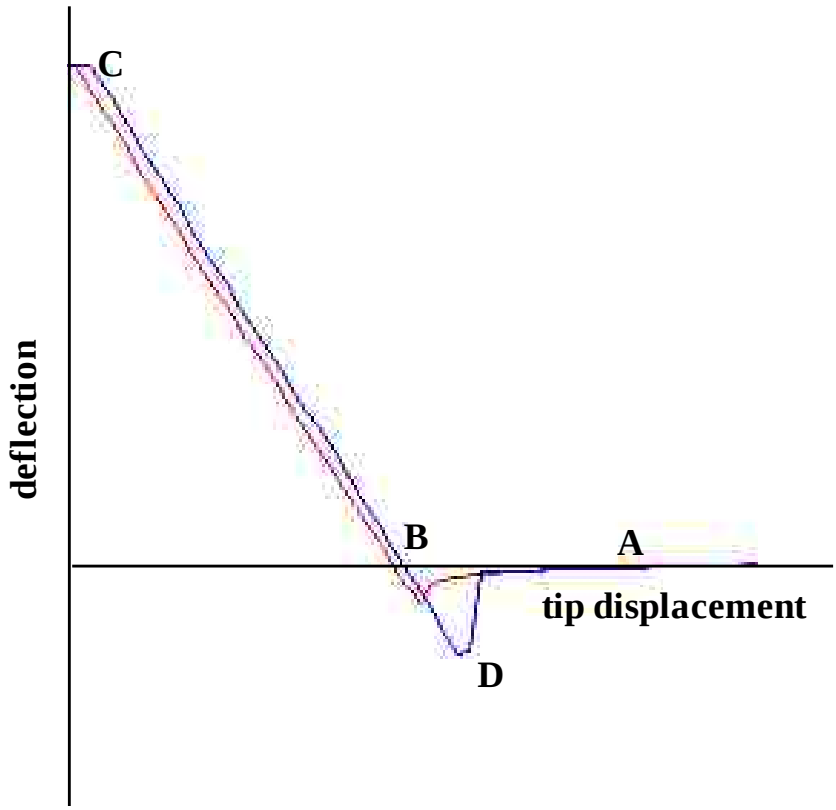

Figure 2.2 Example force-distance curve acquired in air.

The force-distance curve displays the tip displacement versus the deflection of the cantilever obtained for an individual approach-retreat cycle in air. Force spectroscopy studies usually report an average of hundreds of replicate measurements. When the tip is far away from the sample, there is no deflection of the cantilever and the interaction force can be considered negligible (label A). As the tip approaches the sample surface, the interaction with the sample causes the cantilever to bend upward due to the repulsive forces (label B), the bend will continue until tip "snaps in" into contact with the sample. This portion of the curve may be used to measure surface force such as van der Waals and electrostatic combined forces of attraction. As more force is applied to the tip, the deflection of the cantilever is increased to give the maximum deflection of the cantilever (label C). Upon retracting from the surface, the tip will overcome the adhesion forces and "jump-off" (label D) of the surface. This area of the curve can be used to estimate the surface energy or binding forces of materials. A standard protocol for AFM

experiments is to acquire several force-distance curves at the beginning and conclusion of sample analyses. These spectra are used for calculating the total imaging forces applied to samples for each experiment.

Molecular-level measurements of adhesion forces for biomaterials have become a significant research focus for biological AFM studies. Forces can be measured with pico-newton sensitivity for either specific or nonspecific protein-protein and protein-ligand interactions. For these measurements, a force versus distance curve is generated using an AFM probe that is coated with proteins such as antibodies, enzymes or desired functional groups. The coated probe is brought into contact with the sample and then withdrawn from the surface to generate a plot of the interaction forces as a function of tip displacement. For a typical approach-retreat measurement cycle, the bending of the cantilever is monitored as the probe is brought in and out of contact with the surface. The coated probe will adhere to the sample as it is withdrawn from the surface, often with multiple pull-off points for aggregate samples. The magnitude of this adhesive force can be calculated to provide estimates of molecular bond rupture forces. Changing the pH or ionic strength of the imaging buffer can be used to study changes for protein-protein interactions as a function of surface charge.

2.4 Tapping Mode and Phase Imaging AFM

Tapping mode AFM was invented to address the challenges of imaging delicate samples. For tapping mode, the cantilever is driven to oscillate near its resonance frequency to intermittently touch or *tap* the sample as the probe scan across the surface. The oscillation of the AFM tip eliminates much of the frictional and shearing forces, thus reducing damage or alteration of the surface.[76] The rapid motion of the oscillating tip prevents formation of transient interfacial bonds which cause the tip to adhere to the surface. The typical resonant frequency of tapping mode tips range from 160 to 300 kHz. Topography and phase data frames are acquired

simultaneously. For tapping mode AFM, the feedback loop maintains the oscillation of the tip at a specified constant amplitude setting selected by software parameters.[77, 78] As a general rule, a minimal setting is used to tune image resolution for soft and fragile samples. A larger amplitude is used for harder surfaces or polymers, to better tune the contrast for phase imaging. The amplitude of the tip oscillation changes with the AC voltage applied to the piezoactuator of the AFM nosecone for Agilent instruments. Changes in the voltages applied by the feedback loop to maintain a constant amplitude signal at the photodiode detector are translated into digital images of the sample topography.

Magnetic AC-mode or MAC-mode is an advanced version of tapping-mode, which enables more precise actuation of magnetically-coated AFM probes. The feedback loop and imaging principle of MAC-mode are identical to tapping-mode AFM, however the mechanism for tip actuation is quite different. Instead of driving the oscillation of an entire cantilever and chip with a piezoceramic element, for MAC-mode only the AFM tip is driven to oscillate by the influence of an external AC electromagnetic field. The magnetic field is generated by a wire-coil solenoid placed within the nosecone of the tip-holder assembly or underneath the sample stage. Operation for MAC-mode AFM requires probes that are manufactured with a top-side coating of a thin magnetic film.

Information about the adhesion, hardness or softness properties attributable to differences in surface chemistry of samples can be sensitively mapped with the phase images using tapping mode or MAC-mode AFM.[79] The phase image is influenced by three factors: the amplitude set point, topography and the material properties. These factors affect the phase channel because of changes in the interaction forces between the tip and the sample. The phase lag of the oscillation relative to the driving AC input signal is used to generate phase images, measured sensitively with a lock-in amplifier within the AFM controller. Phase images are obtained from mapping the

phase lag between the AC input signal which drives the oscillation with reference to the output signal detected due to cantilever oscillation. Phase imaging has become an indispensible tool for nanoscale chemistry studies for mapping compositional differences of polymer blends and organic thin films.[80-82]

2.5 Current Sensing AFM and I-V Measurements

Current sensing (CS-AFM) or conductive probe (CP-AFM) are used to measure and map conductive properties of samples at the nanoscale. For CS-AFM, topography and current frames are simultaneously acquired by applying a DC bias voltage to a conductive or semiconductive sample (Figure 2.3), and measuring the current with a conductive probe placed in contact with the surface. Surface topography frames are concurrently acquired with current maps for visualization of the transport properties of a sample.[65, 83] Applying a voltage between the substrate and conducting cantilever generates current flow, which is sensitively measured at the AFM tip using a preamp within the nosecone assembly. The change in current is used to construct a spatially resolved conductivity image. Changes in the polarity and magnitude of the bias voltage, controls the contrast for current images. Point measurements of current-voltage (*I-V*) characteristics can be measured for a programmed set of measurement points. Current measurements in the range of hundreds of femto- to nearly microamperes can be acquired with CS-AFM, by changing the size of the preamp located within the nosecone assembly. The CS-AFM imaging mode has been used to characterize conductive polymers,[84, 85] nanoparticles[86, 87] and metals.[88] Preliminary results with current sensing AFM are described in Chapter 6, in which CS-AFM was applied to measure nanoscale changes in the conductance of oxidized copper surfaces.

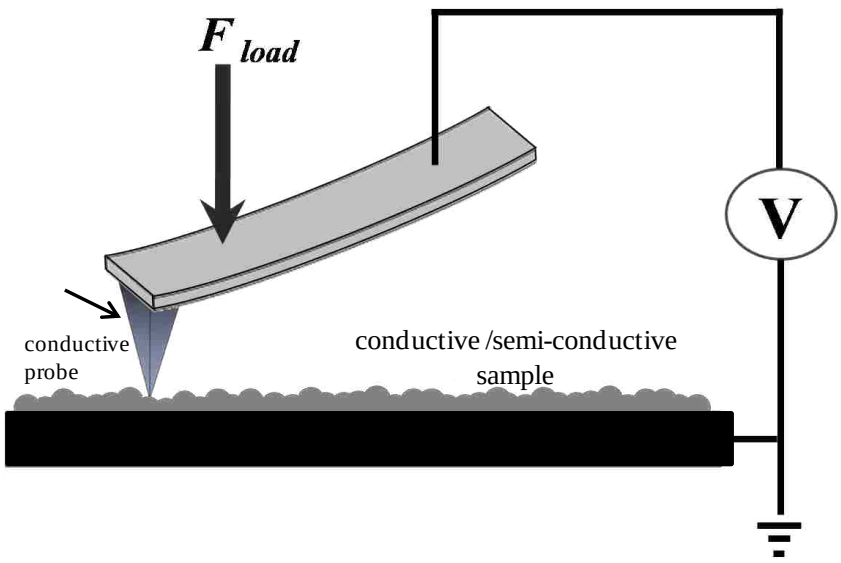

Figure 2.3 Current-sensing mode of AFM.

2.6 Magnetic Sample Modulation AFM

Magnetic sample modulation imaging (MSM-AFM) is a hybrid imaging mode, which is essentially a variation of force-modulation AFM with selective modulation of magnetic domains.[11, 66] For MSM-AFM, a *non-magnetic* AFM tip is operated using contact mode with a MAC-mode sample plate. An alternating electromagnetic field is used to drive selective modulation of magnetic or superparamagnetic nanomaterials. The detailed operating principle of MSM-AFM and experiments with an iron-containing protein, ferritin are discussed in chapters 4 and 5 of this dissertation. When an electromagnetic field is applied to samples, materials which are magnetic or superparamagnetic are driven to vibrate, and the vibrational motion of the samples can be detected using a non-magnetic AFM tip operated in contact mode. The strength, oscillation and flux of the magnetic field are controlled by selection of parameters for the AC current applied to the wire coil solenoid, which is located underneath the sample plate. With MSM, the periodic motion of the sample vibration can be tracked by changes in the deflection of the tip. Changes in the phase angle and amplitude of motion as the tip interacts with the vibrating sample are plotted as a function of tip position to create MSM phase and amplitude images.

Digital channels for the amplitude and phase components of the tip motion are obtained by directing an auxiliary output channel from the photodiode to the input of a lock-in amplifier, using the driving AC waveform as a reference signal.

The mechanical motion of the sample will produce differences in contrast exclusively for domains vibrating in response to the flux of the AC electromagnetic field. For MSM imaging, it is important to select a tip holder assembly (nose cone) and nonmagnetic tip to ensure that the tip is not driven to oscillate. With each set of MSM-AFM experiments, control spectra are acquired for the monitoring the tip trajectory as the AC field is ramped when the tip is lifted from the surface, and when the tip is placed at non-magnetic locations of the sample such as for bare areas of the substrate. A magnetized probe or tip assembly would respond directly to the flux of the magnetic field and thereby interfere with the tip-sample response. For the MSM set-up, the flux of the alternating magnetic field selectively induces mechanical vibration for magnetic nanomaterials on surfaces. The dynamic motion of the magnetic nanomaterials driven by an oscillating magnetic field is sensed by an AFM tip only when it touches the vibrating domains. Only magnetic domains vibrate, providing nanoscale selectivity.

2.7 SPM Imaging Modes Used for Dissertation Research

Further experimental details of the nature of the samples to be characterized, sample preparation methods, and specific operating parameters are presented within each chapter of the dissertation. A concise summary and overview of the imaging modes used for this dissertation is presented in Table 2.2. A typical AFM experiment will also include unpublished results of control samples, force-distance measurements and replicate image frames for multiple samples and experiments. These results are archived in the laboratory for future audit or reference for a period of at least five years.

Table 2.2 SPM imaging modes used for dissertation experiments.

Chapter	SPM Imaging Modes	Sample Description	Imaging Media
4	tapping and MSM	microstructures of ferritin on mica	air
5	tapping and MSM	nanorings of ferritin on mica	air
6	tapping	oxidized copper metal substrate	air
7	current sensing	oxidized copper metal substrate	air

CHAPTER 3. FERRITIN AS A MODEL NANOMATERIAL: NANOLITHOGRAPHY AND SCANNING PROBE MICROSCOPY STUDIES

3.1 Introduction

Although the physical, chemical and magnetic properties of ferritin have been well studied at the macroscopic level, investigations at the molecular-level with scanning probe microscopy offer promising opportunities for nanomedicine and nanotechnology. The iron storage protein ferritin has unique synthetic capabilities for encapsulating materials [89] and also has superparamagnetic [90] and electrical properties that can be used in nanodevice designs. The protein shell provides a biocompatible container for material synthesis for applications in magnetic resonance imaging (MRI), gene therapy, drug encapsulation, cell specific targeting and catalysis. [91, 92] Scanning probe microscopy (SPM) is well suited for imaging biological systems with advantages for studies in ambient or liquid environments with minimal sample preparation. Concurrently with molecularly-resolved topography images of protein structure, information of material properties can be acquired with nanoscale resolution, e.g. magnetic and conductive properties. As a molecular building block, strategies for nanolithography have been applied to direct the assembly of ferritin into designed arrangements for prototype nanodevices and surface test platforms.

3.2 Molecularly Resolved Characterizations of Ferritin and Apoferritin

Ferritin serves a major role for storage and regulation of iron in plants, bacteria and animals, acting as a buffer against iron deficiency or overload. [93, 94] The protein coat of ferritin (without iron) is referred to as apoferritin and holoferritin refers to the protein containing a mineral core. Ferritin is used for sequestering and storing toxic iron as an innocuous mineral of iron oxide. The overall protein mediated reaction for iron sequestration has been previously described. [95] Ferritin has a nearly spherical shape with a hollow shell encapsulating a cavity

which holds metal atoms. The protein cage within ferritin measures approximately 6-8 nm in diameter, and can encapsulate up to 4500 iron atoms. [96, 97] As a model nanomaterial, ferritin is a robust protein and is stable at temperatures up to 85 ^{o}C as well as for a relatively wide range of pH conditions. Ferritin was first described by Laufberger in 1937 who developed a purification method by crystallization with cadmium salts. [98] Since then, the crystalline structure of ferritin and biological functions have been extensively studied with x-ray diffraction (XRD), Mössbauer spectroscopy and electron paramagnetic resonance. [99, 100] The 450 kDa protein shell is composed of multiple four α-helix bundle subunits to form a symmetrical structure with a total dimension of 12 nm. [101] An overview of the structural details and dimensions for ferritin are shown in Figure 3.1, revealing the cage-like shell encapsulating a cavity for iron storage. As a framework for nanotechnology applications, extensive details of the chemistry, biological function and structure of ferritin have been previously published. [102-105]

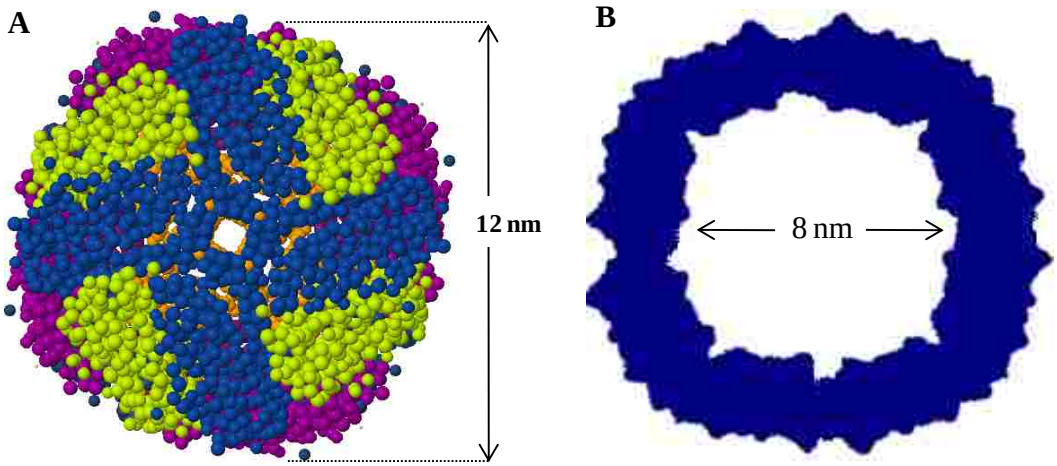

Figure 3.1 Structural models of ferritin. [A] Rasmol representation; [B] cross-section of the empty protein shell (apoferritin).

3.2.1 Electron Microscopy Studies

There has been a considerable amount of research performed with electron microscopy for studying ferritin.The quaternary structure of ferritin and the mineral core were first identified

by Farrant in 1954, using electron microscopy at the single molecule level.[106] Electron microscopy has provided detailed information about the dimensions and morphology of the core and shell of ferritin. Transmission electron microscopy (TEM), scanning electron microscopy (SEM) and scanning transmission electron microscopy (STEM) have been applied to visualize the morphology of ferritin. [107] These studies reveal that the iron within the core is encased by an outer shell of protein. For electron microscopy studies of ferritin, the sample is placed on a conductive metal grid for analysis in vacuum chambers. To view the protein coating, electron microscopy analysis requires pretreatment of samples, such as staining or fixing of the sample with conductive material.

3.2.2 Scanning Probe Microscopy Studies of Ferritin at the Molecular Level

New directions for molecular-level investigations have been advanced with SPM, which can be accomplished without sample treatment. Major advantages for SPM studies are the versatility for imaging conductive and non-conductive samples in ambient or liquid environments. Typically, SPM instruments are operated in either continuous contact or dynamic (intermittent) imaging modes. However, there are more than 30 SPM imaging modes which provide molecular-level maps of surface properties such as friction, conductivity, magnetism or adhesion, to provide further information beyond morphology characterizations.

The operating principle of SPM is based on scanning a small, sharp probe across the sample surface. Interactions between the probe and sample are measured and mapped with nanometer precision to construct a digital image. As the probe encounters regions of differing composition, the cantilever responds according to surface changes. For contact mode atomic force microscopy (AFM), a small force is applied as the tip is scanned in continuous contact with the sample surface. When imaging in liquids, contact mode AFM can provide exquisite resolution for protein samples.[108] Adsorption and assembly processes of ferritin have been

studied using SPM with a wide range of substrates, viewed with different imaging modes. The range of dimensions reported for ferritin depends on the nature of sample preparation as well as the type of ferritin used for experiments. Representative scanning probe studies with ferritin are summarized in Table 3.1, indicating the nature of the substrate for protein adsorption, the imaging media, reported range of measured dimensions as well as other complementary techniques used in combination with SPM.

With tapping mode AFM, the tip is actuated to rapidly oscillate as it is scanned across the sample. The tip is driven to intermittently touch the surface; in this way, stick-slip adhesion or shearing forces are minimized. Tapping mode AFM has become the method of choice for imaging soft and sticky surfaces or for fragile samples. [109] Additional information of sample softness or elastic properties can be acquired with the dynamic nature of tapping mode AFM, which alters the amplitude and phase trajectory of the tip motion. As the tip "taps" the sample surface, the cantilever oscillation is dampened as the tip touches the surface. Slight changes in the tip oscillation by the dampening effects can be used to map changes in surface stiffness or adhesion. An example AFM topography image of ferritin is presented in Figure 3.2 for a dilute solution of horse spleen ferritin (0.05 mg/mL) that was dried on the surface of mica(0001) and imaged using tapping mode AFM in air. Near spherical, random islands are observed throughout the surface within the 2×2 μm^2 area. For the z-scale of AFM topography images, typically the bright areas are taller and shorter features are dark in color. The individual molecules measured 6-10 nm in height, which corresponds with the range of values reported in Table 3.1. The dispersity of sizes reported for ferritin depends on how the sample is dried, the nature of the surface used for adsorption, as well as the amount of iron within the ferritin.

Table 3.1 Representative SPM studies of ferritin.

Mode	Ferritin Type	Substrate	Media	Reported Dimensions	Complementary Measurements	Year	Ref.
AFM contact	horse spleen	Si(100)	aqueous	12 nm	--	1992	[110, 111]
AFM tapping	horse spleen	gold	air	6.0 ± 1.1 nm	QCM, SPR, XPS	1997	[112]
AFM tapping	human spleen	silicon	air	6-24 nm	AFM force-distance	1999	[113]
AFM tapping	horse spleen	silane treated glass, HOPG	liquid *vs.* pH	10 - 13 nm	L-B, AFM force-distance	2000	[114]
AFM tapping	horse spleen	plexiglass	liquid	13.1 ± 0.3 nm	AFM force-distance	2000	[115]
AFM tapping	horse spleen	alkanethiol modified gold	air	12-13 nm	QCM cyclic voltammetry	2004	[116]
AFM contact	horse spleen	surfactant films on silicon	aqueous	--	SPR	2005	[117]
AFM tapping	horse spleen	gold	air	10 nm	conductive probe AFM	2005	[118]
AFM tapping	horse spleen	ITO, silane-modified silicon	air	12 nm	cyclic voltammetry	2005	[119]
AFM tapping	apo and holo forms	HOPG	air	8.4 ±1.5 nm	conductive AFM	2007	[120]
AFM tapping	horse spleen	thiol modified gold electrodes	air	11 ± 1.5 nm	cyclic voltammetry	2007	[121]
AFM tapping	horse spleen	gold	liquid	10 ± 2 nm	absorption kinetics	2008	[122]
AFM tapping	horse spleen and apoferritin	Au,TiO, NbO, Ta, SiO	air	--	QCM *vs.* pH	2008	[123]
AFM tapping	horse spleen	thiol-modified gold	air	6.5 ± 0.7 nm	--	2008	[124]
AFM tapping	horse spleen	SAM-modified gold electrodes	air	--	cyclic voltammetry	2008 2009	[125, 126]
AFM tapping	horse spleen	silane modified mica	air	7-10 nm	elastic modulus	2009	[127]
STM	human liver equine spleen	Au(111)	vacuum	10.3 ± 3.7 nm	STS	2010	[128]

ITO – indium-tin-oxide
HOPG – highly ordered pyrolytic graphite
SPR – surface plasmon resonance
QCM – quartz crystal microbalance
XPS – x-ray photoelectron spectroscopy
L-B – Langmuir-Blodgett apparatus
STS – scanning tunneling spectroscopy

The *apo* form of ferritin in which the iron core has been removed by chemical treatment has an overall diameter as small as 6 nm; whereas the *holo* form of ferritin which is fully saturated with iron has a diameter of 12 ± 1 nm. [120]

Beyond characterizing surface morphologies, the SPM investigations highlighted in Table 3.1 disclose new information about the selectivity of surface chemistries, [114, 119, 121, 124-126] adsorption kinetics, [122] surface charge, [111] elastic response, [127] as well as surface packing and arrangements. [114, 119, 126]

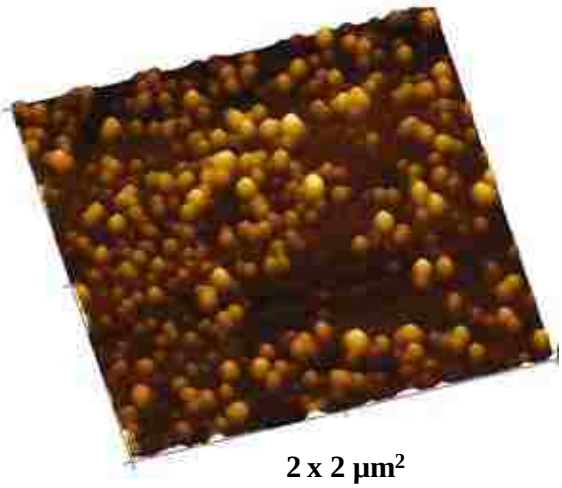

2 x 2 μm^2

Figure 3.2 Tapping mode AFM image of ferritin on mica. [A] topograph, 2×2 μm^2; [B] cursor profile for the line in **A**.

The kinetic studies were accomplished by counting the number of individual proteins that are attached to a selected area of the surface as a function of time and solution concentration. [122] Molecularly-resolved AFM studies provide detailed mechanistic insight for protein adsorption under physiological conditions that cannot be obtained by other techniques.

3.3 Lithography Approaches for Controlling the Surface Arrangement of Ferritin

Methods of surface patterning have been developed to take advantage of the multifaceted properties of ferritin for potential applications as surface-based sensors and bioelectronic devices. Several strategies have been applied to pattern ferritin molecules, which are most often based on the chemical selectivity of patterns to define the surface placement of the protein. A challenge for ferritin-based nanotechnology is to develop protocols to consistently produce nanostructures with regular features that are smaller than 100 nm, without the use of harsh chemical or physical conditions which could denature the protein. Retention of structure and function are essential for fundamental studies of protein-protein interactions and protein function. Examples of the diverse strategies used for patterning ferritin are presented in Table 3.2. One approach is to first pattern areas of a self-assembled monolayer (SAM) of organosilanes

Table 3.2 Examples of surface patterning studies with ferritin.

Year	Lithography Method	Nature of Surface Attachment	Nanopattern Dimensions (nm)	Surface	Ref.
2003	AFM anodic oxidation	selectivity of surface adsorption	600 nm oxidized line micropatterns	silane coated Si	[129]
2006	colloidal lithography	ferritin adsorption on thiolated nanostructures	disks, 100 nm diameter	gold/SiO_2	[130, 131]
2006	nanosphere lithography	selective affinity of recombinant ferritin to Ti patterns	ferritin adsorbed to 40 nm Ti triangle patterns	Ti nanopatterns on Si wafer	[132]
2006	e-beam lithography	electrostatic placement of individual ferritin molecules	circular patterns, 15 nm diameter	silanized SiO_2	[133]
2007	microcontact printing of thiol SAMs	ferritin adsorption by controlled potential electrolysis onto printed thiol SAM micropatterns	micropatterns, 25-100 μm	alkanethiol SAM/gold	[121]
2008	particle lithography	evaporative drying of an aqueous mixture of 500 nm silica mesospheres and ferritin	array of ring patterns, 500 nm diameter	mica, gold and glass	[40, 134]
2009	photolithography of organosilanes	electrostatic adsorption on silane nanopatterns	single molecules of recombinant ferritin on 32–45 nm disks	SiO_2	[135]
2010	DPN	direct writing of proteins with a protein coated AFM probe	dots, 50-500 nm diameter	gold, Al, Nb Si/SiO_x TEM grid	[136, 137]
2010	scanning probe-based local oxidation of organosilane SAMs	electrostatic adsorption of ferritin to organosilane SAM patterns	microlines, 10-15 nm width	Si(100) and organosilane SAMs	[138]
2010	block copolymer (BCP) micelle lithography	guided assembly of thiol-functionalized ferritin onto gold nanodots	arrays of single ferritins placed at 50 nm spacing on gold nanodots	gold	[139]
2011	AFM tip displacement	under force, the AFM tip was used to uncover an area of Si substrate coated with ferritin	500 × 500 nm square	silicon	[140]

DPN - Dip Pen Nanolithography

or alkanethiols, and then to use the spatial selectivity of surface headgroups to direct the adsorption of ferritin. Other approaches have been developed to directly place ferritin on surfaces in designed arrangements, such as direct-writing with dip-pen nanolithography (DPN).

3.3.1 Application of Scanning Probe Lithography to Produce Nanopatterns of Ferritin

Scanning probe lithography (SPL) methods have been successfully applied for patterning ferritin, by using an AFM probe as a tool for nanofabrication to generate protein patterns. Direct-writing of protein "ink" was accomplished with DPN [136, 137] as shown in Figure 3.3. The AFM tip was coated with a solution of ferritin and glycerol, for writing on clean substrates to form nanopatterns. Patterns are generated when the coated tip is placed in contact with the surface, by diffusion of protein "ink" molecules through a liquid meniscus. The size of the spot patterns is

controlled by the duration of time the tip is in contact with the surface. The example in Figure 3.3A demonstrates the precision of DPN for controlling tip placement and timing for reproducibly generating 100 dot nanostructures which measure 500 nm in diameter, regularly spaced at 1 μm intervals. After the nanopatterns have been generated with DPN, the surfaces can be characterized by AFM using a clean probe. The thickness of the nanostructures corresponds to a single layer of ferritin as shown in the cursor profile of Figure 3.3B. The height of the patterns measured 10 ± 2 nm, in close agreement with the expected dimensions of ferritin. A 3D view of an array of smaller ferritin nanostructures with diameters of 100 nm spaced at 500 nm intervals is shown in Figure 3.3C. Letter patterns were generated with DPN by translating the tip across the surface at a designated writing speed, as shown in Figure 3.3D. Depending on the experimental applications, further chemical steps can be applied after DPN. For example, the protein coating can be selectively removed while leaving the nanoparticles intact by either heat or UV/ozone treatment.

Another example of SPL with ferritin was accomplished with tip-directed anodic oxidation of Si surfaces. [129, 138] In these reports, the selectivity of patterned surfaces of Si and organosilanes was used to define the placement of ferritin nanostructures. Local surface oxidation is accomplished when a conductive AFM probe is placed in contact with the surface at elevated bias. When the bias voltage applied between the tip and surface is increased to certain threshold levels, the local area directly underneath the tip is locally oxidized. Local oxidation nanolithography can generate ultra small patterns on conductive or semiconductive substrates, with nanoscale precision. The size of patterns can routinely achieve dimensions of 10 nm or smaller. Patterns of ferritin are produced in a subsequent chemical step by immersing the substrates in protein solutions.

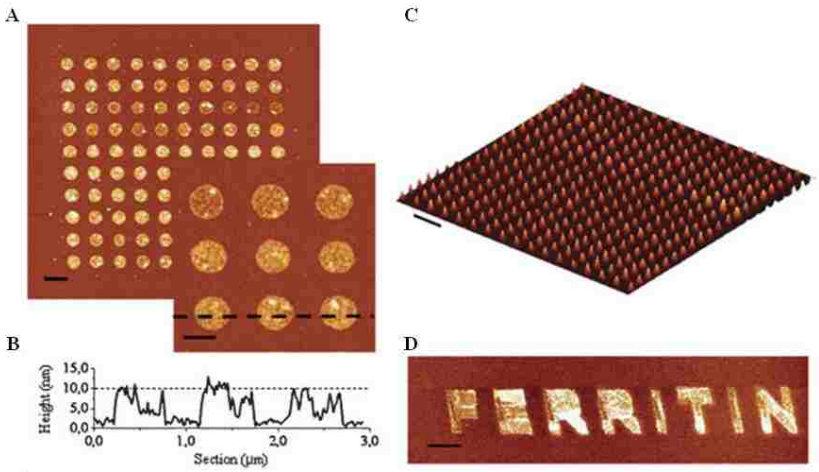

Figure 3.3 Nanopatterns of ferritin generated using DPN written on gold substrates. [A] AFM topograph of an array of 500 nm diameter dot patterns of ferritin (10×10 µm^2). [B] height profile for the inset in **A**. [C] array of 100 nm diameter dot patterns spaced at 500 nm intervals, scale bar measures 1 µm. [D] letter patterns, scale bar is 4 µm. Reprinted with permission from reference.[137]

The isoelectric point of ferritin is ~ 4.5, such that at pH values below 4.5 the protein is positively charged, while at higher pH ferritin is negatively charged. The pH conditions can likewise be used to define the selectivity of surface sites for electrostatic adsorption of ferritin to oxide patterns. This tip-based lithography method was also demonstrated by Yamamoto, et al., who applied elevated force to an AFM probe to displace ferritin to uncover a selected 500 × 500 nm^2 area of the substrate within a protein film. [140]

3.3.2 Nanostructures of Ferritin Produced by Surface Selectivity

Surfaces can be designed to present nanopatterns of reactive or adhesive terminal moieties for the selective adsorption of ferritin. Protein-patterning methods developed with SPM-based lithography have the limitation that each pattern is prepared individually, by relatively slow serial processes. To scale-up for patterning large areas with high throughput, other approaches such as microcontact printing, photolithography and electron-beam lithography have been applied for surface patterning of ferritin. For these methods, the selectivity of pre-patterned surfaces with designed headgroup chemistries defines the placement of ferritin. For example,

microcontact printing was used to prepare micropatterns of methyl- and amino- terminated alkanethiol SAMs (hexanethiol and 11-amino-undecanethiol) for selective adsorption of ferritin. [121] In a further step, ferritin attached selectively to the printed patterns through potential-controlled electrolysis. Placement of single ferritins on organosilane nanopatterns was reported by Kumagai, et al. using surfaces of SiO_2 patterned by electron beam lithography. [133] Designed distances between surface patterns provided a way to control electrostatic interactions to define the selectivity of ferritin binding from buffer solutions.

Nanopatterns of recombinant ferritin were produced by photolithography and genetic engineering. [135] Photo exposed areas of 3-aminopropyltriethoxysilane were generated on SiO_2 for electrostatic adsorption of mutant ferritin samples from solution. Genetic engineering was used to enhance the negative surface charge of ferritin. Another study used thiol-gold attachment for patterning ferritin by a method of block polymer (BCP) micelle lithography.[139] Nanostructures of gold dots were prepared by spin-coating a film of diblock copolymer micelles on silicon wafers or glass substrates to form a uniform array of cylindrical microdomains as a surface template. Gold(III) chloride hydrate ($HAuCl_4$) was then loaded into the micellar domains, and treatment with an oxygen plasma was used to remove the BCP film and to oxidize the gold salt to form gold nanostructures. Molecules with thiol functionalities were attached to ferritin as a tether to anchor the protein to individual gold nanodots. Thiol-modified ferritin attached selectively to the gold dots to generate an exquisite, high throughput array of individual ferritin molecules on the surface, mediated by thiol-gold chemisorptions. [139] The array of high density, periodic nanostructures of ferritin measured 11.2 ± 0.7 nm in diameter, with a distance between patterns of 48.4 ± 4.6 nm.

3.3.3 Patterning Ferritin Using Particle Lithography

Particle lithography with mesospheres can be used to directly guide the deposition of proteins on surfaces of mica, gold or glass. [40, 134] The natural self-assembly of monodisperse spheres provides an efficient, high-throughput route to prepare nanopatterns. Mesospheres of latex or silica assemble spontaneously into crystalline layers when dried on flat substrates, which supply a structural frame, template or mask for lithography. The template particles can be readily displaced with rinsing to disclose periodic arrays of nanopatterns on surfaces. For particle lithography with ferritin, the protein concentration and diameter of the mesospheres are tunable parameters to designate the size, interparticle spacing and surface coverage of nanopatterns. When an aqueous mixture of protein and mesoparticles is dried, proteins attach securely to surface areas surrounding the mesospheres as the liquid evaporates to generate nanostructures with a thickness corresponding to a single layer. An example of a single ring-shaped nanostructure of ferritin is shown in Figure 3.4. The circular arrangement of protein is produced within the meniscus area where the latex mesosphere masked the surface. A practical consideration for patterning proteins with particle lithography is that well-defined patterns can be generated from buffered conditions with minimal steps to produce large areas of high-density patterns.

An indirect approach for protein patterning based on particle lithography and electron-beam deposition was reported, where titanium nanostructures were generated as a spatially selective surface for subsequently anchoring recombinant ferritin to surfaces. [132] A film of polystyrene particles (150 nm diameter) arranged in a 2-D layer on a silicon wafer were used as a surface mask force-beam deposition of titanium.

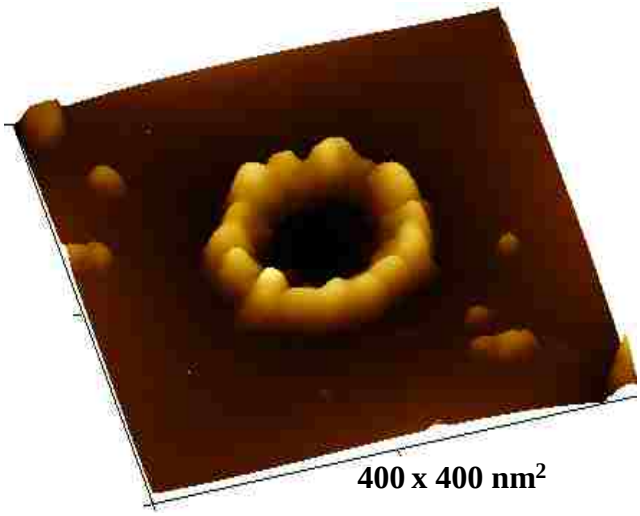

Figure 3.4 Ferritin molecules arranged in a ring on mica(0001), produced by particle lithography. Reprinted with permission from reference. [134]

The polystyrene spheres were removed by ultrasonication in dichloromethane to generate Ti nanopatterns in the shape of an equilateral triangule measuring 40 nm sides, with a thickness of approximately 3 nm. Peptides with a high affinity for titanium were genetically added to the N-terminus of the L-type subunit of horse-spleen ferritin. The genetically modified ferritin with Ti affinity peptides attached selectively to Ti nanopatterns after 1 h immersion in a buffer solution of recombinant ferritin. Each triangular pattern of Ti was so small that only four ferritins adsorbed to each pattern.

3.4 Physical Properties of Ferritin Investigated with AFM

As a model nanomaterial, certain properties of ferritin have been studied at the molecular level with SPM. The measurement modes of SPM can be used to study properties of biological materials, such as surface adhesion forces, mechanical stiffness, electrical conductance and magnetic properties.

3.4.1 Mechanical Properties – Force Spectroscopy Studies with Ferritin

Adhesion forces can be measured with pico-newton sensitivity using SPM, for either specific or nonspecific protein-protein and protein-ligand interactions. For these measurements, a

force versus distance curve is generated with a protein-functionalized AFM probe. The coated probe is brought into contact with the sample and then withdrawn from the surface to generate a plot of the interaction forces as a function of tip displacement. To obtain data for a typical approach-retreat measurement cycle, the bending of the cantilever is monitored as the probe is brought in and out of contact with the surface. The tip will stick to the sample as the probe is withdrawn from the surface, attributable to binding interactions between the probe and surface. The magnitude of this adhesive force can be calculated to provide estimates of molecular bond rupture forces.

Adhesion forces between a silicon substrate coated with an anti-ferritin antibody and a ferritin-coated probe were studied by Allen et al. to probe specific interactions between individual receptor-ligand pairs. [141] The same research group used ferritin-functionalized AFM probes to quantify and map unbinding forces between ferritin and anti-ferritin antibodies bound to a silicon surface. [142] The adhesive forces measured between ferritin-coated probes and anti-ferritin-coated surfaces were reported to range from 79-1,959 pN, with most of the measurements between 100 and 250 pN. A study with force-distance spectroscopy was reported by Wakayama et al. using a probe that was coated with anti-ferritin attached with an alkanethiol linker group. [143] In these studies, ferritin proteins were immobilized on the substrate and force-distance measurements were acquired in the presence or absence of detergent and a nonreactive protein. For these experiments, both the detergent and the nonreactive proteins were found to reduce the nonspecific force of adhesion for measurements of rupture force between antigen and antibody. Force-distance curves were measured for ferritin crystals in liquid by Mollica et al., who calculated the force required to remove or displace a single protein molecule to be 1.9×10^{-20} J/bond (12 kJ/mol). [144] Using AFM probes that were functionalized with the Fab fragment of an antiferritin antibody and substrates coated with ferritin the adhesion forces between the

probe and the ferritin-coated substrates was measured to be approximately 63 pN by Harada et al., which was attributed to a single unbinding event between individual antigen and antibody molecules. [145] The elastic modulus of ferritin was estimated by Zhang et al., using maps of force-distance measurements acquired in ambient air. [127] By acquiring force-distance profiles directly on the surface of ferritin samples attached to silanized mica substrates, the estimated value of the elastic modulus of individual ferritin was measured between 250-800 MPa.

3.4.2 Conductive Probe Studies with Ferritin

Current voltage (*I-V*) measurements can be acquired with SPM by placing a metal-coated probe directly on an individual molecule of ferritin and sweeping the sample voltage scan from negative to positive. An amplifier located near the probe is used to measure small currents at the tip. Electron flow has been characterized with current-voltage (I-V) spectroscopy for both iron-containing holoferritin and the iron-free form of apoferritin using conductive probe studies. [120, 128] For ferritin studies, the conductive iron core is encapsulated by a relatively nonconductive protein sheath, so the current travels from the conductive substrate through the protein coating and metal core to the metal SPM probe. A comparison of electron transport and junction resistance of apoferritin, holoferritin and cytochrome C samples on highly oriented pyrolytic graphite (HOPG) was conducted by Axford et al., under systematic conditions of applied force compression. [120] Differences were observed for the symmetry of I-V profiles, as well as the conductive nature of the proteins. Holoferritin was reported to be 5-15 times more conductive than apoferritin by Xu, et al. using conductive AFM. [118] With an applied sample bias of 1 V, the average electrical current through single holoferritin and apoferritin molecules measured 2.6 pA and 0.19 pA, respectively. Measurements of electronic band gaps for both holoferritin and apoferritin molecules as a function of temperature were accomplished with I-V spectroscopy using STM in vacuum. [128] The current-voltage response of holoferritin exhibited no band gap

response, which resembles metallic behavior. Differences were observed in the shapes of I-V spectra acquired at temperatures between 25 and 40 ^{o}C, and the band gaps were found to be narrower for holoferritin (-0.5 to 0.5 V) than for apoferritin (-0.56 to 0.91 V).

3.4.3 Magnetic Measurements of Ferritin Using SPM

For magnetic force microscopy (MFM), a magnetically coated probe is used to detect long range magnetic forces of surface domains. For MFM studies, the probe is used to obtain a line profile with an initial topographic scan, and then the probe is lifted from the surface for a second scan to measure magnetic forces. At a certain distance above the sample surface, "lift mode" is used to retrace the probe along the topography profile to construct an image of magnetic forces. During the second pass, the magnetic probe will either be attracted or repelled according to the polarity of the magnetic field of the sample, to provide a map of the forces of magnetic domains.

Since ferritin contains a superparamagnetic iron oxide core, it has not been a major focus for studies of magnetic properties with MFM. Only recently has it been demonstrated that MFM can be used to study the properties of superparamagnetic nanoparticles. Schreiber, et al., demonstrated the feasibility of MFM for detecting 10 nm superparamagnetic iron oxide nanoparticles by applying an in-plane external magnetic field to the sample. [146] A study using MFM to map the magnetic properties of aggregates and individual ferritin was reported by Hsieh et al. [147] Experiments with MSM were accomplished with the magnetic probe placed at distances ranging from 0-80 nm above the surface. The average magnetic moment (m_s) of single ferritin proteins was measured with MFM to be $6.76 \pm 0.61 \times 10^{-21}$ A m^2 which is comparable to previous studies, in which the m_s for individual 10 nm superparamagnetic iron oxide nanoparticles was estimated to be 2.5×10^{-19} A m^2 using measurements from a superconducting quantum interference device (SQUID).

A dynamic approach for AFM studies of superparamagnetic particles was introduced by Daniels et al., where the flux of an external AC electromagnetic field is applied to samples of ferritin. [134] Magnetic sample modulation (MSM) is a hybrid imaging approach based on AFM characterization of the vibrational responses of superparamagnetic nanomaterials using a standard, uncoated probe which is nonmagnetic. Rather than directly detecting the magnetic field of the sample, the motion and vibration of samples under the influence of a modulated AC electromagnetic field is used to detect magnetic responses. For MSM-AFM, an AC voltage is applied to the solenoid placed underneath the sample stage to produce an oscillating magnetic field. A *non-magnetic* probe tip is then used as a force and motion sensor to directly detect the vibration of magnetic material on the surface. Studies using MSM-AFM with ring nanostructures of ferritin were reported by Daniels et al., as shown in Figure 3.5. [134] The MSM-AFM imaging mode is selective for detecting nanomaterials that will vibrate in response to the flux of the AC electromagnetic field. Test platforms of ferritin produced using particle lithography were used for successive measurements at the nanoscale and exhibit interesting cooperative effects for magnetic coupling between adjacent nanoparticles.

Conventional contact mode AFM images without the influence of a magnetic field were acquired to obtain topography, amplitude and phase frames (Figures 3.5A-3.5C). The MSM amplitude (Figure 3.5B) and phase (Figure 3.5C) images do not show any contrast; this demonstrates that in the absence of the applied electromagnetic field, the ferritin molecules do not vibrate. Next, the same sample was scanned with the field turned on (Figures 3.5D-3.5F). The amplitude (Figure 3.5E) and phase (Figure 3.5F) images clearly map the locations of ferritin when the field is actuated.

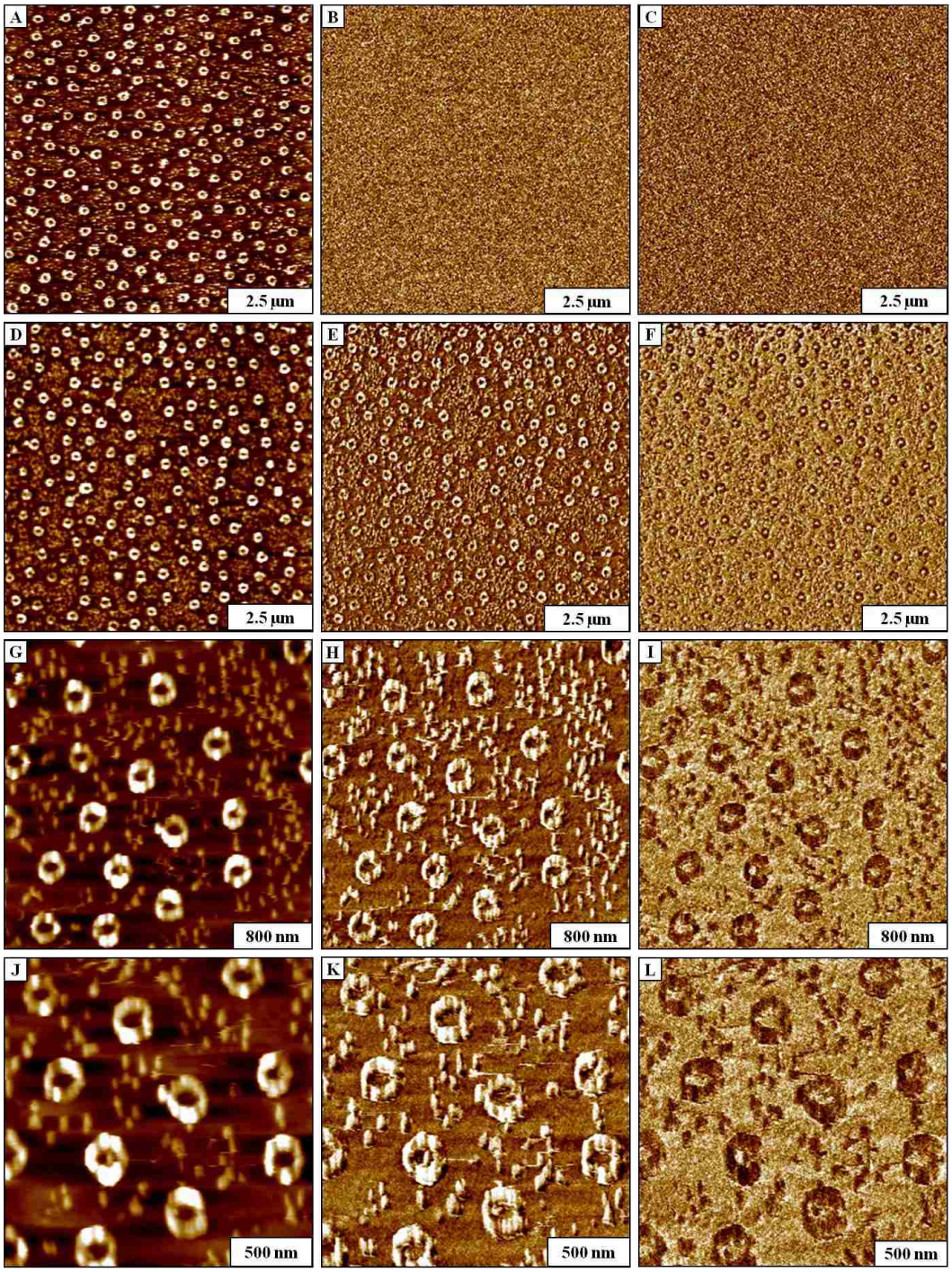

Figure 3.5 MSM-AFM images of ferritin nanopatterns. Contact mode AFM views without an applied magnetic field: [A] topography image (9×9 μm^2); [B] corresponding amplitude channel; [C] phase channel without an applied field. Images acquired with an applied AC field (0.2 T, 96 kHz): [D] MSM topograph (9×9 μm^2); [E] matching MSM amplitude and [F] MSM phase image for D. Higher magnification views: [G] zoom-in MSM topograph (3×3 μm^2); [H] MSM amplitude channel for **G**; [I] MSM phase image for **G**; [J] MSM topograph (2×2 μm^2); [K] MSM amplitude image for **J**; [L] MSM phase image for **J**. Reprinted with permission from reference. [134]

Changes in the phase and magnitude of tip oscillation relative to the driving signal are used to generate MSM images. Successive zoom-in views are shown in Figures 3.5G-3.5L. The locations of ring patterns and individual ferritin between the ring nanostructures are clearly detected in the MSM amplitude and phase images. These promising new results with MSM-AFM showcase new possibilities for AFM imaging of superparamagnetic nanomaterials such as ferritin, with unprecedented sensitivity.

3.5 Ferritin as a Vessel for Biomineralization

Because of the regular spherical shape and small dimensions of ferritin, the apoferritin cage has been used as a nanoreaction vessel to synthesize nanoparticles of varied composition. [148] Essentially, the cavity of ferritin and apoferritin provides an architectural framework for biosynthesis. The iron within ferritin can be removed via reductive dissolution to empty the core for encapsulation of other materials. Metals are introduced or released through the hydrophobic and hydrophilic molecular channels of the protein shell of ferritin. [102] Synthesis of nanoparticles within apoferritin has been successfully accomplished to generate a wide variety of nanomaterials, such as pure metallic Cu, [149] Ag, [150] Ni, [151, 152] Co, [152, 153] Pd, [154, 155] and Pt, [156] metal oxides of Co_3O_4 [157] and Mn_3O_4, [158] semiconductors such as CdS, [159, 160] CdSe, [161] ZnSe [162] and ferromagnetic alloys such as CoPt [163].

The cavity of apoferritin was used to synthesize nickel and chromium nanoparticles through a hydroxylation process using carbonate ions. [164] A new polymer-mediated route was introduced by Li et al. to deposit $CaCO_3$, $SrCO_3$, $BaCO_3$ and $CaPO_4$ particles within the cage. [122] Synthesis of ZnSe nanoparticles within the cavity of apoferritin was accomplished using a chemical reaction of tetraaminezic ion and selenourea. [165] The nanodot structures of ZnSe were then patterned on silicon and imaged with AFM. [166]

Several studies have demonstrated the synthesis of catalyst nanoparticles from apoferritin and ferritin for regulating the size and growth of carbon nanotubes. [167, 168] Nanotubes grown from catalytic nanoparticles derived from ferritin deposited on SiO_2 was demonstrated by Li et al. [169] Ferritin-based iron particles were used as catalysts by Durrer et al., to create individual single-walled carbon nanotubes by chemical vapor deposition, for studies with carbon nanotube-based field effect transistors. [170, 171] Ferritin was used to synthesize gold nanoparticles by Takagi et al., for studies of the growth mechanism of single-walled carbon nanotubes formed by vapor deposition on different substrates. [172]

3.6. Future Technologies Based on Ferritin-Derived Nanostructures

The uniform geometry and nanoscale dimensions of ferritin provide unique size-dependent properties that can be applied in electronic or optical devices. Heating or chemical treatments of surface films of ferritin can selectively remove the protein coating of ferritin to generate arrays of metal nanostructures for device applications. [173-175] For example, a combination of UV/ozone and ammonia plasma treatment of a ferritin monolayer was used to prepare ferrihydrite nanodots embedded within a SiN substrate by Hikono, et al., for application as a nanodot gate metal–oxide–semiconductor field effect transistor (MOSFET). [176] Biomineralized cobalt oxide Co_3O_4 nanodots synthesized in the cavity of ferritin were formed on Si substrates by Miura, et al., for studies as metal-oxide-semiconductor (MOS) memory devices. [177, 178] Next-generation MOS and gate memory designs require metal nanostructures with high surface density, uniformity and well-ordered arrangements that cannot be prepared by conventional lithography approaches. [179] Applications of ferritin in nanotechnology were recently reviewed by Yamashita, et al., for ferritin-based nanostructures. [175]

3.7 Conclusion and Prospectus

Ferritin is a unique nanomaterial with inherent properties attributable to size-dependent properties for emerging applications in bionanotechnology. The spherical protein cage and cavity of ferritin provide versatile capabilities for directed materials synthesis. Using ferritin as a model system, fundamental SPM investigations have been conducted to study magnetic, electronic and structural properties at the nanoscale. Because of the promising attributes of biocompatibility, processability and capability to prepare monodisperse, ordered crystals, studies with ferritin will facilitate future groundbreaking developments with device platforms for nanomedicine and nanotechnology.

CHAPTER 4. CHARACTERIZION OF FERRITIN MICROSTRUCTURES WITH MAGNETIC SAMPLE MODULATION AFM

4.1 Introduction

Fundamental understanding magnetic properties on nanomaterials may provide essential information and advancement in developing novel nanotechnology. We have developed a highly sensitive and selective imaging approach based on contact-mode atomic force microscopy (AFM) and magnetic sample modulation (MSM) for mapping and measuring the magnetic response of nanomaterials. Proof-of-concept results with characterizations of iron oxide nanostructures were previously reported by Li et al., for dimensions in the size range of 25-70 nm.[66] The goal of this research was to develop new protocols for MSM studies with AFM with nanoscale sensitivity. Ferritin is a nearly spherical protein consisting of a cage-like protein shell encapsulating iron oxide nanoparticles.[180] The inner cavity of ferritin can accommodate up to 4500 iron atom as ferrous ions (Fe^{2+}) which can be oxidized and stored inside as ferric ions (Fe^{3+}).[181, 182] The dimensions of ferritin molecules (10-12 nm) provide a model nanomaterial for testing the suitability of MSM-AFM for studying superparamagnetic nanoparticles. Microstructures of ferritin were prepared as model structures for characterizations with MSM-AFM. Ferritin is considered to be antiferromagnetic in its natural state, however, when exposed to an external magnetic field the Fe_2O_3 nanoparticles exhibit superparamagnetic behavior.[183, 184]

Microfabrication of biological samples is essential for the development of biosensors,[185, 186] protein microarrays[187, 188] and bioelectronic devices.[189, 190] With biomaterials such as ferritin, it is important to simulate physiological conditions during sample preparation and avoid using harsh chemical treatment with solvents or heat. For studies with ferritin, microstructured arrays were prepared with a soft lithography method referred to as capillary filling.[191, 192] The use of capillary filling for controlling the arrangement of biological systems have been demonstrated

previously with proteins,[193] cells[194, 195] and tissues.[196] Microfabricated poly(dimethylsiloxane) PDMS molds provide protein patterns with well-defined geometries on a variety of surfaces. With capillary filling, a PDMS mold with linear channels is placed in conformal contact with the substrate, the protein solution is placed at one end of the microchannels to form structures on the surface.

The purpose of this research was to provide proof-of concept for vibrating densely packed structures of ferritin with MSM. The microstructures of ferritin were used as a model test platform for studies with MSM-AFM. Magnetic sample modulation can directly detect vibrational responses of magnetic materials with nanometer sensitivity. Results are presented for micropatterns of ferritin using acoustic AC (tapping) mode AFM, phase imaging and MSM-AFM. Dynamic measurement protocols were developed with MSM-AFM to evaluate the superparamagnetic response of ferritin micropatterns with changing parameters of field strength and AC field frequency.

4.2 Experimental Approach

4.2.1 Materials and Reagents

Ferritin was purchased from MP Biomedical Inc. (Solon, OH). Hydrogen peroxide (30%) and sulfuric acid (95.5%) were acquired from Sigma-Aldrich (Saint Louis, MO). A commercially available Sylgard 184 PDMS kit containing the silicon elastomer base and the silicon elastomer curing agent was obtained from Dow Corning (Midland, MI). Round glass substrates, diameter 12 mm were obtained from Ted Pella Inc. (Redding, CA). The glass substrates were cleaned for 30 min by immersion in piranha solution, a 3:1 mixture of sulfuric acid and 30% hydrogen peroxide. (Caution: Piranha solution is highly exothermic and corrosive). Substrates were rinsed with deionized water and dried in air before use.

4.2.2 Procedure for Micropatterning Ferritin by Capillary Filling of PDMS Molds

To fabricate the microchannels, a PDMS stamp was placed firmly on a clean glass substrate. The steps for capillary filling are illustrated in Figure 3.1. A 10 µL drop of ferritin (0.02 µg/ml) was deposited at one end of the the stamp and the liquid allowed to dry for 24 h before removing the stamp. After drying, the stamp was removed from the substrate leaving intact features of ferritin micropatterns on the surface.

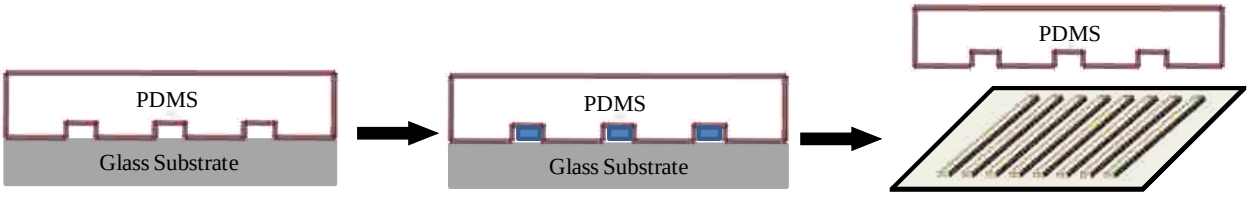

Figure 4.1 Approach for preparing microstructures of ferritin by capillary filling of PDMS molds.

4.2.3 Atomic Force Microscopy

Tapping mode AFM images of ferritin microstructures on glass were acquired using a Dimension 3100 scanning probe microscope with maximum scan area of 90 × 90 μm^2 (Veeco Metrology Inc., Santa Barbara, CA). Commercially available silicon nitride cantilevers with resonance frequencies ranging from 200 to 400 kHz, and spring constants 5 N/m were used for acquiring the results shown in Figure 4.2. The MSM-AFM data of the samples were obtained with an Agilent 5500 AFM system using Picoscan v5.3.3 software. Standard soft cantilevers, (MSCT-AUHW, Veeco Probe Store, Camarillo, CA) with spring constants ranging from 0.05 - 0.1 N/m were used for imaging with contact mode (Figure 4.3, 4.4 and 4.5). Images were acquired at ambient temperature in air. Digital images were processed with Gwyddion (version 2.9), which is open source software supported by the Czech Metrology Institute, freely available on the Internet (http://gwyddion.net).

4.2.4 Basic Principle of MSM-AFM

For MSM, a sample plate with a solenoid underneath the stage is used to produce an alternating magnetic field near the sample. MSM is operated in contact mode images, to located the features the samples were first acquired without applying a magnetic field. The imaging principles and sample plate used for MSM-AFM are shown in Figure 4.2. Next, the same area of the surface is re-scanned with the alternating electromagnetic field applied. The flux of the alternating magnetic field causes the magnetic domains in ferritin to vibrate. As the tip is scanned across the sample in contact mode, the movement of the protein causes the tip to vibrate when it touches the vibrating material. The mechanical motion of ferritin is sensitively detected by a soft nonmagnetic AFM tip.

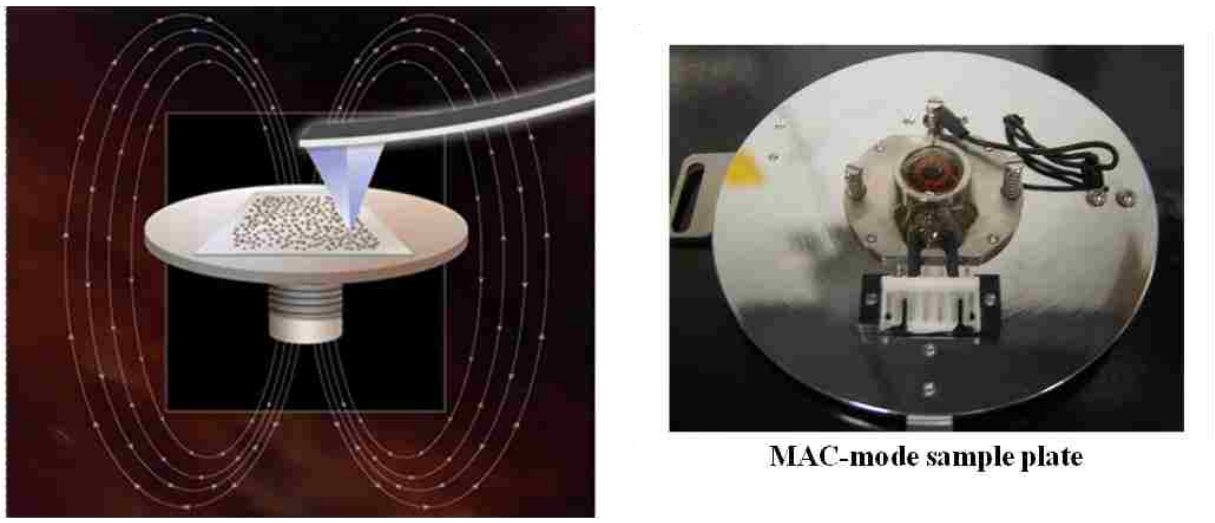

Figure 4.2 Instrument set-up for magnetic sample modulation AFM. (Left) Operating principle for MSM imaging. (Right) Photo of the underside of the sample stage used for MSM imaging.

Essentially, MSM is a variant of force modulation AFM with selectivity for actuating and characterizing magnetic nanomaterials. When an electromagnetic field is applied to samples, that exhibit magnetic behavior the magnetic domains are driven to vibrate. The vibration of the magnetic domain provides selective contrast for areas that are in motion. A lock-in amplifier is used to acquire the amplitude and phase images which correspond to the small deflection signals

in the tip movement with exquisite sensitivity. The tip interacts with the vibrating sample are plotted as a function of the position of the tip to create MSM phase and amplitude images. The differences displayed for images with and without an applied magnetic field are used to map areas of magnetic nanomaterials.

4.3 Results and Discussion

The experiments described in this chapter were designed to evaluate the suitability of capillary filling of PDMS molds for preparing microstructures of ferritin and show the applicability of MSM-AFM for characterizing ferritin. Results in this study provides new benchmarks for size scaling and sensitivity for measuring superparamagnetic properties with a new imaging mode of SPM. In addition, the instrument configuration for systematically changing parameters of AC field strength and modulation frequencies were tested for dynamic studies of the magnetic response of nanomaterials.

4.3.1 Characterization of Microchannels with Tapping-Mode AFM

Microarrays of ferritin were imaged with tapping mode AFM in air to characterize the dimensions of the microstructures that were fabricated with capillary filling. Dense, solid microlines of ferritin were produced as shown in Figure 4.3. Within the large scanned (Figure 4.3A) area, nine stripes are observed, with the width and spacing between stripes of 2 μm, respectively. The dark areas within the images are uncovered glass subtrate, the bright lines correspond to the ferritin filled structures. In the wide view, it is difficult to resolve individual ferritin molecules within the structures. Successive zoom in views of the arrays are displayed in Figures 4.3B and 4.3C. A cursor plot stretching across five of the patterns in Figure 4.3B measures the height of the features to be $17 \pm 2\ \mu m^2$.

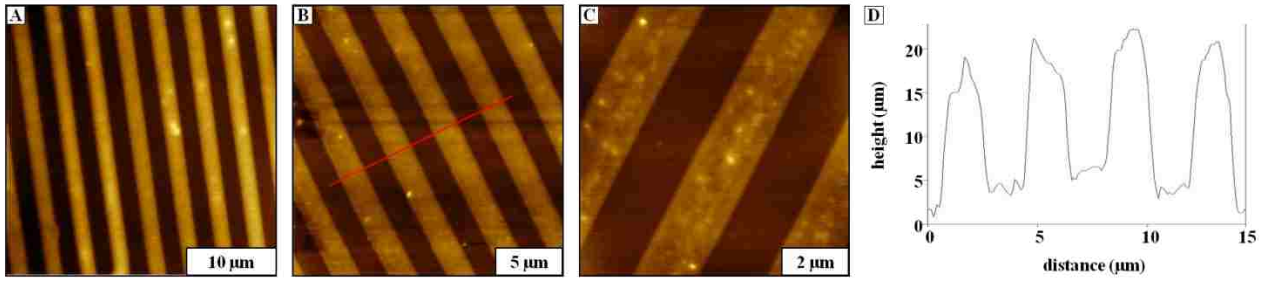

Figure 4.3 Microfabricated structures of ferritin produced by capillary filling. Topography views obtained with tapping mode AFM: [A] 30 × 30 µm^2; [B] 20 × 20 µm^2; [C] 8 × 8 µm^2; [D] cursor profile for the line **B**.

4.3.2 Characterization of Ferritin Microchannels with MSM-AFM

The fabricated microarrays of ferritin were used as test structures for studies with MSM-AFM. Results for micropatterns of ferritin characterized with MSM-AFM are displayed in Figure 4.4. Contact mode AFM imaging was used to characterize the morphology of the stripes and serves as a baseline view of the surface topography (Figure 4.4A). In this case, no external magnetic field was applied to the sample as the tip was scanned in continuous contact with the surface. The micropatterns of ferritin can be detected in the topography image, however, with the magnetic field off no features are visible in the simultaneously acquired amplitude and phase images. The same area was scanned when the AC field was activated at 0.02 T with a driving frequency of 167.5 kHz in Figure 4.4B (center row). By applying a magnetic field to the sample, MSM amplitude and phase channels show line patterns corresponding to the topography features. A zoom-in view of the sample reveals individual particles within the stripes of the microchannels, as well as a few individual particles on areas between the line patterns.

A requirement for MSM-AFM studies is that the sample be free to vibrate; if the materials are embedded in a matrix the possiblity of the sample vibrating is lessen. The soft protein sheath of ferritin encapsulates the metal nanoparticles of iron oxide and provides a robust attachment to the surface. However, the protein can still be driven to vibrate, even within densely packed multilayers of the microstructures.

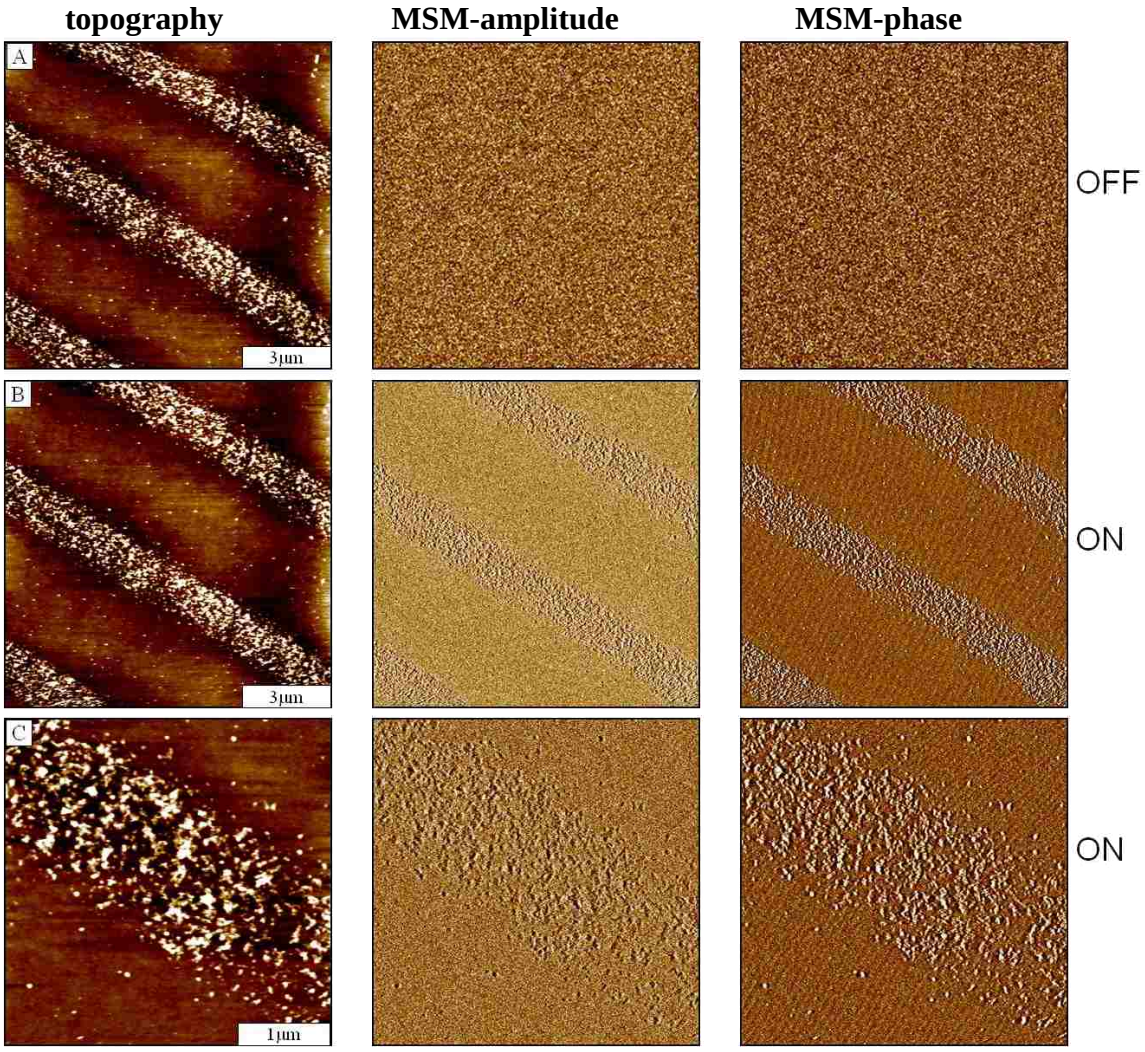

Figure 4.4 Vibrational response of ferritin microstructures mapped with MSM-AFM. [A] conventional contact-mode AFM images with the magnetic field turned off (top row); [B] with the AC electromagnetic field applied, contrast is visible in amplitude and phase channels (middle row); [C] zoom-in view of a single stripe with the magnetic field turned on (bottom row).

4.3.3 Dynamic MSM-AFM Protocols for Characterization of Ferritin Microchannels

The vibrational response of ferritin as a function of applied electromagnetic field is demonstrated in Figure 4.5. In this experiment, the frequency was kept constant at 167.5 kHz and the electromagnetic field was varied at 0.05, 0.50 and 1.0 T to evaluate the change in response. Arrows placed to the right of the MSM phase image indicate the changes in the applied magnetic field. At higher field strength, more structural details are apparent in the MSM frames, evidencing that a greater density of protein is driven to vibrate. In the MSM amplitude image,

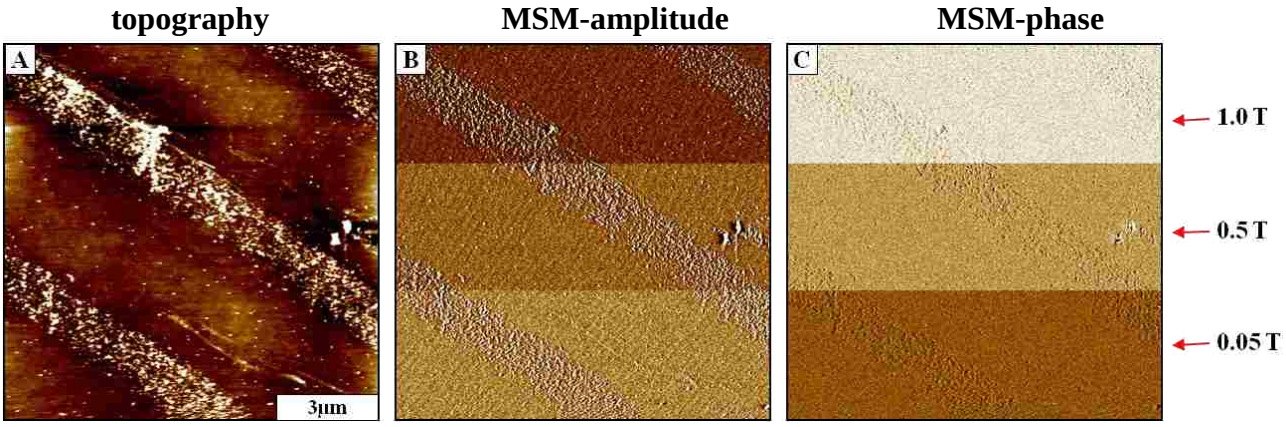

Figure 4.5 Dynamic protocols acquired by varying electromagnetic field strength within a single image using MSM-AFM. Simultaneously acquired frames of [A] MSM contact-mode topograph; [B] MSM amplitude view; [D] MSM phase image.

distinctly sharper contrast is observed as the field strength was successively increased (Figure 4.5B). As the field strength increased from 0.05 T to 0.5 T to 1.0 T corresponding changes were detected in the amplitude image, indicating changes in sample vibration. However, the microchannels of ferritin are faintly visible with slightly changes in the MSM phase image (Figure 4.5C).

Studies of the vibrational response of ferritin were acquired *in situ* with MSM-AFM at a constant applied magnetic field strength of 1.5 T, obtained within a single image with discrete changes of the driving frequency (Figure 4.6). As the driving frequency was successively increased from 118 to 205.6 kHz, changes in contrast are detected for the MSM amplitude and phase image. When the driving frequency was changed from 118 kHz to 141 kHz to 171.5 kHz and finally 205.6 kHz the features in the MSM amplitude frame in Figure 4.6B became progressively sharper at higher frequencies. The driving frequencies selected for image acquisition in Figure 4.6 are displayed in Figure 4.6D. The shapes of the patterns as well as the individual particles dispersed between the microstructures are clearly apparent in the topography image and are easily distinguishable in the MSM amplitude and phase images.

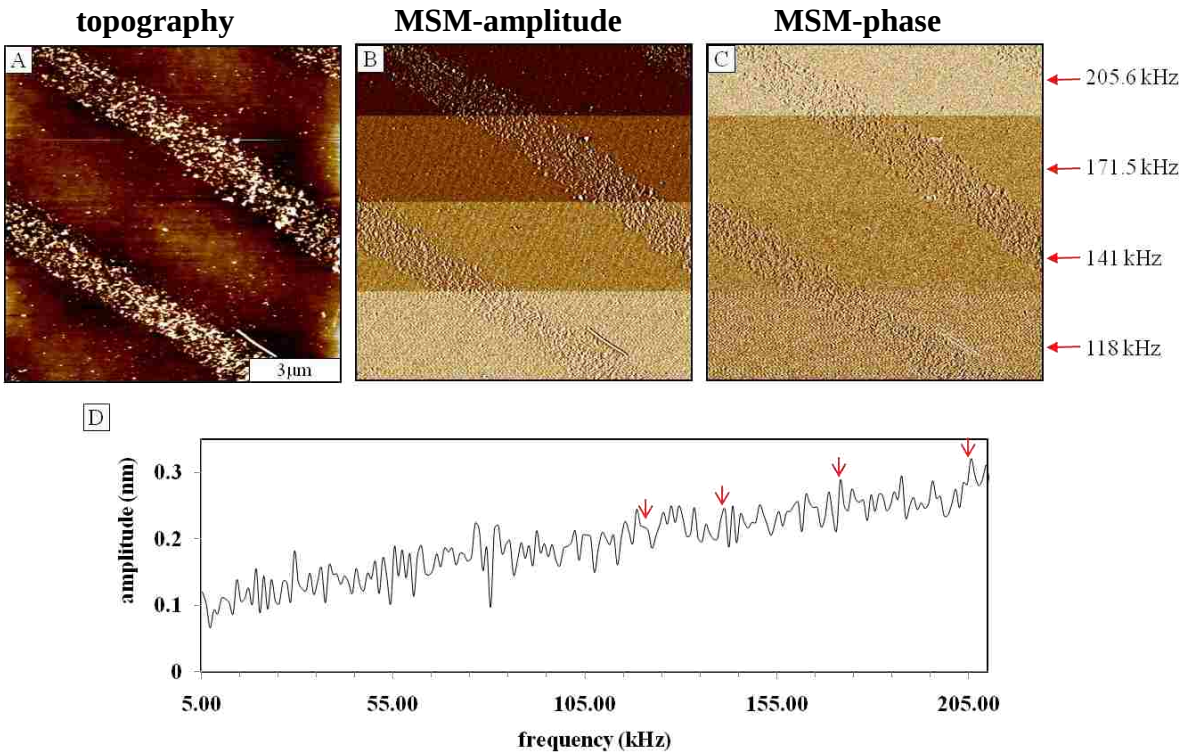

Figure 4.6 Successive changes for MSM-AFM images with incremental changes in the driving frequency of the sample. [A] MSM contact mode topography image; [B] corresponding MSM amplitude channel; [C] MSM phase image; [D] frequency profile.

4.4 Conclusion

Microstructures of ferritin were prepared on glass surfaces using a method of capillary filling of PDMS molds. The fabricated microstructures were used to evaluate the imaging and detection limits of MSM. In summary, new dynamic measurements have been developed for characterizing the superparamagnetic response of ferritin using MSM-AFM. By applying an external magnetic field to the sample stage the magnetic domains of ferritin were driven to vibrate on the surface. Magnetically selective contrast was demonstrated for MSM phase and amplitude channels for vibrating domains of ferritin micropatterns. The new hybrid mode of MSM-AFM is an advancement of the method of force modulation AFM. With force modulation, the entire sample is driven to vibrate for detecting elastic properties. Whereas for MSM-AFM, only magnetic or superparamagnetic domains are driven to vibrate for magnetically selective

imaging with unprecedented sensitivity. Parameters of the magnetic field strength as well as the driving frequency were systematically ramped to obtain dynamic MSM-AFM measurements. The difference in contrast (phase and amplitude) for areas imaged with and without magnetic field were demonstrated to selectively map the location of superparamagnetic nanoparticles.

CHAPTER 5. INVESTIGATION OF THE MAGNETIC PROPERTIES OF FERRITIN BY AFM IMAGING WITH MAGNETIC SAMPLE MODULATION*

5.1 Introduction

Size scaling relationships can be used to tailor the magnetic properties of materials from the bulk ferromagnetic level to the superparamagnetic regime. Magnetic nanoparticles of iron oxide tend to be either paramagnetic or superparamagnetic depending on sample dimensions. Superparamagnetism is one example of the interesting size-dependent phenomena of magnetic nanomaterials. Nanoparticles with superparamagnetic behavior are similar to paramagnetic substances which lose their magnetization when the magnetic field is removed, however superparamagnetic particles exhibit a much higher magnetic moment.[197, 198] Superparamagnetic particles of Fe_2O_3 and Fe_3O_4 do not retain any magnetism after removal of the magnetic field, which is a critical requirement for MRI contrast agents.[199] Ferromagnetic materials exhibit an intense magnetic field when an external magnetic field is applied, but in a bulk sample the material will usually be nonmagnetized because of the random orientation of spin domains. A small externally imposed magnetic field can cause the magnetic domains to line up with each other to magnetize nanomaterials.

Ferritin is a spherical iron storage protein with a hollow shell enclosing a cavity containing iron atoms. The ferrimagnetic core of ferritin is weakly paramagnetic.[200] Ferritin is the primary regulator for iron metabolism for both prokaryotes and eukaryotes. The outer diameter of the ferritin shell is 12 nm. Ferritin is the primary regulator for iron metabolism, and problems with iron uptake have been diagnosed for patients with anemia,[201] diabetes,[202, 203] rheumatoid arthritis,[204] liver[202] and kidney disease.[205-207] The uptake and release mechanisms of ferritin are caused by the oxidation and reduction of iron ions (Fe(II)/Fe(III)).

*Reprinted with permission from Springer

Designed nanoscale platforms of magnetic nanomaterials and metalloproteins can be generated using particle lithography with colloidal silica or latex mesospheres.[38, 208, 209] Using particle lithography, high-density nanostructures with exquisitely uniform geometries can be prepared on surfaces with few defects, without costly instruments or vacuum environments. Particle lithography has previously been applied to pattern metals,[210] inorganic materials,[211] alkanethiol self-assembled monolayers,[212, 213] polymers[214-216] and proteins[39, 217, 218] with a variety of surfaces. Protein patterning is a critical technology for the integration of biological molecules into miniature biological-electronic devices. Direct applications of protein patterning include biosensing, medical implants, control of cell adhesion and growth, and for fundamental studies of cell biology.[219-222]

In this report, proof-of-concept results are demonstrated for a new magnetic imaging mode of AFM. We refer to the imaging mode as "magnetic sample modulation" or MSM-AFM, since the flux of an electromagnetic field is used to induce physical movement of magnetic nanomaterials. Unlike previous AFM imaging modes which use specifically designed tips to interrogate samples, for MSM imaging the changes in sample dynamics form the basis for measurements of material properties. The sample is driven to vibrate in response to an externally applied electromagnetic field and the tip is used as a force and motion sensor for mapping the vibrational response. Investigations are presented for test platforms of ferritin nanostructures prepared using particle lithography.

5.2 Experimental Approach

5.2.1 Materials and Reagents

Silica mesospheres (Duke Scientific, Palo Alto, CA) measuring 500 nm in diameter were used for particle lithography. Freshly cleaved pieces of mica(0001) were used as substrates (Ruby muscovite mica, S&J Trading Inc., Glen Oaks, NY). The mica was cut into circular pieces

(1×1 cm^2) and cleaved immediately before depositing sample solutions. Horse spleen ferritin was purchased from MP Biomedical, Inc. (Solon, OH). Stock solutions of ferritin were prepared in deionized water (18 MΩ resistivity). The concentration of ferritin used for patterning was 5 mg/mL.

5.2.2 Atomic Force Microscopy (AFM)

Measurements were obtained with an Agilent 5500 AFM system using Picoscan v5.3.3 software. Software from Gwyddion was used to process images, which is freely available on the Internet (http://gwyddion.net/). Rectangular type silicon nitride cantilevers (NSC14/Al, MikroMasch, Portland, OR) with resonance frequency of 186 kHz, and spring constant 5 N/m from were used to acquire tapping mode images (Figures 5.3 and 5.4). Standard soft cantilevers, (MSCT-AUHW, Veeco Probe Store, Camarillo, CA) with spring constants ranging from 0.05 - 0.1 N/m were used for imaging with contact mode (Figure 5.5). Images were acquired at ambient temperature in air. The relative percentage of colored pixels was used to obtain estimates of surface coverage, using UTHSCA Image Tool software.[223]

5.2.3 Preparation of Ring Structures of Ferritin Using Particle Lithography

Particle lithography provides a practical means to create arrays of nanostructures on surfaces using straightforward steps of bench chemistry (e.g. mixing, centrifuging, drying and rinsing). The steps for particle lithography with proteins are outlined in Figure 5.1. Monodisperse mesospheres of 500 nm colloidal silica were mixed with the desired protein in aqueous solution and deposited directly onto substrates. As the solution dries, the mesospheres assemble naturally into a close-packed crystalline layer with proteins surrounding the base of the spheres (Figure 5.1A). The close-packed spheres provide a structural template to direct the surface arrangement of the proteins. By rinsing with water, the spheres can be selectively and completely displaced from the surface. The proteins remain attached to the substrate despite copious rinsing steps to

form well-defined nanopatterns (Figure 5.1B). Protein nanostructures form in accordance to the arrangement and periodicity of the structural templates of mesospheres. The overall surface coverage and density of protein nanostructures can be tailored by selecting the ratio of protein-to-latex as well as the diameter of the mesospheres.

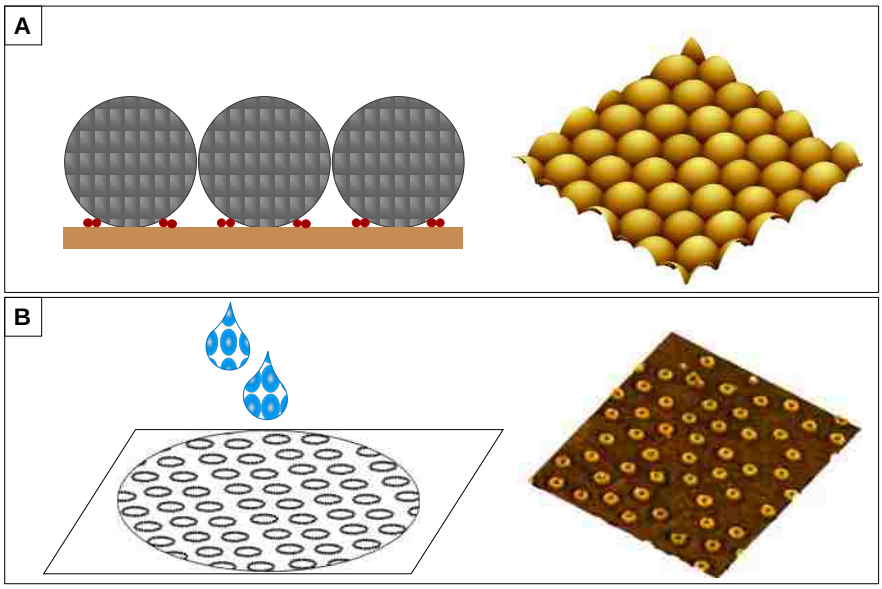

Figure 5.1 Basic steps for particle lithography with proteins. [A] a mixture of protein and monodisperse mesospheres is dried on a flat surface. [B] the spheres of the structural template are readily rinsed away with water, to generate well-defined protein nanostructures.

5.2.4 Using Contact-Mode AFM with Magnetic Sample Modulation

Oscillating magnetic fields can be applied to samples using well-developed technology from Agilent with a "MAC-mode" sample plate accessory. An AC current is applied to a wire coil solenoid located within the sample stage, which produces an oscillating electromagnetic field (Figure 5.2). For MSM-AFM imaging, the sample is placed on the sample stage near one end of the solenoid, where it will experience the strongest magnetic flux. When no current is applied and the magnetic field is off, the sample can be scanned using conventional contact mode AFM to acquire topography and frictional force images. The typical imaging procedure first requires acquisition of conventional contact mode topographic and frictional force images. Next,

the same area of the surface is scanned again, however with an oscillating magnetic field applied to the sample plate. The mechanical motion of the sample will produce changes in the phase and amplitude frames for the areas which are physically vibrating in response to the flux of the applied magnetic field. The differences displayed in images with and without an applied magnetic field are used to map the location of magnetic nanomaterials such as ferritin.

The MSM-AFM imaging mode employs a standard soft commercial cantilever rather than using a magnetic tip with a bulky metal coating as the sensor. For MSM imaging, uncoated cantilevers are used in combination with contact mode AFM imaging under the influence of an external AC electromagnetic field. The nosecone of the scanner is constructed with plastic components to ensure that the magnetic field does not induce vibration of the tip holder assembly. The oscillating electromagnetic field (in the range of 0.2-2 T) is sufficient to induce magnetic actuation of the sample.

For the instrument set-up of MSM-AFM, positional feedback for the scanner is not changed and the typical force-deflection settings for scanning in contact mode are used for topographic data acquisition. To obtain signals for the amplitude and phase components of the tip motion, an auxiliary output channel from the quadrant photodiode of the AFM scanner is directed to input channels of a lock-in amplifier, using the driving AC waveform as a reference. Thus, the periodic motion of the sample vibration can be tracked by changes in the deflection of the tip. The changes in phase angle and amplitude as the tip interacts with vibrating areas of the sample are plotted as a function of tip position to create MSM phase and amplitude images. The lock-in amplifier used to acquire the amplitude and phase components of the AC signal provides extreme sensitivity for small changes in AFM tip movement. Essentially, MSM is a hybrid of contact mode AFM combined with selective vibration of magnetic domains. Reconstruction of both the amplitude and phase signal simultaneously with the topographic image, and spectra of

the vibration response can be acquired with nanoscale resolution. The MSM amplitude images map changes in the magnitude of the AFM tip motion as it encounters a vibrating sample, with reference to the driving AC current. The changes in phase result from differences in the waveform of the driving current applied to the solenoid versus the changes in the periodic motion of the scanning AFM tip. Both channels (phase and amplitude) sensitively detect sub-angstrom changes in AFM tip motion caused by vibration of the magnetic samples.

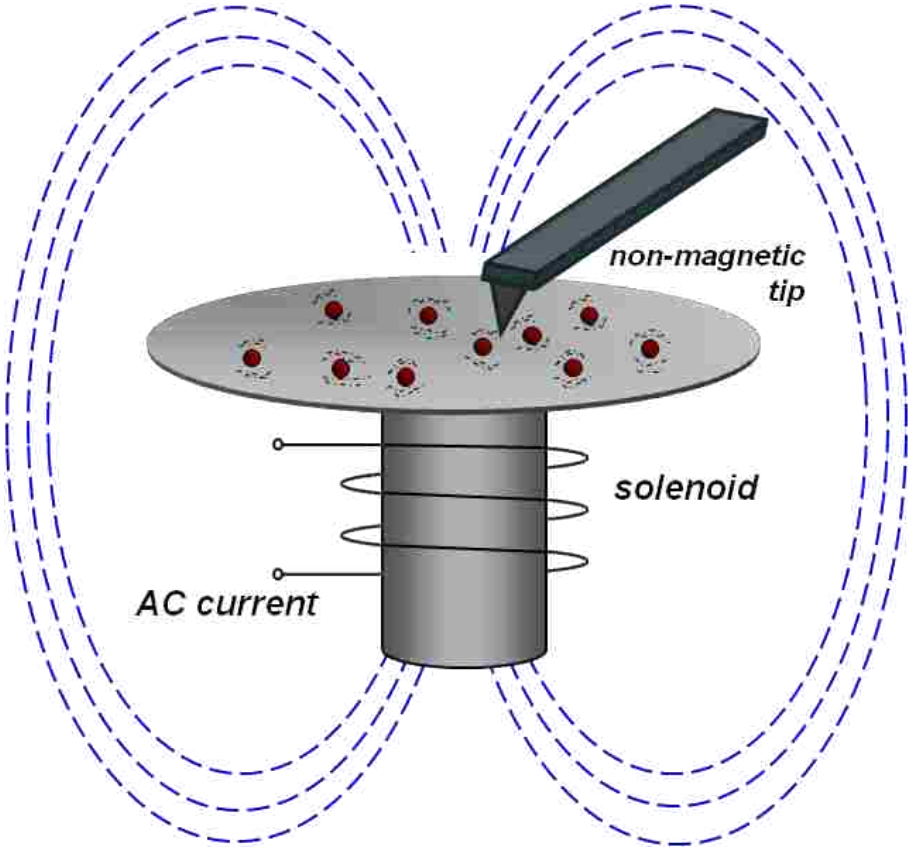

Figure 5.2 Concept for magnetic sample modulation (MSM-AFM). An AC electromagnetic field is applied to the sample to induce a periodic motion of magnetic nanomaterials, such as ferritin. Vibrating areas of the sample are detected by an AFM tip operated using contact mode.

5.3 Results

A key strategy for the experiments was to apply particle lithography to produce arrays of nanostructures as test platforms with tunable sizes and spacing. Millions of nanostructures can be

prepared on surfaces with relatively few defects and high reproducibility to enable multiple successive SPM measurements with well-defined surface structures. Custom test platforms of magnetic nanomaterials were prepared using particle lithography to facilitate AFM characterization at the level of individual proteins. The ferritin test structures were used to evaluate the capabilities of MSM for acquiring dynamic information about changes in the vibrational response of individual ferroproteins.

5.3.1 Surface Aggregation of Ferritin

Typically, when dilute solutions of proteins are deposited and dried on surfaces under natural conditions, aggregates form without defined arrangements. The self-aggregation of proteins often generates multilayer films and irregular dense clusters throughout the surface. When samples are dried, forces such as electrostatic and hydrophobic forces tend to pull proteins together into a clustered morphology. An example AFM image of protein aggregates is presented in Figure 5.3A, for a dilute solution of ferritin that was dried on the surface of mica(0001). Ferritin has a nearly spherical shape; however within this image the natural geometry is indistinguishable within the tightly packed clusters and chains resulting from surface aggregation. Particularly for AFM characterizations, the width of the probe is too large to penetrate between the tightly packed proteins to enable resolving the true shape of individual proteins. At intermediate surface coverage (49%) the height of the aggregates measures 10 ± 2 nm (Figure 5.3B), in good agreement with the known dimensions of ferritin. According to measurements using X-ray crystallography, the outer diameter of ferritin measures 12.5 nm.[224]

5.3.2 Nanostructures of Ferritin Produced with Particle Lithography

Particle lithography (PL) can be used to control the arrangement and surface coverage of proteins, preventing problems with surface aggregation.

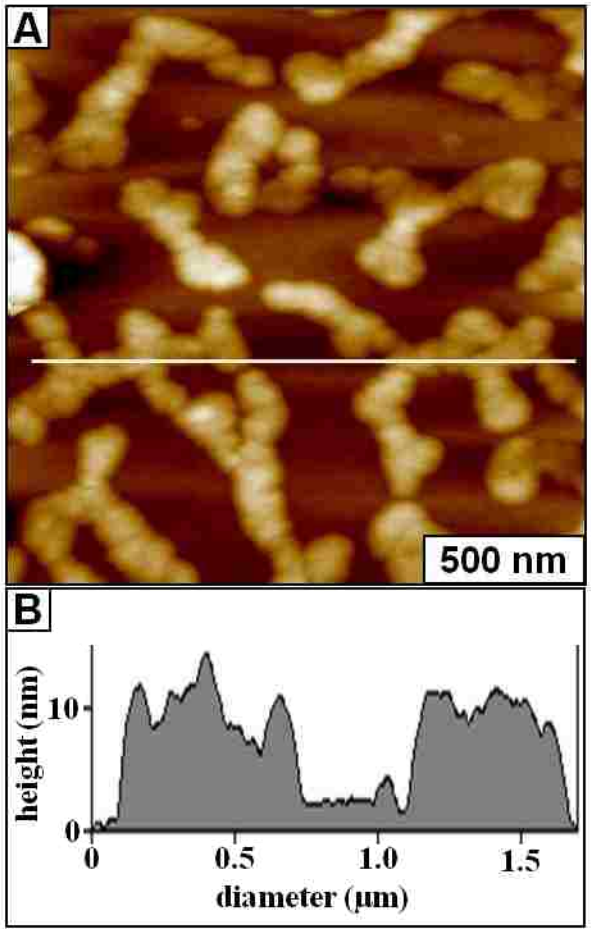

Figure 5.3 Natural surface assembly of ferritin. [A] topograph acquired with tapping-mode AFM; [B] cursor profile for the line drawn in **A**.

An example is presented in Figure 5.4 displaying successive zoom-in views of ring structures of ferritin, acquired using tapping mode AFM. Regularly spaced circular arrangements of proteins were produced using monodisperse silica mesospheres as structural templates. The periodic arrangement of the silica spheres define the spacing between the rings; the average periodicity measured 500 ± 36 nm, matching the 500 nm diameter of the silica mesospheres. There are approximately 65 rings within the 5 x 5 μm^2 area of Figure 5.4A, which would scale to ~10^8 nanostructures per square centimeter. Individual proteins are observed that are randomly scattered between the ring structures. If the ratio of proteins-to-mesospheres is increased, the areas between rings can be completely filled-in to generate pore structures.[209]

A closer view of simultaneously acquired topography and phase images (Figures 5.4B and 5.4C, respectively) clearly resolves the shape and arrangement of ferritin patterns. Phase images are often more sensitive to the shape of nanoscale features, without the distortions of height scaling that are often apparent in topographs. Figure 5.4C is an exquisite example of the capabilities of phase imaging for discriminating the detailed surface morphology at the edges of the proteins. The color contrast of phase images originates from differences in tip-sample adhesion as well as the viscoelastic response of the tapping AFM tip. The pores within the rings define the places where the silica mesospheres were attached to the surface, the areas became uncovered during the rinsing step. The color of the areas within the pores matches the bare regions of the surface surrounding the ferritin rings, which is evidence that the mesospheres were completely removed and did not leave residues on the surface.

At high magnification (Figure 5.4D) the round shape of ferritin within the ring structures is well resolved in the tapping mode topography image. The hexagonal arrangement of ferritin patterns is apparent, and the surface coverage measured 18% for the 2 x 2 μm^2 area. A cursor profile across two ring structures (Figure 5.4E) displays a height of 11 ± 2 nm, and the average diameter of the rings measured 312 ± 23 nm. The diameters of the ferritin rings are regular and uniform for all of the ring structures viewed in the series of images in Figure 5.4, with thicknesses corresponding to a single layer of ferritin. A 3D view of a single pattern is presented in Figure 5.4F, displaying the spherical shape of ferritin which form the rings.

5.3.3 Imaging Ferritin Using Magnetic Sample Modulation AFM

Arrays of nanostructures of ferritin make ideal test platforms for investigating the limits of resolution for MSM-AFM imaging. The regularly shaped nanostructures enable multiple successive AFM measurements for reproducible surface structures. The iron cores of ferritin are ferromagnetic, and thus provide a natural, well-defined reference sample for magnetic imaging.

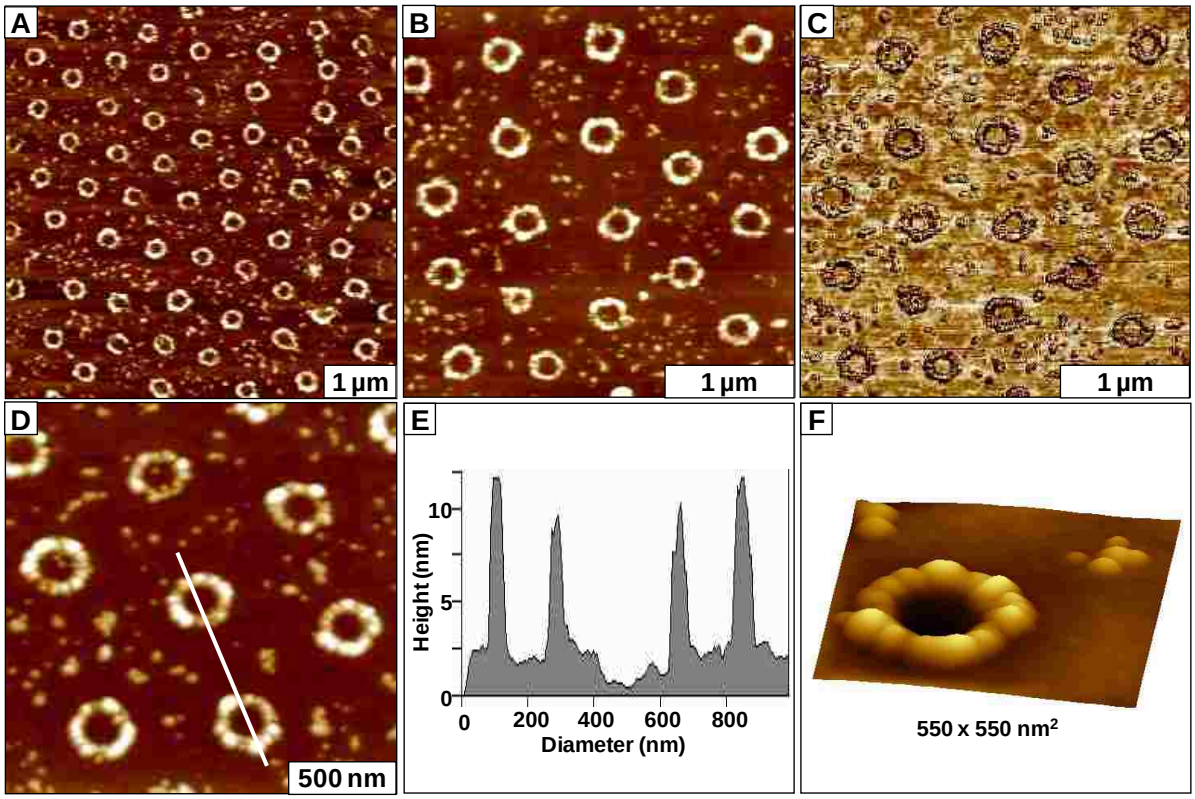

Figure 5.4 Ring nanopatterns of ferritin produced on mica(0001) using particle lithography. [A] wide area topograph imaged with tapping mode; [B] zoom-in (3 x 3 μm^2); [C] matching phase image for **B**; [D] topograph showing the hexagonal arrangement of ferritin rings; [E] cursor for the line in **D**; [F] individual ring structure of ferritin.

The AFM tip scanning in contact mode serves as a force and motion sensor to detect the vibration of the sample. A requirement for MSM-AFM imaging is that the sample be movable, without detaching from the surface. The core of ferritin is encapsulated by a protein cage, which remains securely attached to the surface. In planning experiments, we hypothesized that an externally applied AC electromagnetic field would induce ferritin to rock back and forth in response to the flux of the field, and this nanoscale vibrational motion would be detectable by MSM-AFM imaging.

To provide a baseline reference image, a 9 x 9 μm^2 area of the surface was first scanned using contact mode AFM without the influence of a magnetic field (Figures 5.5A-5.5C). The undistorted morphology of a periodic array of ferritin rings is viewed in Figure 5.5A for a

conventional AFM topograph. Without applying an electromagnetic field, the tip and sample do not vibrate, as evidenced by the absence of contrast or shapes in the simultaneously acquired phase (Figure 5.5B) and amplitude (Figure 5.5C) frames. Next, the same sample was scanned with an applied AC field (0.2 T, 96 kHz) to acquire MSM images (Figures 5.5D-5.5L), using the same AFM tip. The left column of Figure 5 presents MSM topographs for successively smaller areas, from top to bottom. The corresponding MSM phase images are displayed in the center column, and the right column shows the MSM amplitude frames. With MSM images, Figures 5.5D-5.5F display an area that is the same size as Figure 5.5A. Comparing the topography channels of Figure 5.5A versus Figure 5.5D, the lateral dimensions of the rings appear to be wider. Thus, depending on the strength of the magnetic flux, the vibration of magnetic nanoparticles is actually detectable in the topography images, such as for Figure 5.5D.

The MSM amplitude and phase images clearly distinguish the locations of ferritin, with well-defined contrast for the rings and also for the individual proteins located between rings. The MSM phase images are produced by spatially mapping the changes in the response of the AFM tip compared to the sinus waveform of the AC current applied to drive the sample modulation. The amplitude images display changes in the magnitude of the tip oscillation. The ferritin particles vibrate in response to the rhythm of the AC electromagnetic field, with a periodic motion and frequency according to the designed experimental settings. As the AFM tip is brought into contact with vibrating areas of the surface, the force and motion of the surface changes are sensitively detected in phase and amplitude channels. An advantage of MSM-AFM is that amplitude and phase images can be acquired simultaneously with topography images, to aid in identifying magnetic and non-magnetic areas of the sample. The dynamic conditions of the applied field strength, the force applied to the AFM probe and the frequency parameters can be systematically varied to visualize nanoscale changes in the magnetic response of magnetic

nanomaterials. By comparing the resulting output wave function of the tip motion to the input signal of the AC voltage, information for amplitude and phase lag detected for vibrating materials can be obtained. The changes in phase angle and amplitude as the tip interacts with the vibrating sample are plotted as a function of tip position to create MSM phase and amplitude images.

The ring patterns and individual ferritin proteins are well resolved in the topography, amplitude and phase channels for the MSM zoom-in views (Figures 5.5G-5.5L). The vibration of the samples causes a distortion and elongation of the dimensions of ferritin, thus the field must be turned off for accurate topography measurements. The shapes of individual particles of the rings cannot be distinguished for the high magnification images at 96 kHz. Future experiments will address changing the parameters of the AC field strength and driving frequencies for improving image resolution for small areas.

The mapping capabilities of the MSM-AFM imaging mode presented in the previous section can be combined with acquisition of frequency spectra at selected areas. A control spectral profile was acquired to determine if the uncoated AFM cantilever responds to the flux of the electromagnetic field. The tip was lifted a short distance from the surface, and the frequency of the magnetic field was swept from zero to 90 kHz (Figure 5.6). When the tip was disengaged, the vibrational response mostly shows a flat baseline, with no significant resonance peaks. Next the tip was brought into contact with the surface and placed directly on the ferritin sample. A number of prominent peaks were detected throughout the range of frequencies tested. The broadening of the peaks is attributed to the sample motion, and any of the peak frequencies could be used successfully to acquire MSM images. Future experiments are planned to evaluate the frequency and amplitude dependence for MSM-AFM imaging for a broader range of frequency and field strength parameters.

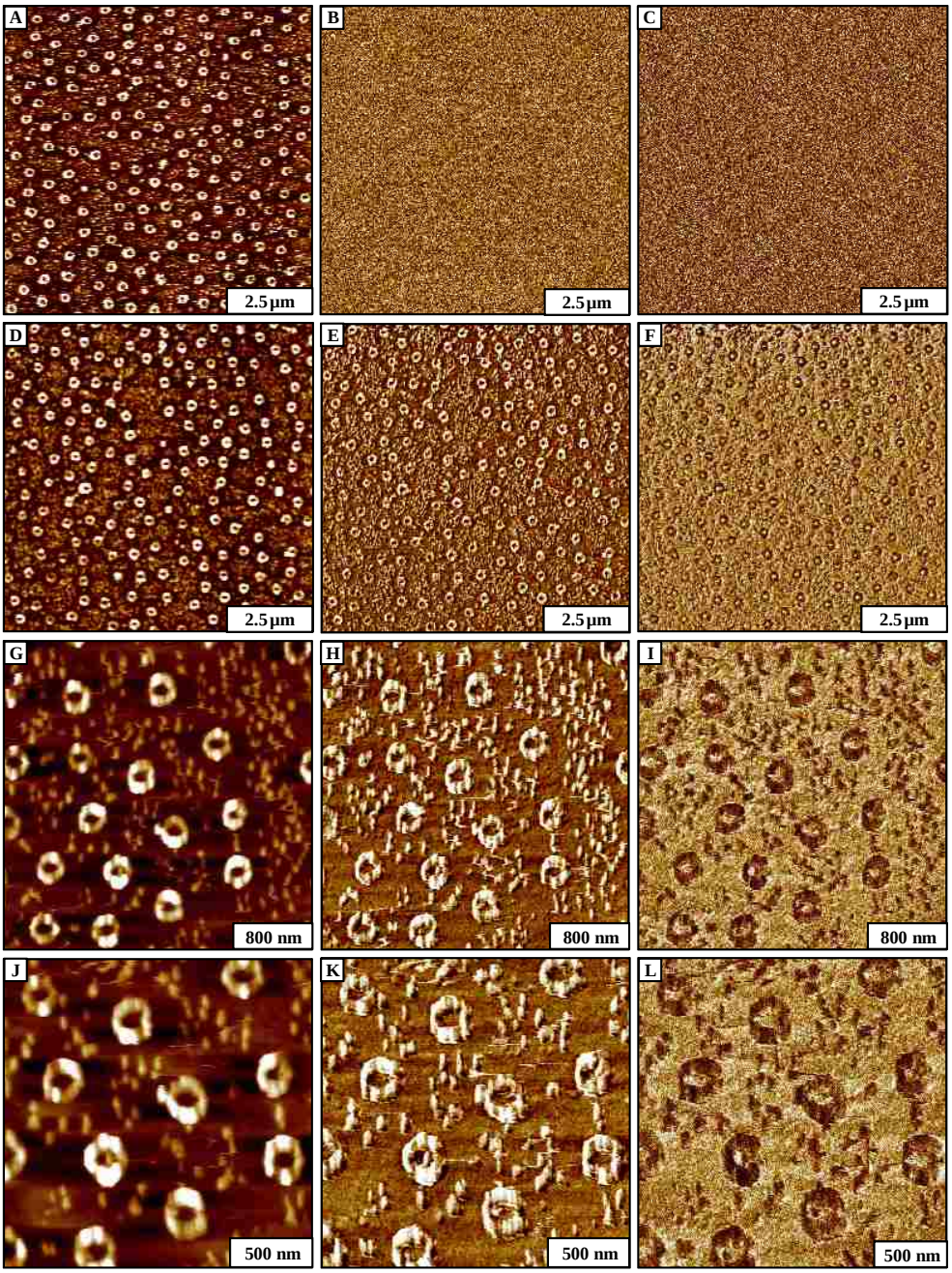

Figure 5.5 AFM images of ferritin ring structures acquired with MSM. [A] conventional topography image acquired with contact mode (9 x 9 μm^2); [B] corresponding amplitude channel without magnetic flux; [C] phase channel without an applied field. [D] topograph acquired using MSM (9 x 9 μm^2); [E] MSM amplitude frame for **D**; [F] MSM phase image for **D**. [G] zoom-in MSM topograph; [H] MSM amplitude channel for **G**; [I] MSM phase image for **G**. [J] MSM topograph with further magnification; [K] MSM amplitude image for **J**; [L] MSM phase image for **J**.

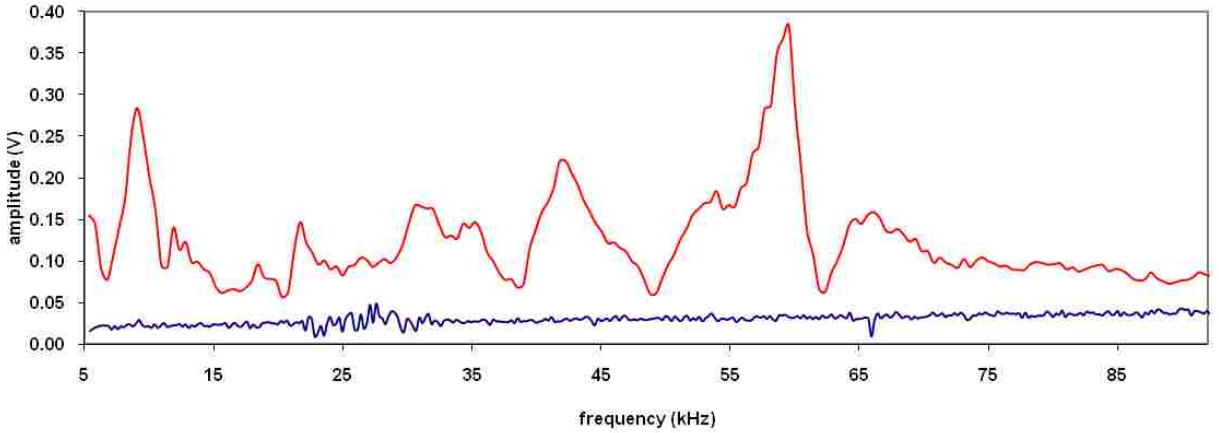

Figure 5.6 Frequency spectra with MSM-AFM. Profile of the vibrational amplitude of the AFM tip during a frequency sweep when the tip was disengaged from the surface (blue line); and when it was in contact with the ferritin sample (red line). The red line is shifted by 0.05 V for clarity.

The frequency spectra were found to depend on the point of contact between the tip and sample. When the tip was placed on bare areas of the surface, no spectra could be obtained.

5.4 Discussion

For magnetic sample modulation or MSM-AFM, the samples are induced to vibrate in concert with the flux of an externally applied electromagnetic field. A soft, *non-magnetic* AFM tip is operated in contact mode to detect the force and motion of nanomaterials which vibrate in response to the externally applied oscillating magnetic field. Lock-in detection is used for sensitively tracking changes in the amplitude, phase and frequencies of motion compared to the driving AC electromagnetic field. The MSM-AFM technique provides exceptional sensitivity and is selective for distinguishing samples which have a magnetic moment in the presence of an applied AC electromagnetic field.

The strategy of the conventional SPM imaging mode for magnetic detection known as magnetic force microscopy (MFM)[58, 225-229] is quite different from our newly invented MSM mode. For MFM, an AFM tip that is coated with a magnetic material is required as a sensor to detect the relatively weak long-range forces of magnetic areas of surfaces operating over

distances of 50-200 nm from the surface. For MFM, the strength of the magnetic field must be strong enough to deflect or attract a micrometer-sized cantilever to enable mapping of the magnetic domains. The MFM approach provides a means to map the strength of the magnetic field at various distances, (e.g. 50, 100, 150 nm) from the surface. When the tip is attracted towards the surface, dark contrast is generated in images; as the tip is repelled by the surface, brighter contrast results. Thus, MFM indicates the relative strength and polarity of magnetic regions. The limits of MFM detection intrinsically depend on the size and spring constant of the magnetic lever. The topography resolution is generally poor with MFM, since the magnetic coatings on the underside of MFM tips results in probes that are blunt and bulky. The detection capabilities of the new MSM-AFM imaging mode, demonstrated by the results presented pushes beyond the typical 200 nm detection limit of MFM to characterize magnetic nanomaterials as small as 12 nm. Several other magnetic SPM imaging modes have been developed such as magnetic resonance force microscopy (MRFM),[62, 230-232] magnetic AC or MAC-mode,[233-236] and magnetic force modulation;[237] however all of these methods require the use of tips with a magnetic coating for detecting magnetic forces. A clearly different imaging strategy is applied for MSM-AFM, which *requires* nonmagnetic tips. For MSM-AFM, the tip is used to detect motion and vibrational response rather than directly measuring magnetic fields.

5.5 Conclusion

Results with MSM demonstrate new possibilities for AFM imaging of magnetic nanomaterials such as ferritin, with unprecedented sensitivity. Combining contact mode AFM imaging with MSM-AFM provides new capabilities for distinguishing and mapping magnetic nanomaterials at the level of tens of nanometers. The iron present in ferritin can be sensitively mapped using magnetic sample modulation (MSM-AFM). An actuated magnetic field causes the ferromagnetic protein to vibrate, and the motion at sample resonances is detected and mapped

using a soft non-magnetic AFM cantilever. In essence, MSM-AFM enables one to visualize how magnetic nanoparticles or metalloproteins respond to the flux of an applied AC electromagnetic field. The mechanical motion of the sample can be sensitively detected by a scanning AFM tip. The MSM-AFM imaging mode may become an important technique among the growing arsenal of SPM characterizations applied for characterizing the properties of nanomaterials. The MSM-AFM investigations are facilitated by preparation of designed test platforms of magnetic materials at nanometer length scales using particle lithography. The exquisite capabilities for generating nanostructures of varied dimension and composition are illustrated by high throughput patterning of ferritin ring structures.

CHAPTER 6. NANOSCALE SURFACE CHARACTERIZATION OF THE EARLY STAGES OF AQUEOUS COPPER CORROSION: EFFECTS OF IMMERSION INTERVAL AND ORTHOPHOSPHATE CONCENTRATION

6.1 Introduction

Fundamental investigations of the corrosion and passivation process of copper surfaces are important for improving the quality of consumer tap water and for preserving of distribution pipelines. Copper is used in household plumbing because of the inherent durability, inertness, and manufacturability.[238] When copper pipes are exposed to aggressive water, the metal can corrode, producing by-products that leach into drinking water and eventually lead to structural failure. Although copper is an essential nutrient, exposure to elevated levels of copper from drinking water has been linked to health problems.[239, 240] As a result, the United States Environmental Protection Agency (USEPA) established an action level of 1.3 mg/L for copper for drinking water.[241] The effects of water composition for accelerating or mitigating the corrosion of copper pipes, is not fully understood. For this chapter, surface changes were investigated for designed water conditions of pH and orthophosphate levels. Surface changes at the nanoscale within 6 to 24 hours of exposure to water solutions were characterized with AFM. Surface spectroscopies were applied to identify the composition of the surface deposits.

Copper corrosion is an electrochemical process involving the transfer of electrons between the metal (anode) and oxidant (cathode), and requires an electrolyte interface.[240, 242] Structural defects on the metal surface can serve as nucleation sites for initiating corrosion.[243] Copper can resist corrosion by forming a protective layer of cuprous oxide (Cu_2O)[244, 245] that acts as a barrier to slow the corrosion process.[246] During the formation of the passivation layer, properties such as porosity, thickness and conductivity affect the progression of corrosion.[247-249] Studies have shown that the disruption of cuprous oxide can be attributed to changes in water

chemistry such as pH, alkalinity and the presence of certain anions, including sulfate and chloride.[49, 250]

To overcome the problem of copper leaching into drinking water, chemical inhibitors are added to drinking water. Distribution facilities will treat drinking water with phosphorus compounds such as orthophosphate, polyphosphate or silicate to reduce corrosion.[251, 252] Orthophosphate is the most commonly used inhibitor for corrosion of metals. This inorganic compound forms a cuprite-phosphate ($Cu_3(PO_4)_2$) complex which reduces dissolved oxygen at the metal surface, thereby decreasing copper solubility, pitting initiation, and oxidant demand. Therefore, lessening further oxidation that may lead to the formation of other corrosion by-products. The capability of orthophosphate to aid in the passivation of the copper surface is greatly dependent on pH, disolved inorganic carbon (DIC), and dosage concentration of the inhibitor. Much efforts have focused on the effectiveness of phosphates inhibitors in drinking water.[253-255]

Several macroscopic techniques have been applied to study copper corrosion such as electrochemical impedance spectroscopy (EIS)[44] and cyclic voltametry[256] to evaluate the development of the protective layer formed on the metal surface. Recently, atomic force microscopy (AFM) has emerged as an important technique for directly characterizing surface changes of corroding metals for both *in situ* and *ex situ* experiments, with nanoscale resolution.[250, 257] Morphology changes of stainless steel[258] copper thin films[259] and brass[260] due to corrosion have been studied using AFM, however information for speciation of the surface deposits has not been obtained.

Our previous reports furnished nanoscale studies of surface changes for designed parameters to evaluate the role of polyphosphates, DIC and pH.[250, 261] For the new investigations in this chapter, our goals were to compare changes at systematically smaller increments of pH

and to acquire complementary surface spectroscopy information to identify and provide chemical details for the solids formed on treated copper surfaces. Measurements with x-ray diffraction (XRD) and near edge x-ray absorption fine structure (NEXAFS) spectroscopies provide information of the oxidation state for metal complexes that formed, and fourier transform infrared spectroscopy (FTIR) enables structural identification for surface films.

6.2 Methods and Materials

6.2.1 Chemicals and Reagents

Water (double-deionized, 18.2 MΩ•cm resistivity) was prepared in a l L reaction cell to a composition of 10 mg C/L DIC, 60 mg/L chloride, 120 mg/L sulfate, and 3 mg/L free chlorine. Levels of DIC were maintained with sodium bicarbonate. Purified grade (4-6%) sodium hypochlorite was added to maintain residual free chlorine. Free chlorine residual was measured at a wavelength of 530 nm using a HACH colorimeter by the colorimetric version of the N,N-diethyl-p-phenylenediamine (DPD) method.[262] Experiments were completed with and without the addition of orthophosphate to the water. When present, the orthophosphate level was maintained at 6 mg/L. The pH of the water was adjusted by adding hydrochloric acid and sodium hydroxide to the solution with an automated titrator as needed for pH values of 6.5, 7, 8 and 9. Sheets of commercially available copper alloy (110 ASTM B187) (Metal Supermarket, Cincinnati, OH), were cut into 0.75 × 0.75 in^2 squares. Before exposure to the synthetic drinking water, unpolished copper coupons were cleaned in 0.05% Triton-X 100, sonicated for 5 minutes, rinsed and sonicated in water, and finally rinsed with pure acetone to remove any organic materials from the surface. The copper coupons were suspended in the synthetic drinking water and agitated slowly in a beaker at room temperature (25ºC). Two coupons were placed in the reaction cell, and were removed after 6 h and 24 h, respectively. Coupons were dried before analysis with tapping-mode AFM.

6.2.2 Atomic Force Microscopy

Images of the copper coupons were captured using an Agilent 5500 AFM/SPM system with Pico Scan v5.3.3 software (Agilent Technologies, Chandler, AZ). The surface was probed with commercially available Si_3N_4 AFM tips (PPP-NCL resonance frequency of 167 kHz) purchased from NanoSensors (Tempe, AZ). Scans of the samples were acquired with tapping-mode in ambient air. The scan rate for AFM imaging ranged from 1.0-1.2 μm/s. The raw data collected was processed with Picoscan software and the surface roughness was calculated using Gwyddion software version 2.10.[263]

6.2.3 Infrared (IR) Micro-Spectroscopy Measurements

Infrared (IR) micro-spectroscopy measurements for the copper samples were obtained using angle-resolved photoemission spectroscopy and high resolution photoemission, by means of the IR reflection mode with a Thermo Nicolet continuum microscope. The IR spectra were collected with the Thermo Nexus 670 FTIR spectrometer, equipped with a deuterated triglycine sulfate (DTGS) detector.

6.2.4 X-ray Diffraction Analysis

X-ray diffraction data was acquired with a Scintag (Scintag, Inc., Santa Clara, CA) model XDS-2000 theta-theta diffractometer. A copper KR source was used to identify the copper precipitates. The tube was operated at 40 kV and 40 mA for the analyses. Scans were performed over a 2-theta range between 5° to 90° with a step size of 0.02° and a one-second count time at each step. Pattern analysis generally followed ASTM procedures and was performed using the computer software Jade (version 8, Materials Data, Inc.), with reference to the 1995-2002 ICDD PDF-2 data files (International Center for Diffraction Data, Newtown Square, PA).

6.2.5 Near Edge X-ray Absorption Fine Structure (NEXAFS)

Measurements with NEXAFS were performed using a variable-line-space plane-grating-monochromator (VLSPGM) beamline.[264] The tunable incident radiation, with a resolution of better than 0.2 eV at the copper L-edge, is focused onto the samples located in a UHV chamber. The photon energy scale was calibrated with copper standard samples (Cu_2O and Cu). The incident beam intensity was concurrently monitored by a gold mesh placed in the incident beam before the sample. The measured sample spectrum I_0 (total electron yield mode) was normalized by the total electron yield of the gold mesh. Reproducibility of the spectra was carefully monitored and verified by multiple scanning, typically four times. NEXAFS spectra were acquired at room temperature at both the oxygen K-edge and the copper L-edge regions.

6.2.6 Data Analysis

Surface roughness (Rq) calculations were used to quantitatively compare results for selected areas for high resolution AFM images. Difference in local roughness of the surface can vary greatly at the nanometer level, according to magnification scales and tip geometries. The Rq was calculated with Gwyddion software using Equation 1.

$$Rq = \sqrt{\frac{\sum_{i=1}^{n} (Z_i - \bar{Z})^2}{n}} \qquad \textit{Eq. 1}$$

Where Z_i is the vertical height of each data point, Z_{avg} represents the average of the Z_i values, and n represents the number of data point within the given area.[265] Small changes (less than 20 nm) in surface roughness for AFM images are subjective and may not be considered as absolute values for comparison of surface changes.

Estimates for surface coverage were determined for selected surface areas to evaluate changes in the amount of deposits formed on the substrate. Analysis of surface coverage was

obtained with UTHSCA ImageTool.[266] The percentage of colored pixels was determined subjectively for surface coverage estimates. Topography images were converted to grayscale bitmaps and a threshold value was selected visually for conversion to black and white pixels.

6.3 Results and Discussion

6.3.1 AFM Characterization of Copper Samples

A clean, untreated copper coupon was imaged with the AFM to establish a baseline reference for topography changes. To more closely represent the surface conditions of household plumbing, clean copper coupons were not polished or etched. Representative images of a clean copper coupon are shown in Figure 6.1. Grooves and scratches are apparent on the copper surface with a few absorbates (Figure 6.1A). The surface roughness measured 0.11 µm, indicating that the surface is relatively smooth for the 5×5 μm^2 view in Figure 6.1B. Concurrently acquired phase images often reveal surface details that are not readily veiwable in topography frames. Phase images indicate differences in surface chemistries or variations in composition.[267]

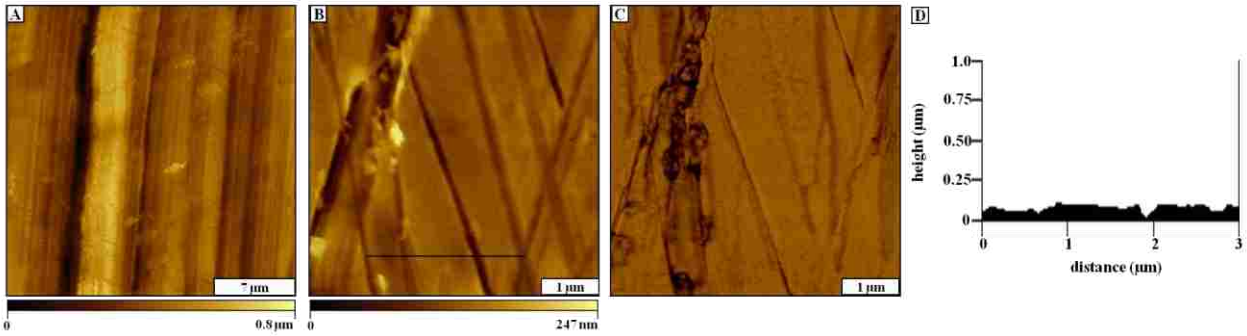

Figure 6.1 Surface views of a clean, untreated copper substrate. [A] representative topograph of a clean surface (25×25 μm^2) acquired using tapping mode AFM in air. [B] zoom-in view (5×5 μm^2); [C] corresponding phase image; [D] cursor profile for the line drawn in **B**.

The contrast in the phase image (Figure 6.1C) is relatively homogenous for the flat areas of the simple. The darker color at corners and channels, as a result of edge effects. A cursor profile

across the substrate in Figure 6.1B indicates variations in height of the surface scratches are less than 0.1 µm, in close agreement with the roughness estimate.

The surface morphology of copper samples that were exposed to water without orthophosphate were compared at pH 7 for immersion intervals of 6 h and 24 h (Figure 6.2). At neutral (pH 7), AFM images reveal small solids scattered on the surface after 6 h of immersion, as shown in Figure 6.2A. A magnified view of the same area, reveals the precipitates have an irregular shape (Figure 6.2B). The surface roughness measured 0.066 µm with an estimated surface coverage of 17% for the 15×15 μm^2 image (Figure 6.2B). The corresponding phase image is displayed in Figure 6.2C, providing sharper outlines of the surface contours. The solids measure approximately 0.10-0.25 µm in height, as shown by the cursor profile in Figure 6.2D.

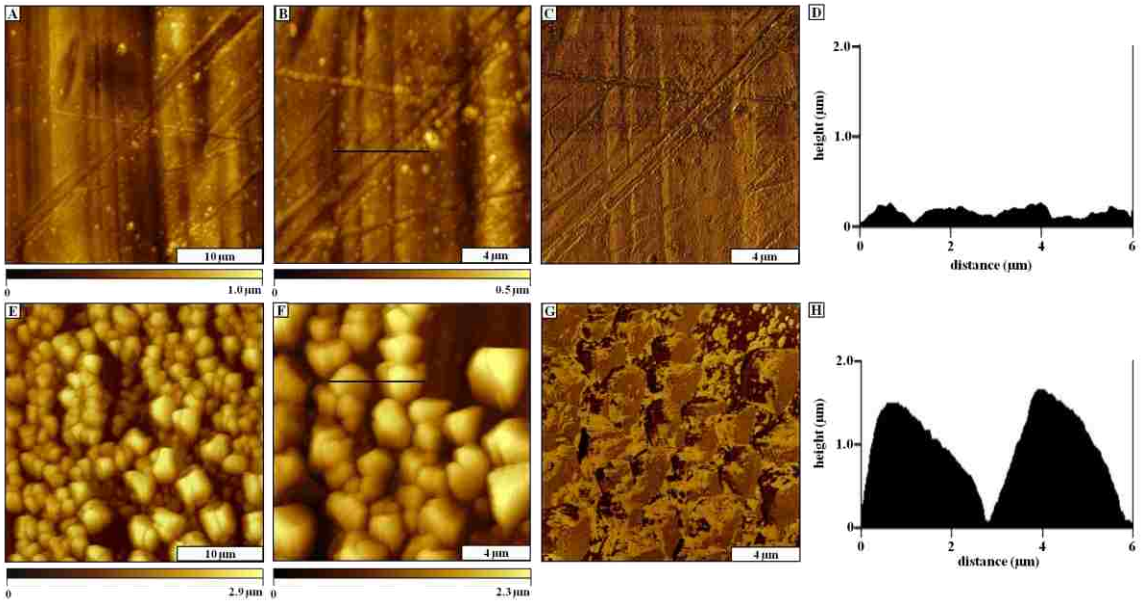

Figure 6.2 Changes on copper surfaces after exposure to water at pH 7, revealed by AFM. Top row images were obtained after 6 h immersion: [A] 30×30 μm^2 topograph; [B] 15×15μm^2 topograph; [C] corresponding phase image; [D] cursor profile for **B**. Bottom row images acquired after 24 h immersion: [E] 30×30 μm^2 topograph; [F] 15×15 μm^2 topograph; [G] phase image for **F**; [H] height profile for the line in **F.**

After 24 h of immersion time at pH 7, further growth of corrosion by-products formed on the copper surface as displayed in Figures 6.2E and 6.2F. The deposits are larger and cover most

of the surface (~87%). The angular shape of the surface crystals is characteristic of cuprite (Cu_2O). The smaller deposits appear to have grown together to form larger, multifaceted islands. The phase image (Figure 6.2G) provides a view of smaller deposits that are otherwise masked by topographic scaling effects. A line profile across two clusters measures 1.5 µm and 1.7 µm in height (Figure 6.2H), and the color scale ranges up to 2.9 µm for the adsorbate thickness in Figure 6.2E.

The next set of images reveal surface changes when 6 mg/L orthophosphate was added to the water samples at pH 7 (Figure 6.3). Within 6 h of immersion, ~ 92% of the copper surface is coated with small globular features as revealed in Figure 6.3A. A closer view (Figure 6.3B) the precipitates are fairly uniform in height and size. Within the corresponding phase image in Figure 6.3C, there are distinct changes in surface contrast from bright to dark colors; however this could be attributed to effects of either geometry or composition. The local surface roughness measured at 0.099 µm, which is a slight increase in comparison to the sample of Figure 6.2B. The height of the surface deposits ranges from 0.40 to 0.45 µm (Figure 6.3D) for the phosphate treated surface. As a result of the addition of orthophosphate, the surface coverage and thickness of deposits is greater after 6 h.

After 24 h immersion, the evolution of larger islands was not evident, as shown in Figure 6.3E and 6.3F. Approximately 90% of the surface is covered with small deposits, similar to the results after 6 h immersion. The clusters are larger in the lateral dimension however the cursor profile shows little change in the height for the deposits (Figure 6.3H), which measures 0.5 µm in thickness. Comparing these results with surfaces in the absence of orthophosphate, the progressive growth of larger islands was not observed. It appears that a thin film of phosphate-containing deposits forms throughout the surface, which mitigates the growth of cuprite or copper by-products.

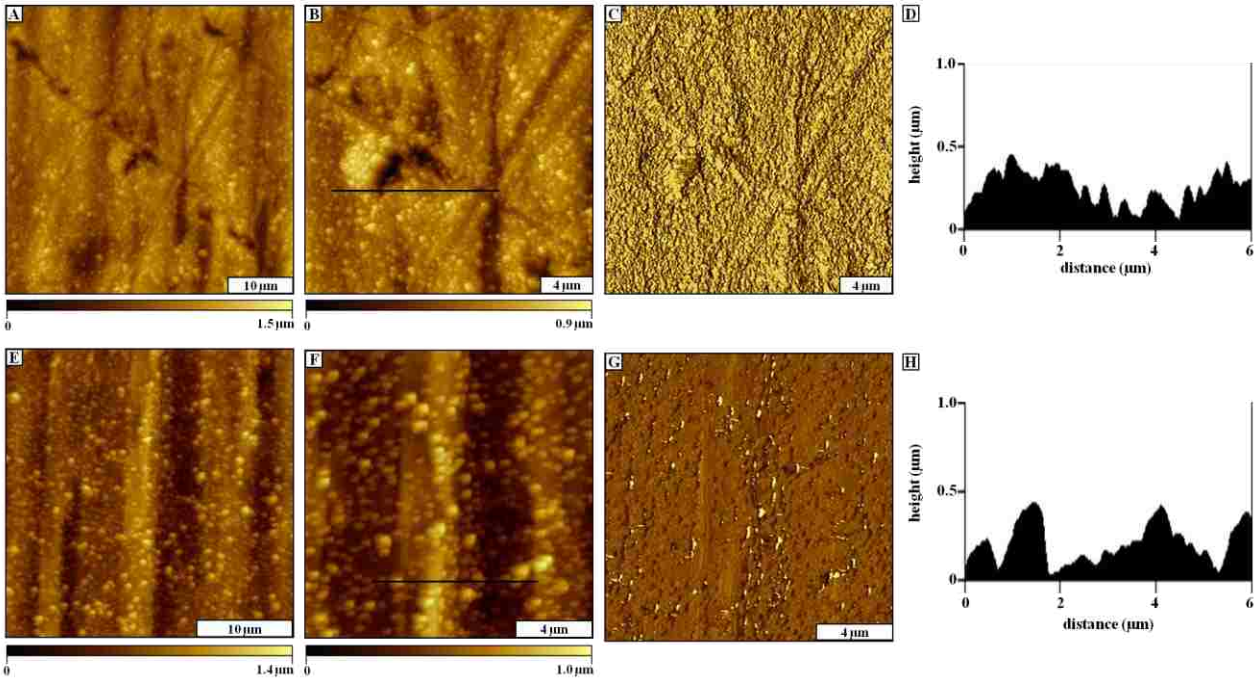

Figure 6.3 Surface changes with orthophosphate added as a corrosion inhibitor. Top row, after 6 h of surface treatment: [A] 30×30 µm^2 topograph; [B] 15×15µm^2 topograph; [C] corresponding phase image; [D] cursor profile for the line in **B**. Bottom row shows changes after 24 h immersion: [E] 30×30 µm^2 topograph; [F] 15×15 µm^2 view; [G] corresponding phase image; [H] cursor plot for the line **F**.

For samples immersed in synthetic water without orthophosphate at pH 8, surface changes are evident after 6 h as shown in Figures 6.4A and 6.4B. As compared to the smooth, angular crystal facets of Figure 6.2, the deposits formed at higher pH shown in Figure 6.4 have a smaller, grainy and clustered morphology. This likely occurs from differences in nucleation and growth of deposits in alkaline conditions. The clusters of solids measures approximately 0.2-0.5 µm in height and cover nearly the entire surface. After longer immersion for 24 h at pH 8, the surface density and height increased for the solid deposits (Figures 6.4D and 6.4E). Scratches and defects that were present in the previous images were no longer visible as the surface film increased in height and coverage.

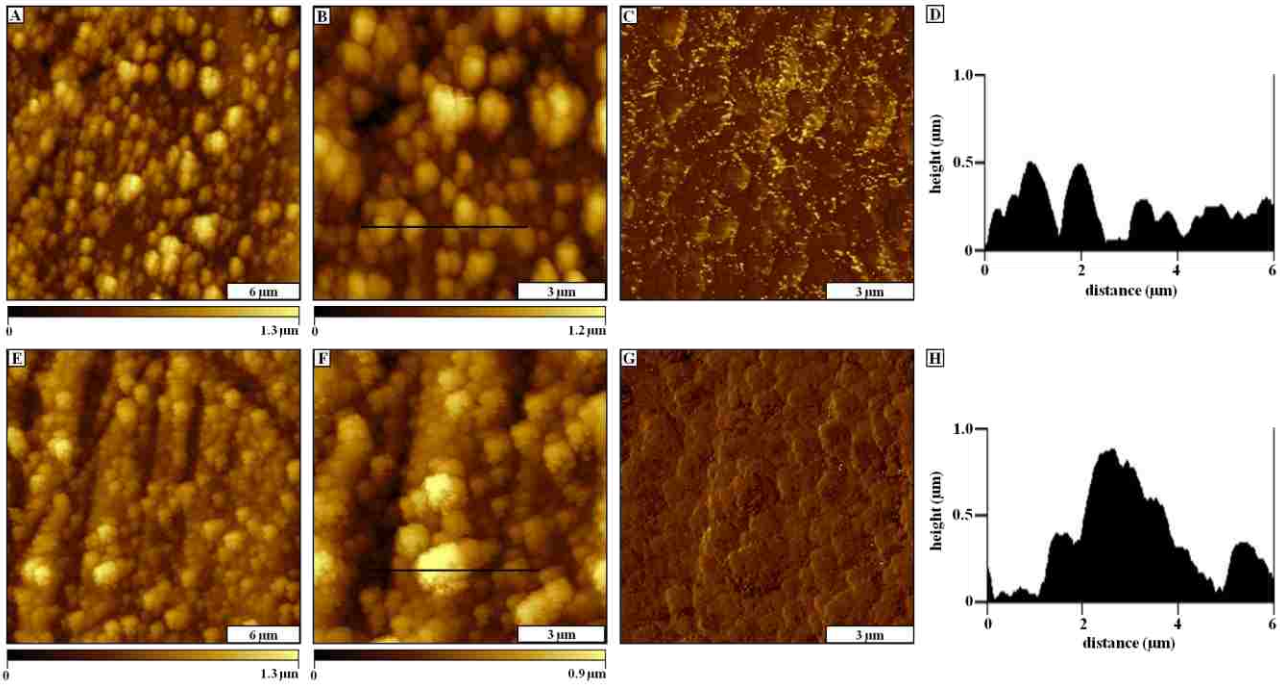

Figure 6.4 Copper surfaces after immersion in simulated drinking water at pH 8. After 6 h of water immersion: [A] 20×20 µm^2; [B] 10×10 µm^2 AFM topographs; [C] corresponding phase image;]D] cursor profile of **B**. Topography images after 24 h of treatment: [E] 20×20 µm^2; [F] 10×10 µm^2 area; [G] corresponding phase image; [H] height profile for the line in **F**.

Surface changes after the addition of orthophosphate at pH 8 are demonstrated in Figure 6.5. It is immediately apparent that there is lower coverage of solid deposits on the surface (Figures 6.5A and 6.5B) in comparison to samples without phosphate. The characteristic scratches and grooves of the underlying copper substrate are evident, as reference landmarks. With a zoom in view of the area (Figure 6.5B) small globular structures dispersed across areas of the surface are revealed. Distinct changes between the bare substrate and deposits can be resolved in the phase image of Figure 6.5C, indicating that the adsorbates have a different chemical nature than the underlying substrate. The height of the deposits measured 100-300 nm in Figure 6.5B, with the color scales ranging up to 0.6-1.7 µm for the image heights. The estimated surface coverage for Figure 6.5B was 52% for the surface deposits.

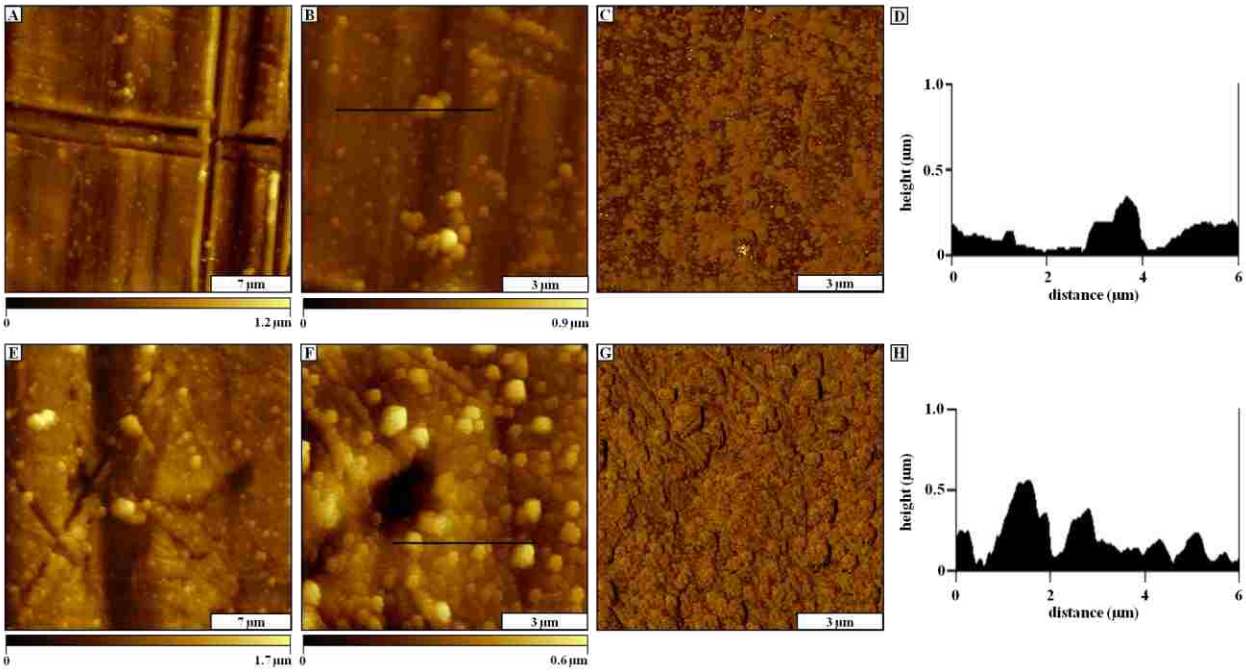

Figure 6.5 Effects of orthophosphate at pH 8. [A] Wide area view (25×25 µm^2) of a copper substrate after 6 h of exposure; [B] zoom-in view (10×10 µm^2); [C] corresponding phase image; [D] cursor profile for **B**. Views after 24 h: [E] 25×25 µm^2; [F] 10×10 µm^2; [G] corresponding phase image; [H] Cursor for the line in **F**.

After 24 h immersion at pH 8 with 6 mg/L of orthophosphate, the precipitates were observed to grow in dimension and increase in surface coverage (Figures 6.5E and 6.5F). The corresponding phase image is displayed in Figure 6.5G, showing uniformity in surface coverage of the phosphate-based surface coating. A representative line profile in Figure 6.5F indicates heights ranging from 0.1 to 0.7 µm. A direct comparison of the topographs of Figures 6.4E and 6.4F suggests that at pH 8 less growth and smaller deposits are apparent for phosphate-treated (Figure 6.5E and 6.5F) samples.

A side-by-side comparison of the surface changes after 24 h immersion over a pH range from 6.5 to 9, for water chemistries in the presence or absence of orthophosphate are shown in Figure 6.6. The images shown in Figure 6.6 are 5×5 µm^2 topography views. Without orthophosphate, large deposits formed at pH 6.5, 7 and 8. However, as the pH was increased to 9 the morphology and size changed to smaller structures. This trend suggests that the growth and

formation of the copper by-products without orthophosphate is pH dependent, under alkaline conditions the surface changes were the opposite of those observed at slightly acidic pH 6. With the addition of orthophosphate at all pH values, a decrease in size and density of surface deposits was observed. The addition of orthophosphate was shown to reduce the size of the solid deposits regardless of pH.

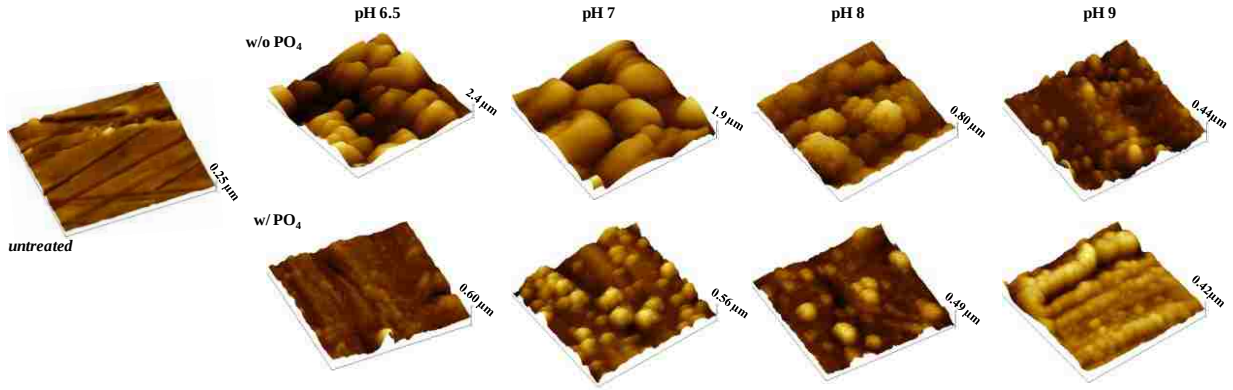

Figure 6.6 Morphology changes of copper surfaces after 24 h immersion in synthetic drinking water. A clean, untreated copper surface is shown at the far left. The upper row shows the growth of deposits in the absence of phosphate; the bottom row shows changes with the addition of orthophosphate.

6.3.2 Characterization of Surface Chemistry with XRD Analysis

Studies with XRD were used to identify the composition of the surface deposits observed with AFM for samples immersed for 24 h (Figure 6.7). Several peaks were observed within the spectrum with the strongest primarily for the pure copper metal. Peaks for cuprite were the only other detectable mineral for copper samples immersed in water without phosphate treatment. Interestingly, the XRD patterns also show a small signal for cuprite for substrates immersed in water containing orthophosphate. For samples with orthophosphate, the signal corresponding to the mineral cuprite was significantly reduced compared with all other pH values at 24 h without orthophosphate. The XRD patterns confirm that the addition of orthophosphate at pH 6.5, 7, 8 and 9 reduces the growth of cuprite on copper.

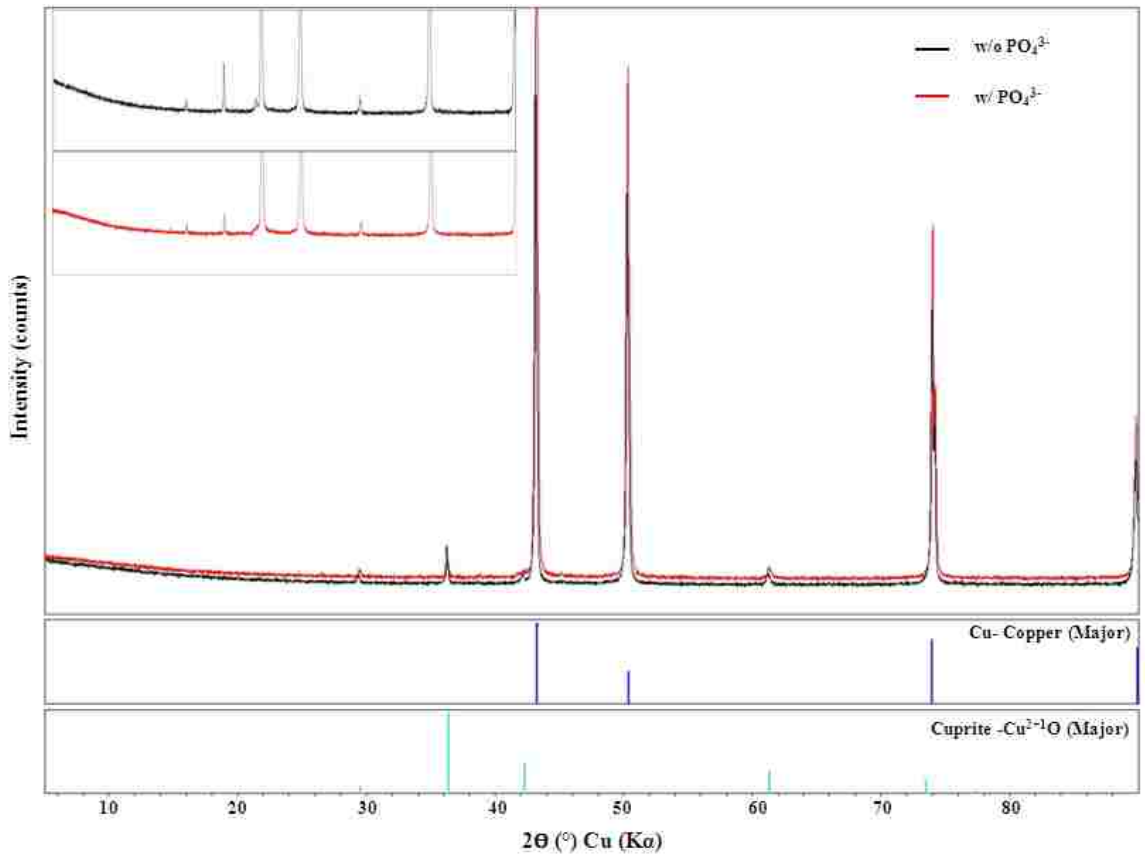

Figure 6.7 Spectra acquired with XRD for copper surfaces immersed for 24 h in water at pH 7.

6.3.3 NEXAFS Surface Characterizations

For copper samples immersed for 24 h at pH 6.5, 7, 8 and 9, NEXAFS spectra were obtained for samples treated with and without orthophosphate and compared with Cu_2O and CuO standards (Figure 6.8). A surface area ranging from 10-20 nm was scanned to determine the extent of oxidation of the copper surface. Figure 6.8A shows a series of spectra for coupons immersed in water without orthophosphate. The copper oxide (CuO) standard showed two distinctive peaks at 934 and 954 eV. The two peaks in this case are a result of the dipole transition of the $2p_{3/2}$ (L_{III}) and $2p_{1/2}$ (L_{II}) in Cu(II) ions.[268] The standard copper coupon displayed peaks at 938 and 957 eV, and these features are likely due to Cu^0 ions.[269]

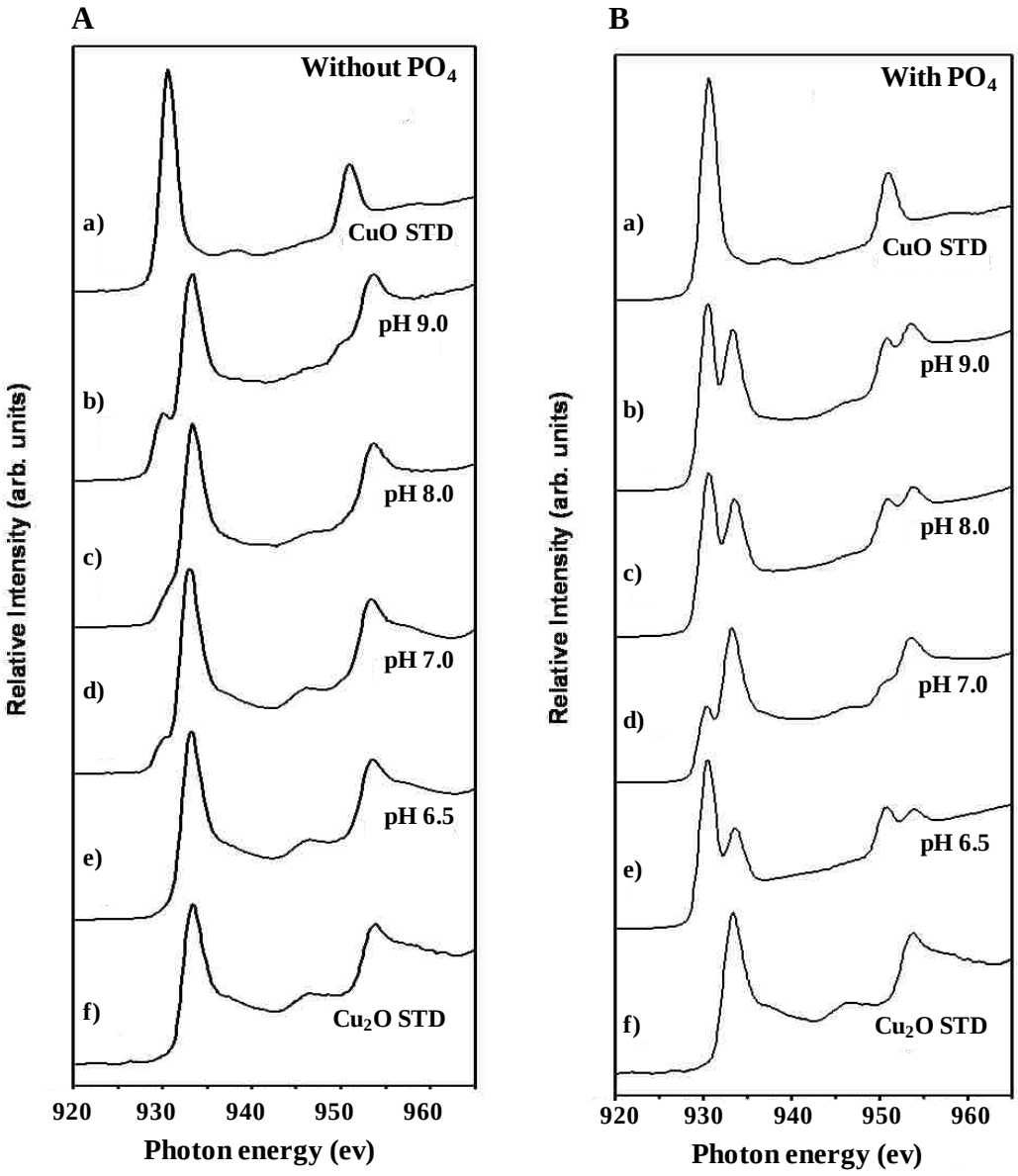

Figure 6.8 Comparison of NEXAFS spectra for copper surfaces after 24 h immersion at pH ranging from 6.5-9. [A] without orthophosphate; [B] with orthophosphate.

NEXAFS spectra from copper surfaces after 24 h of immersion at pH 6.5, 7, 8 and 9 without orthophosphate show a slight shift in the peak to the left (937 eV) as compared to the copper standard. This shift is indicative that the surface of copper coupon has been partially oxidized to Cu(I). However, as the pH increases, a closer look at the spectrum reveals small shoulder peaks at pH 7, 8, and 9, which correspond with the CuO standard. This indicates that

some part of copper samples have been oxidized to Cu(II). The NEXAFS spectra of copper surfaces that were immersed in water with orthophosphate are depicted in Figure 6.8B. There is no significant shift in the features of the sample coupons compared with the copper standard but there is an abundance in the presence of CuO within the spectrum. This indicates that the copper coupons are more easily oxidized to Cu(II) in the presence of orthophosphate, rather than without it. Moreover, as the pH increases, the intensity of features of Cu(II) increases.

6.3.4 FTIR Analysis of Treated Copper Samples

Fourier transform infrared absorbance spectra were taken of coupons at different pH values for samples treated with orthophosphate, to detect the adsorption of phosphorus to copper as a corrosion inhibitor. A spectral overlay is shown in Figure 6.9 for different samples that were treated for 24 h. The top peak in the graph is the control sample, which was not exposed to orthophosphate. The FTIR spectra for the sample without orthophosphate, an absorption band at 615 cm^{-1} was observed. This peak corresponds to the absorption band of Cu_2O.[270] This confirms that the copper was oxidized to Cu_2O as a result of surface corrosion. The intensity of the Cu_2O peak may result from orthophosphate treatment, shown in the bottom spectrum. The intensity of the absorption band at 620 cm^{-1} changes with pH, and there is also a broad peak at 1020 cm^{-1}.

In previous reports, the absorption bands near 1100 cm^{-1} and 1000 cm^{-1} have been assigned to $P\text{-}O^-$ groups, the phosphate non-bridging oxygen portion of PO_4 tetrahedra in a chain structure. For our study, the sample with orthophosphate present in the water, an absorption peak was found in the range of 1025 cm^{-1} confirming the presence of $P\text{-}O^-$ groups.[271] The decrease in intensity for the absorption peak originating from Cu_2O is also indicative of the phosphate group. However, there is no noticeable shift observed in the wavenumber values of the Cu_2O absorption peaks.

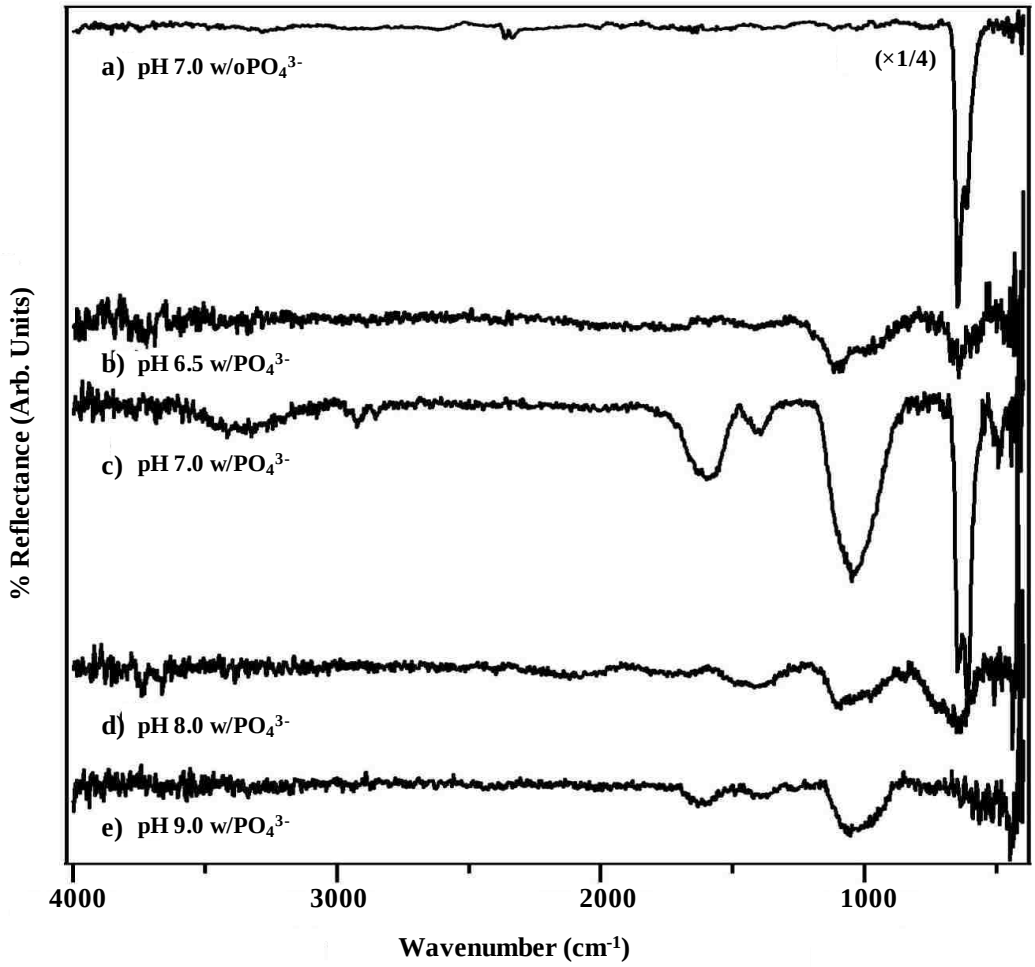

Figure 6.9 Comparison of surface changes observed with FTIR spectra for samples treated with water containing orthophosphate.

Presumably the interaction between Cu_2O and phosphate group is weak. The peaks appeared at 3325 and 3418 cm^{-1} results from bending and 1600 cm^{-1} is due to the stretching vibrational mode of the O-H bond that resides in water.

6.4 Discussion

Nanoscale morphology changes of the corroding copper surfaces after exposure to synthetic drinking water were characterized using AFM, FTIR and NEXAFS analysis. Investigations revealed that the morphology of the solids formed on copper surfaces depend on

water composition and contact time. As the immersion time was increased to 24 h for pH 6.5 and 7, dense, angular structures formed on coupon surfaces. At pH 8 and 9 after 24 h, the morphology changed into clustered, grainy morphologies. With addition of orthophosphate, smaller deposits were observed for each pH range.

Data from NEXAFS indicate that the film on the coupon surface is a layer of cuprite (Cu_2O). The two spectra in Figure 6.8, show pH dependent changes in the presence or absence of the phosphate inhibitor. The only detectable corrosion by-product that formed on the copper coupon was Cu_2O, and no Cu(II) phases were identified with XRD analysis. This was interesting because CuO was detected with NEXAFS. It is possible that Cu(II) crystal phases formed but were not detectable by XRD. The ratio of Cu:Cu_2O displayed a decreasing trend with time, suggesting Cu_2O is passivating the pure copper surface.

6.5 Conclusion

Without the phosphate inhibitor, the surface morphology of treated copper surfaces exhibited growth of large crystalline facets of copper by-products at pH 7 within 24 h. As the pH was increased from 7 to 8, in the absence of orthophosphate, solid deposits were apparent with heights less than 800 nm. With the addition of orthophosphate to the water, For all tested pH values, characterizations with AFM revealed a reduction in the growth and morphology of copper corrosion by-products. The chemical composition and oxidation state of the copper by-products viewed by AFM were identified by complementary characterizations with XRD, NEXAFS, and FTIR. Results from these additional techniques determined that the by-products were cuprite (Cu(I)) for samples without orthophosphate. However, copper coupons with the inhibitor produce a mixed oxidation state with the primary state being the pure metal, Cu(0).

CHAPTER 7. SUMMARY AND FUTURE PROSPECTUS

The research presented emphasizes results of fundamental studies with high resolution scanning probe microscopy for micro and nanoscopic measurements of materials. High resolution SPM imaging provides direct views of the surface morphology of samples of ferritin nanopatterns and furnishes molecular-level views of precipitates formed by chemical treatments of copper surfaces. The development of magnetic sample modulation AFM, has provided an alternative aproach for investigating the magnetic behavior of the iron storage protein, ferritin. The use of SPM for nanoscale studies of systematic changes in the morphology of copper surfaces that occur during the early stages of water corrosion processes was also achieved. Characterization with various AFM imaging modes such as MSM-AFM, conductive probe AFM, and phase imaging as demonstrated in this dissertation, shows the versatility of this surface technique for obtaining structural and physical information with nanometer resolution.

Ferritin is a supermolecular protein that has been used as a biosynthetic reactor to facilitate the growth of a range of nanomaterials,[272, 273] as an iron oxide nanoparticle,[274, 275] a nanodevice and for measuring binding and adhesions interactions[276] with other biomolecules. Due the nanometer dimensions of ferritin, SPM can be used to obtain molecular-level information of the protein. To maximize the potential of ferritin in applications, it is important to develop approaches to control the placement of the protein on various surfaces. The key is identifying patterning methods that will produce ferritin nanostructures with the desired shapes and sizes precisely and reproducibly without denaturing the protein.

Two high-throughput approaches for protein lithography were demonstrated to be suitable for fabricating structures of ferritin. Capillary filling of microchannels with PDMS molds were used to produce microline patterns of ferritin on glass substrates. Particle lithography with silica mesospheres was applied successfully to reproducibly generate arrays of ferritin ring

nanostructures, exhibiting relatively few defects and long-range periodicity. These designed test structures of ferritin were used for multiple successive SPM measurements, including studies with tapping-mode AFM, phase imaging and MSM-AFM.

For nanomagnetic materials, such as the Fe_2O_3 present in ferritin, a clear understanding of relationships between particle shape and size, surface structure and the resulting magnetic properties have not been well-studied at the molecular level. The properties of magnetic nanostructures cannot necessarily be inferred from scaled down properties of bulk materials, because of the cooperative effects of self-aggregation. The new approach for MSM-AFM combined with nanoscale lithography has facilitated measurements at the level of individual nanoparticles or proteins. The small dimensions of the nanoparticles can result in unique magnetic phenomena which are different than properties of bulk samples.[277]

Methods for investigating magnetic properties and measuring the magnetic response of nanomaterials as a function of size, chemical environment and temperature are important for both understanding the behavior of existing nanomaterials as well as for advancements in the synthesis of new nanomaterials with designed properties. Ferritin is ferromagnetic but due to the size of the material encapsulated within the cavity, this material is known to exhibit superparamagnetic properties when an external magnetic field is applied. Magnetic sample modulation (MSM), a newly developed AFM imaging mode, was applied for measuring the vibrational response of magnetic ferritin when the flux of an alternating electromagnetic field is applied to the sample. One of the key goals met with this research was to develop a scalable patterning approach with particle lithography for size-dependent measurements of magnetic properties. Despite the challenges for organizing proteins on biochip surfaces at the molecular scale, particle lithography was successfully applied for preparing regularly spaced surface structures of proteins, with high surface density. Future experiments will be to develop dynamic

experimental protocols with MSM for placing the AFM probe directly in contact with a single ferritin molecule on the surface, to obtain frequency spectra for the vibration of individual protein. The amplitude responses will be acquired as the field strength is incrementally increased as an indirect measurement of magnetic susceptibility.

Characterization of the size, morphology and speciation of copper precipitates formed during corrosion was investigated in Chapter 6. The impact of water quality for the early stages of surface corrosion as influenced by parameters of pH, dissolved inorganic carbon (DIC) and orthophosphate was evaluated as a function of time. The studies in Chapter 6 conducted in collaboration with the USEPA provide insight into the release of copper from distribution systems. Further research with SPM studies are in progress, to gain fundamental information of the rates and mechanisms of corrosion processes.

Since corrosion results from both electrochemical and physical processes caused by a potential difference between an anode and cathode, investigations with current sensing AFM (CS-AFM) are appropriate. Current sensing AFM can be applied for studying the variation of conductivity in resistive samples. This technique enables direct and simultaneous mapping of the surface topography with generating a current image of metal surfaces. The CS-AFM technique requires cantilevers coated with a conductive metal film and is operated in the standard AFM contact mode. Applying a bias voltage between the substrate and conducting AFM probe generates the flow of current, which is sensitively measured with an amplifier placed within the tip-holder assembly. The current generated can be used to construct a spatially resolved conductivity image, for scaling measurements in the range from femto- to nearly micro-amperes.[278, 279] The typical lateral resolution of CS-AFM achieved is 10 nm, depending on the geometry of the AFM probe. Switching the bias voltage reverses the contrast in current images.

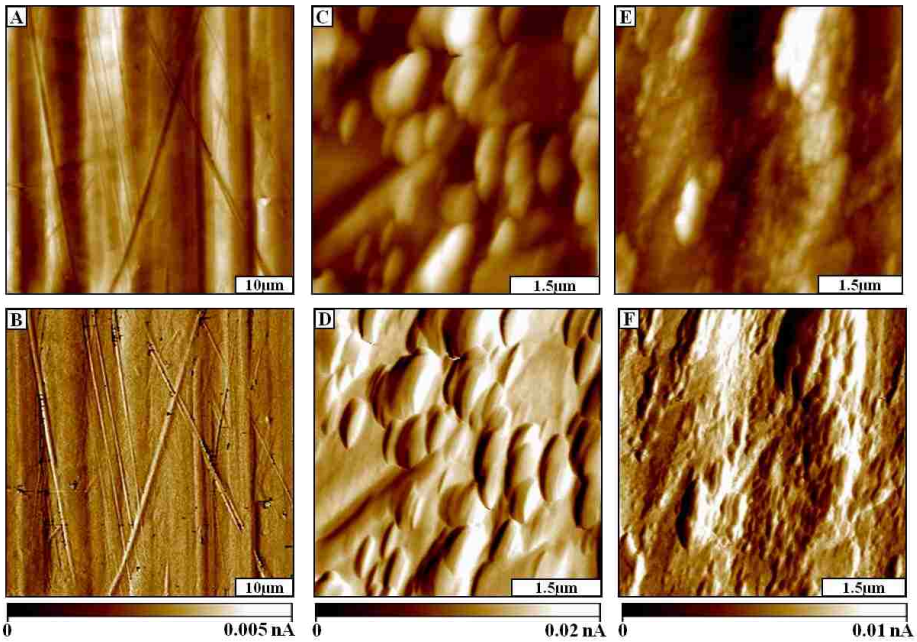

Figure 7.1 Current sensing AFM images of copper surfaces after 24 h exposure to water. [A] topograph of an untreated, clean copper coupon; [B] corresponding current image for **A**; [C] topography view of coupon treated at pH 6.5 in water without orthophosphate; [D] simultaneously acquired current image for **C**; [E] topography frame of copper coupon exposed to water containing 6 mg/L of orthophosphate; [F] corresponding current image for **E**.

Spectra of current-voltage (I-V) profiles can be acquired at selected points within an image frame using CS-AFM.

Studies of copper surface corrosion with CS-AFM have not been previously reported. Preliminary proof-of-concept data demonstrating the applicability of CS-AFM to investigate surface changes are shown in Figure 7.1 Studies with CS-AFM were accomplished with clean copper coupons immersed in treated waters without and with orthophosphate at pH 6.5, after 24 h immersion. For the clean copper coupon a bias of -0.01 V was applied for the topography and current image shown in Figures 7.1A and 7.1B, respectively. The challenge with imaging the copper coupons is that the copper is highly conductive thus a very small sample bias was needed to for measurements. However, the output signal exceeded the saturation limit of the detector. Current images were acquired three samples, as proof-of-concept. Further work is planned at the USEPA laboratory for continuing this project.

REFERENCES

1. Binnig, G.; Quate, C. F.; Gerber, C. Atomic force microscope. *Phys. Rev. Lett.* **1986,** *56,* 930-933.

2. Giessibl, F. J. Advances in atomic force microscopy. *Rev. Mod. Phys.* **2003,** *75*, 949-983.

3. Tsukruk, V. V.; Bliznyuk, V. N. Adhesive and friction forces between chemically modified silicon and silicon nitride surfaces. *Langmuir* **1998,** *14*, 446-455.

4. vanderVegte, E. W.; Hadziioannou, G. Scanning force microscopy with chemical specificity: An extensive study of chemically specific tip-surface interactions and the chemical imaging of surface functional groups. *Langmuir* **1997,** *13*, 4357-4368.

5. Grandbois, M.; Beyer, M.; Rief, M.; Clausen-Schaumann, H.; Gaub, H. E. How strong is a covalent bond? *Science* **1999,** *283*, 1727-1730.

6. Noy, A.; Frisbie, C. D.; Rozsnyai, L. F.; Wrighton, M. S.; Lieber, C. M. Chemical force microscopy-exploiting chemically-modified tips to quantify adhesion, friction, and functional-groups distributions in molecular assemblies. *J. Am. Chem. Soc.* **1995,** *117*, 7943-7951.

7. Tang, W.; Bhushan, B.; Ge, S. Friction, adhesion and durability and influence of humidity on adhesion and surface charging of skin and various skin creams using atomic force microscopy. *J. Microsc. -OXFORD* **2010,** *239*, 99-116.

8. Jacobs, H. O.; Knapp, H. F.; Muller, S.; Stemmer, A. Surface potential mapping: A qualitative material contrast in SPM. *Ultramicroscopy* **1997,** *69*, 39-49.

9. Moser, A.; Hug, H. J.; Parashikov, I.; Stiefel, B.; Fritz, O.; Thomas, H.; Baratoff, K.; Guntherodt, H. J.; Chaudhari, P. Observation of single vortices condensed into a vortex-glass phase by magnetic force microscopy. *Phys. Rev. Lett.* **1995,** *74*, 1847-1850.

10. Fotiadis, D.; Scheuring, S.; Muller, S. A.; Engel, A.; Muller, D. J. Imaging and manipulation of biological structures with the AFM. *Micron* **2002,** *33*, 385-397.

11. Daniels, S. L.; Ngunjiri, J. N.; Garno, J. C. Investigation of the magnetic properties of ferritin by AFM imaging with magnetic sample modulation. *Anal. Bioanal. Chem.* **2009,** *394*, 215-223.

12. Daniels, S. L.; Kizilkaya, O.; Lytle, D. A.; Garno, J. C. Surface characterization of the early stages on aqueous copper corrosion: Effects of immersion interval and orthophosphate concentration. *Appl. Surf. Sci.* **2011,** *submitted*.

13. Binnig, G.; Rohrer, H. Scanning tunneling microscopy *Helv. Phys. Acta* **1982,** *55*, 726-735.

14. Binnig, G.; Rohrer, H. Scanning tunneling microscopy - From birth to adolescence *Rev. Mod. Phys.* **1987,** *59*, 615-625.

15. Engel, A.; Lyubchenko, Y.; Muller, D. Atomic force microscopy: A powerful tool to observe biomolecules at work. *Trends Cell Biol.* **1999,** *9*, 77-80.

16. Hofer, W. A.; Foster, A. S.; Shluger, A. L. Theories of scanning probe microscopes at the atomic scale. *Rev. Mod. Phys.* **2003,** *75*, 1287-1331.

17. Garcia, R.; Perez, R. Dynamic atomic force microscopy methods. *Surf. Sci. Rep.* **2002,** *47*, 197-301.

18. Radmacher, M.; Tillmann, R. W.; Fritz, M.; Gaub, H. E. From molecules to cells-imaging soft samples with the atomic force microscope. *Science* **1992,** *257*, 1900-1905.

19. Lindsay, S. M.; Nagahara, L. A.; Thundat, T.; Knipping, U.; Rill, R. L.; Drake, B.; Prater, C. B.; Weisenhorn, A. L.; Gould, S. A. C.; Hansma, P. K. STM and AFM images of nucleosome DNA under water. *J. Biomol. Struct. Dyn.* **1989,** *7*, 279-287.

20. Moller, C.; Allen, M.; Elings, V.; Engel, A.; Muller, D. J. Tapping-mode atomic force microscopy produces faithful high-resolution images of protein surfaces. *Biophys. J.* **1999,** *77*, 1150-1158.

21. Thomson, N. H.; Fritz, M.; Radmacher, M.; Cleveland, J. P.; Schmidt, C. F.; Hansma, P. K. Protein tracking and detection of protein motion using atomic force microscopy. *Biophys. J.* **1996,** *70*, 2421-2431.

22. Stark, R. W.; Schitter, G.; Stemmer, A. Tuning the interaction forces in tapping mode atomic force microscopy. *Phys. Rev. B* **2003,** *68*.

23. Putman, C. A. J.; Vanderwerf, K. O.; Degrooth, B. G.; Vanhulst, N. F.; Greve, J. Viscoelasticity of living cells allows high-resolution imaging by tapping mode atomic-force microscopy. *Biophys. J.* **1994,** *67*, 1749-1753.

24. Hansma, H. G.; Vesenka, J.; Siegerist, C.; Kelderman, G.; Morrett, H.; Sinsheimer, R. L.; Elings, V.; Bustamante, C.; Hansma, P. K. Reproducible imaging and dissection of plasmid DNA under liquid with the atomic force microscope. *Science* **1992,** *256*, 1180-1184.

25. Lyubchenko, Y. L.; Shlyakhtenko, L. S. Visualization of supercoiled DNA with atomic force microscopy in situ. *Proc. Natl. Acad. Sci. U.S.A.* **1997,** *94*, 496-501.

26. Kasas, S.; Thomson, N. H.; Smith, B. L.; Hansma, H. G.; Zhu, X. S.; Guthold, M.; Bustamante, C.; Kool, E. T.; Kashlev, M.; Hansma, P. K. Escherichia coli RNA polymerase activity observed using atomic force microscopy. *Biochem.* **1997,** *36*, 461-468.

27. Fritz, J.; Anselmetti, D.; Jarchow, J.; FernandezBusquets, X. Probing single biomolecules with atomic force microscopy. *J. Struct. Biol.* **1997,** *119*, 165-171.

28. Fisher, T. E.; Oberhauser, A. F.; Carrion-Vazquez, M.; Marszalek, P. E.; Fernandez, J. M. The study of protein mechanics with the atomic force microscope. *Trends Biochem. Sci.* **1999,** *24*, 379-384.

29. Rotsch, C.; Radmacher, M. Drug-induced changes of cytoskeletal structure and mechanics in fibroblasts: An atomic force microscopy study. *Biophys. J.* **2000,** *78*, 520-535.

30. A-Hassan, E.; Heinz, W. F.; Antonik, M. D.; D'Costa, N. P.; Nageswaran, S.; Schoenenberger, C. A.; Hoh, J. H. Relative microelastic mapping of living cells by atomic force microscopy. *Biophys. J.* **1998,** *74*, 1564-1578.

31. Alessandrini, A.; Facci, P. AFM: A versatile tool in biophysics. *Meas. Sci. Technol.* **2005,** *16*, R65-R92.

32. Arosio, P.; Ingrassia, R.; Cavadini, P. Ferritins: A family of molecules for iron storage, antioxidation and more. *Biochim. Biophys. Acta, Gen. Subj.* **2009,** *1790*, 589-599.

33. James, C. D.; Davis, R. C.; Kam, L.; Craighead, H. G.; Isaacson, M.; Turner, J. N.; Shain, W. Patterned protein layers on solid substrates by thin stamp microcontact printing. *Langmuir* **1998,** *14*, 741-744.

34. Bernard, A.; Delamarche, E.; Schmid, H.; Michel, B.; Bosshard, H. R.; Biebuyck, H. Printing patterns of proteins. *Langmuir* **1998,** *14*, 2225-2229.

35. Blawas, A. S.; Oliver, T. F.; Pirrung, M. C.; Reichert, W. M. Step-and-repeat photopatterning of protein features using caged/biotin-BSA: Characterization and resolution. *Langmuir* **1998,** *14*, 4243-4250.

36. Dontha, N.; Nowall, W. B.; Kuhr, W. G. Generation of biotin/avidin/enzyme nanostructures with maskless photolithography. *Anal. Chem.* **1997,** *69*, 2619-2625.

37. Palacin, S.; Hidber, P. C.; Bourgoin, J. P.; Miramond, C.; Fermon, C.; Whitesides, G. M. Patterning with magnetic materials at the micron scale. *Chem. Mater.* **1996,** *8*, 1316-1325.

38. Garno, J. C.; Amro, N. A.; Wadu-Mesthrige, K.; Liu, G.-Y. Production of periodic arrays of protein nanostructures using particle lithography. *Langmuir* **2002,** *18*, 8186-8192.

39. Li, J. R.; Henry, G. C.; Garno, J. C. Fabrication of nanopatterned films of bovine serum albumin and staphylococcal protein A using latex particle lithography. *Analyst* **2006,** *131*, 244-250.

40. Ngunjiri, J. N.; Daniels, S. L.; Li, J. R.; Serem, W. K.; Garno, J. C. Controlling the surface coverage and arrangement of proteins using particle lithography. *Nanomedicine* **2008,** *3*, 529-541.

41. Cech, I.; Smolensky, M. H.; Afshar, M.; Broyles, G.; Barczyk, M.; Burau, K.; Emery, R. Lead and copper in drinking water fountains - Information for physicians. *Southern Med. J.* **2006,** *99*, 137-142.

42. Critchley, M. M.; Cromar, N. J.; McClure, N. C.; Fallowfield, H. J. The influence of the chemical composition of drinking water on cuprosolvency by biofilm bacteria. *J. Appl. Microbiol.* **2003,** *94*, 501-507.

43. Cuppett, J. D.; Duncan, S. E.; Dietrich, A. M. Evaluation of copper speciation and water quality factors that affect aqueous copper tasting response. *Chem. Senses* **2006,** *31*, 689-697.

44. Shim, J. J.; Kim, J. G. Copper corrosion in potable water distribution systems: influence of copper products on the corrosion behavior. *Mater. Lett.* **2004,** *58*, 2002-2006.

45. Tam, Y. S.; Elefsiniotis, P. Corrosion control in water supply systems: Effect of pH, alkalinity, and orthophosphate on lead and copper leaching from brass plumbing. *J. Environ. Sci. Health. Part A Toxic/Hazard. Subst. Environ. Eng.* **2009,** *44*, 1251-1260.

46. Boulay, N.; Edwards, M. Role of temperature, chlorine, and organic matter in copper corrosion by-product release in soft water. *Water Res.* **2001,** *35*, 683-690.

47. Cong, H. B.; Michels, H. T.; Scully, J. R. Passivity and pit stability behavior of copper as a function of selected water chemistry variables. *J. Electrochem. Soc.* **2009,** *156*, C16-C27.

48. Schock, M. R.; Lytle, D. A.; Sandvig, A. M.; Clement, J.; Harmon, S. M. Replacing polyphosphate with silicate to solve lead, copper, and source water iron problems. *J. Am. Water Works Assn.* **2005,** *97*, 84-93.

49. Edwards, M.; Hidmi, L.; Gladwell, D. Phosphate inhibition of soluble copper corrosion by-product release. *Corros. Sci.* **2002,** *44*, 1057-1071.

50. Binnig, G.; Rohrer, H.; Gerber, C.; Weibel, E. Tunneling through a controllable vacuum gap. *Appl. Phys. Lett.* **1982,** *40*, 178-180.

51. Liu, D. L.; Cheng, F. Advances in research on structural characterisation of agricultural products using atomic force microscopy. *J. Sci.Food Agric.* **2011,** *91*, 783-788.

52. Bhushan, B.; Tang, W. Surface, tribological, and mechanical characterization of synthetic skins for tribological applications in cosmetic science. *J Appl. Polym. Sci.* **2011,** *120*, 2881-2890.

53. Joseph, D. P.; Saravanan, M.; Muthuraaman, B.; Renugambal, P.; Sambasivam, S.; Raja, S. P.; Maruthamuthu, P.; Venkateswaran, C. Spray deposition and characterization of nanostructured Li doped NiO thin films for application in dye-sensitized solar cells. *Nanotechnology* **2008,** *19*.

54. Wiesendanger, R. Contributions of scanning probe microscopy and spectroscopy to the investigation and fabrication of nanometer-scale structures. *J. Vac. Sci. Technol., B* **1994,** *12*, 515-529.

55. Radmacher, M.; Tillmann, R. W.; Fritz, M.; Gaub, H. E. From molecules to cells - Imaging soft samples with the atomic force microscope. *Science* **1992,** *257*, 1900-1905.

56. Greene, M. E.; Kinser, C. R.; Kramer, D. E.; Pingree, L. S. C.; Hersam, M. C. Application of scanning probe microscopy to the characterization and fabrication of hybrid nanomaterials. *Microsc. Res. Techniq.* **2004,** *64*, 415-434.

57. Martin, Y.; Williams, C. C.; Wickramasinghe, H. K. Atomic force microscope force mapping and profiling on the sub 100-Å scale. *J. Appl. Phys.* **1987,** *61*, 4723-4729.

58. Martin, Y.; Wickramasinghe, H. K. Magnetic imaging by force microscopy with 1000-Å resolution. *Appl. Phys. Lett.* **1987,** *50*, 1455-1457.

59. Martin, Y.; Abraham, D. W.; Wickramasinghe, H. K. High-resolution capacitance measurement and potentiometry by force microscopy. *Appl. Phys. Lett.* **1988,** *52*, 1103-1105.

60. Nonnenmacher, M.; Oboyle, M. P.; Wickramasinghe, H. K. Kelvin probe force microscopy. *Appl. Phys. Lett.* **1991,** *58*, 2921-2923.

61. Zhong, Q.; Inniss, D.; Kjoller, K.; Elings, V. B. Fractured polymer silica fiber surface studied by tapping mode atomic-force microscopy. *Surf. Sci.* **1993,** *290*, L688-L692.

62. Rugar, D.; Yannoni, C. S.; Sidles, J. A. Mechanical detection of magnetic resonance. *Nature* **1992,** *360*, 563-566.

63. Zuger, O.; Rugar, D. Magnetic-resonance detection and imaging using force microscope techniques. *J. Appl. Phys.* **1994,** *75*, 6211-6216.

64. Dougherty, W. M.; Bruland, K. J.; Garbini, J. L.; Sidles, J. A. Detection of AC magnetic signals by parametric mode coupling in a mechanical oscillator. *Meas. Sci.Technol.* **1996,** *7*, 1733-1739.

65. Kelley, T. W.; Granstrom, E. L.; Frisbie, C. D. Conducting probe atomic force microscopy: A characterization tool for molecular electronics. *Adv. Mater.* **1999,** *11*, 261-+.

66. Li, J. R.; Lewandowski, B. R.; Xu, S.; Garno, J. C. Detecting the magnetic response of iron oxide capped organosilane nanostructures using magnetic sample modulation and atomic force microscopy. *Anal. Chem.* **2009,** *81*, 4792-4802.

67. Hafner, J. H.; Cheung, C. L.; Woolley, A. T.; Lieber, C. M. Structural and functional imaging with carbon nanotube AFM probes. *Prog. Biophys. Mol. Biol.* **2001,** *77*, 73-110.

68. Drake, B.; Prater, C. B.; Weisenhorn, A. L.; Gould, S. A. C.; Albrecht, T. R.; Quate, C. F.; Cannell, D. S.; Hansma, H. G.; Hansma, P. K. Imaging crystals, polymers, and processes in water with the atomic force microscope PE. *Science* **1989,** *243*, 1586-1589.

69. Hansma, P. K.; Elings, V. B.; Marti, O.; Bracker, C. E. Scanning tunneling microscopy and atomic force microscopy - Application to biology and technology. *Science* **1988,** *242*, 209-216.

70. Meyer, G.; Amer, N. M. Novel optical approach to atomic force microscopy. *Appl. Phys. Lett.* **1988,** *53*, 1045-1047.

71. Jalili, N.; Laxminarayana, K. A review of atomic force microscopy imaging systems: application to molecular metrology and biological sciences. *Mechatronics* **2004,** *14*, 907-945.

72. Mate, C. M.; McClelland, G. M.; Erlandsson, R.; Chiang, S. Atomic-scale friction of a t ungsten tip on a graphite surface. *Phys. Rev. Lett.* **1987,** *59*, 1942-1945.

73. Cappella, B.; Dietler, G. Force-distance curves by atomic force microscopy. *Surf. Sci. Rep.* **1999,** *34*, 1-+.

74. Aoki, T.; Hiroshima, M.; Kitamura, K.; Tokunaga, M.; Yanagida, T. Non-contact scanning probe microscopy with sub-piconewton force sensitivity. *Ultramicroscopy* **1997,** *70*, 45-55.

75. Weisenhorn, A. L.; Maivald, P.; Butt, H. J.; Hansma, P. K. Measuring adhesions, attraction, and repulsion between surfaces in liquids with an atomic-force microscope. *Phys. Rev. B* **1992,** *45*, 11226-11232.

76. Putman, C. A. J.; Vanderwerf, K. O.; Degrooth, B. G.; Vanhulst, N. F.; Greve, J. Tapping mode atomic-force microscopy in liquid. *Appl. Phys. Lett.* **1994,** *64*, 2454-2456.

77. Tamayo, J.; Garcia, R. Deformation, contact time, and phase contrast in tapping mode scanning force microscopy. *Langmuir* **1996,** *12*, 4430-4435.

78. Gotsmann, B.; Seidel, C.; Anczykowski, B.; Fuchs, H. Conservative and dissipative tip-sample interaction forces probed with dynamic AFM. *Phys. Rev. B* **1999,** *60*, 11051-11061.

79. Stark, M.; Moller, C.; Muller, D. J.; Guckenberger, R. From images to interactions: High-resolution phase imaging in tapping-mode atomic force microscopy. *Biophys. J.* **2001,** *80*, 3009-3018.

80. Achalla, P.; McCormick, J.; Hodge, T.; Moreland, C.; Esnault, P.; Karim, A.; Raghavan, D. Characterization of elastomeric blends by atomic force microscopy. *J. Polym. Sci. Pol. Phys.* **2006,** *44*, 492-503.

81. O'Neil, K. D.; Semenikhin, O. A. AFM phase imaging of thin films of electronically conducting polymer polybithiophene prepared by electrochemical potentiodynamic deposition. *Russ. Electrochem+* **2010,** *46*, 1345-1352.

82. Chen, X.; McGurk, S. L.; Davies, M. C.; Roberts, C. J.; Shakesheff, K. M.; Tendler, S. J. B.; Williams, P. M.; Davies, J.; Dawkes, A. C.; Domb, A. Chemical and morphological analysis of surface enrichment in a biodegradable polymer blend by phase-detection imaging atomic force microscopy. *Macromolecules* **1998,** *31*, 2278-2283.

83. de Pablo, P. J.; Gomez-Navarro, C.; Martinez, M. T.; Benito, A. M.; Maser, W. K.; Colchero, J.; Gomez-Herrero, J.; Baro, A. M. Performing current versus voltage measurements of single-walled carbon nanotubes using scanning force microscopy. *Appl. Phys. Lett.* **2002,** *80*, 1462-1464.

84. Fabre, B.; Hao, E. H.; LeJeune, Z. M.; Amuhaya, E. K.; Barriere, F.; Garno, J. C.; Vicente, M. G. H. Polythiophenes containing in-chain cobaltabisdicarbollide centers. *ACS Appl. Mater. Interfaces* **2010,** *2*, 691-702.

85. Barriere, F.; Fabre, B.; Hao, E. H.; LeJeune, Z. M.; Hwang, E.; Garno, J. C.; Nesterov, E. E.; Vicente, M. G. H. Electropolymerizable 2,2'-carboranyldithiophenes. Structure-property investigations of the corresponding conducting polymer films by electrochemistry, uv-visible spectroscopy and conducting probe atomic force microscopy. *Macromolecules* **2009,** *42*, 2981-2987.

86. Yang, G. H.; Tan, L.; Yang, Y. Y.; Chen, S. W.; Liu, G. Y. Single electron tunneling and manipulation of nanoparticles on surfaces at room temperature. *Surf. Sci.* **2005,** *589*, 129-138.

87. Cho, S. H.; Park, S. M. Electrochemistry of conductive polymers 39. Contacts between conducting polymers and noble metal nanoparticles studied by current-sensing atomic force microscopy. *J. Phys. Chem. B* **2006,** *110*, 25656-25664.

88. Gosvami, N.; Lau, K. H. A.; Sinha, S. K.; O'Shea, S. J. Effect of end groups on contact resistance of alkanethiol based metal-molecule-metal junctions using current sensing AFM. *Appl. Surf. Sci.* **2006,** *252*, 3956-3960.

89. Liu, G. D.; Wang, J.; Wu, H.; Lin, Y. H. Versatile apoferritin nanoparticle labels for assay of protein. *Anal. Chem.* **2006,** *78*, 7417-7423.

90. Dickson, D. P. E. Nanostructured magnetism in living systems. *J. Magn. Magn. Mater.* **1999,** *203*, 46-49.

91. Uchida, M.; Flenniken, M. L.; Allen, M.; Willits, D. A.; Crowley, B. E.; Brumfield, S.; Willis, A. F.; Jackiw, L.; Jutila, M.; Young, M. J.; Douglas, T. Targeting of cancer cells with ferrimagnetic ferritin cage nanoparticles. *J. Am. Chem. Soc.* **2006,** *128*, 16626-16633.

92. Uchida, M.; Klem, M. T.; Allen, M.; Suci, P.; Flenniken, M.; Gillitzer, E.; Varpness, Z.; Liepold, L. O.; Young, M.; Douglas, T. Biological containers: Protein cages as multifunctional nanoplatforms. *Adv. Mater.* **2007,** *19*, 1025-1042.

93. Chasteen, N. D.; Harrison, P. M. Mineralization in ferritin: An efficient means of iron storage. *J. Struct. Biol.* **1999,** *126*, 182-194.

94. Harrison, P. M.; Treffry, A.; Lilley, T. H. Ferritin as an iron-storage protein- mechanisms of iron uptake. *J. Inorg. Biochem.* **1986,** *27*, 287-293.

95. Uchida, M.; Kang, S.; Reichhardt, C.; Harlen, K.; Douglas, T. The ferritin superfamily: Supramolecular templates for materials synthesis. *Biochim. Biophys. Acta, Gen. Subj.* **2010,** *1800*, 834-845.

96. Andrews, S. C.; Arosio, P.; Bottke, W.; Briat, J.-F.; VonDarl, M.; Harrison, P. M.; Laulhere, J.-P.; Levi, S.; Lobreaux, S.; Yewdall, S. J. Structure, function, and evolution of ferritins. *Biochem.* **1992,** *47*, 161-174.

97. Theil, E. C. Ferritin: structure, gene-regulation, and cellular function in animals, plants and microorganisms. *Annu. Rev. Biochem.* **1987,** *56*, 289-315.

98. Laufberger, V. Contribution to the technique of renin seclusion. *C. R. Seances Soc. Biol. Fil.* **1937,** *126*, 107-109.

99. Wang, Z. M.; Li, C.; Ellenburg, M.; Soistman, E.; Ruble, J.; Wright, B.; Ho, J. X.; Carter, D. C. Structure of human ferritin L chain. *Acta Crystallogr. D* **2006,** *62*, 800-806.

100. Kleinwachter, V. X-ray diffraction study of ferritin-interpretation of low-angle scattering. *Arch.Biochem. Biophys.* **1964,** *105*, 352-&.

101. Hintze, K. J.; Theil, E. C. Cellular regulation and molecular interactions of the ferritins. *Cell. Mol. Life Sci.* **2006,** *63*, 591-600.

102. Harrison, P. M.; Arosio, P. Ferritins: Molecular properties, iron storage function and cellular regulation. *BBA-Bioenergetics* **1996,** *1275*, 161-203.

103. Theil, E. C. Ferritin - structure, gene-regulation, and cellular function in animals, plants and microorganisms. *Annu. Rev. Biochem.* **1987,** *56*, 289-315.

104. Granick, S. Ferritin - its properties and significance for iron metabolism. *Chem. Rev.* **1946,** *38*, 379-403.

105. Boyd, D.; Vecoli, C.; Belcher, D. M.; Jain, S. K.; Drysdale, J. W. Structural and functional-relationships of human ferritin-H and ferritin-L chains deduced from cDNA clones. *J. Biol. Chem.* **1985,** *260*, 1755-1761.

106. Farrant, J. L. An electron microscopic study of ferritin. *Biochim. Biophys Acta* **1954,** *13*, 569-576.

107. Pan, Y.-H.; Sader, K.; Powell, J. J.; Bleloch, A.; Gass, M.; Trinick, J.; Warley, A.; Li, A.; Brydson, R.; Brown, A. 3D morphology of the human hepatic ferritin mineral core: New evidence for a subunit structure revealed by single particle analysis of HAADF-STEM images. *J. Struct. Biol.* **2009,** *166*, 22-31.

108. Engel, A.; Muller, D. J. Observing single biomolecules at work with the atomic force microscope. *Nat. Struct. Biol.* **2000,** *7*, 715-718.

109. Moller, C.; Allen, M.; Elings, V.; Engel, A.; Muller, D. J. Tapping-mode atomic force microscopy produces faithful high-resolution images of protein surfaces. *Biophys. J.* **1999,** *77*, 1150-1158.

110. Ohnishi, S.; Hara, M.; Furuno, T.; Okada, T.; Sasabe, H. Direct visualization of polypeptide shell of ferritin molecule by atomic-force microscopy. *Biophys. J.* **1993,** *65*, 573-577.

111. Ohnishi, S.; Hara, M.; Furuno, T.; Sasabe, H. Imaging the ordered arrays of water-soluble protein ferritin with the atomic force microscope. *Biophys. J.* **1992,** *63*, 1425-1431.

112. Caruso, F.; Furlong, D. N.; Kingshott, P. Characterization of ferritin adsorption onto gold. *J. Colloid Interf. Sci.* **1997,** *186*, 129-140.

113. Allen, S.; Davies, J.; Davies, M. C.; Dawkes, A. C.; Roberts, C. J.; Tendler, S. J. B.; Williams, P. M. The influence of epitope availability on atomic-force microscope studies of antigen–antibody interactions. *Biochem. J.* **1999,** *341*, 173-178.

114. Johnson, C. A.; Yuan, Y.; Lenhoff, A. M. Adsorbed layers of ferritin at solid and fluid interfaces studied by atomic force microscopy. *J. Colloid Interf. Sci.* **2000,** *223*, 261-272.

115. Mollica, V.; Relini, A.; Rolandi, R.; Bolognesi, M.; Gliozzi, A. Force probing of protein crystals: An atomic force microscopy study. *Eur. Phys. J. E* **2000,** *3*, 315-321.

116. Tominaga, M.; Ohira, A.; Yamaguchi, Y.; Kunitake, M. Electrochemical, AFM and QCM studies on ferritin immobilized onto a self-assembled monolayer-modified gold electrode. *J. Electroanal. Chem.* **2004,** *566*, 323-329.

117. Du, X. Z.; Hlady, V.; Britt, D. Langmuir monolayer approaches to protein recognition through molecular imprinting. *Biosens. Bioelectron.* **2005,** *20*, 2053-2060.

118. Xu, D. G.; Watt, G. D.; Harb, J. N.; Davis, R. C. Electrical conductivity of ferritin proteins by conductive AFM. *Nano Lett.* **2005,** *5*, 571-577.

119. Tominaga, M.; Soejima, K.; Matsumoto, M.; Taniguchi, I. Electrostatic modification of ferritin onto polypeptide-functionalized indium oxide electrode surfaces: Electrochemical and AFM studies. *J. Electroanal. Chem.* **2005,** *579*, 51-58.

120. Axford, D. N.; Davis, J. J. Electron flux through apo- and holoferritin. *Nanotechnology* **2007,** *18*.

121. Tominaga, M.; Miyahara, K.; Soejima, K.; Nomura, S.; Matsumoto, M.; Taniguchi, I. Size-tuneable and micro-patterned iron nanoparticles derived from biomolecules via microcontact printing SAM-modified substrates and controlled-potential electrolyses. *J. Colloid Interface Sci* **2007,** *313*, 135-140.

122. Schon, P.; Gorlich, M.; Coenen, M. J. J.; Heus, H. A.; Speller, S. Nonspecific protein adsorption at the single molecule level studied by atomic force microscopy. *Langmuir* **2007,** *23*, 9921-9923.

123. Hemmersam, A. G.; Rechendorff, K.; Besenbacher, F.; Kasemo, B.; Sutherland, D. S. pH-dependent adsorption and conformational change of ferritin studied on metal oxide surfaces by a combination of QCM-D and AFM. *J. Phys. Chem. C* **2008,** *112*, 4180-4186.

124. Domınguez-Vera, J. M.; Welte, L.; Galvez, N.; Fernandez, B.; Gomez-Herrero, J.; Zamora, F. Covalent deposition of ferritin nanoparticles onto gold surfaces. *Nanotechnology* **2008,** *19*, 025302.

125. Park, C. W.; Park, H. J.; Kim, J. H.; Won, K.; Yoon, H. H. Immobilization and characterization of ferritin on gold electrode. *Ultramicroscopy* **2009,** *109*, 1001-1005.

126. Won, K.; Park, M. J.; Yoon, H. H.; Kim, J. H. Immobilization of iron storage protein on a gold electrode based on self-assembled monolayers. *Ultramicroscopy* **2008,** *108*, 1342-1347.

127. Zhang, J. H.; Cui, C. Y.; Zhou, X. F. Study on elastic modulus of individual ferritin. *Chin. Sci. Bull.* **2009,** *54*, 723-726.

128. Rakshit, T.; Banerjee, S.; Mukhopadhyay, R. Near-metallic behavior of warm holoferritin molecules on a gold(111) surface. *Langmuir* **2010,** *26*, 16005-16012.

129. Yoshinobu, T.; Suzuki, J.; Kurooka, H.; Moon, W. C.; Iwasaki, H. AFM fabrication of oxide patterns and immobilization of biomolecules on Si surface. *Electrochim. Acta* **2003,** *48*, 3131-3135.

130. Agheli, H.; Malmstrom, J.; Hanarp, P.; Sutherland, D. S. Nanostructured biointerfaces. *Mat. Sci. Eng. C-Bio. S* **2006,** *26*, 911-917.

131. Agheli, H.; Malmstrom, J.; Larsson, E. M.; Textor, M.; Sutherland, D. S. Large area protein nanopatterning for biological applications. *Nano Lett.* **2006,** *6*, 1165-1171.

132. Yamashita, I.; Kirimura, H.; Okuda, M.; Nishio, K.; Sano, K.-I.; Shiba, K.; Hayashi, T.; Hara, M.; Mishima, Y. Selective nanoscale positioning of ferritin and nanoparticles by means of target-specific peptides**. *Small* **2006,** *2*, 1148-1152.

133. Kumagai, S.; Yoshii, S.; Yamada, K.; Matsukawa, N.; Fujiwara, I.; Iwahori, K.; Yamashita Electrostatic placement of single ferritin molecules. *Appl. Phys. Lett.* **2006,** *88*, 153103.

134. Daniels, S. L.; Ngunjiri, J. N.; Garno, J. C. Investigation of the magnetic properties of ferritin by AFM imaging with magnetic sample modulation. *Anal. Bioanal. Chem.* **2009,** *394*, 215-223.

135. Yoshii, S.; Kumagai, S.; Nishio, K.; Kadotani, A.; Yamashita, I. Electrostatic self-aligned placement of single nanodots by protein supramolecules. *Appl. Phys. Lett.* **2009,** *95*, 133702.

136. Bellido, E.; de Miguel, R.; Ruiz-Molina, D.; Lostao, A.; Maspoch, D. Controlling the number of proteins with dip-pen nanolithography. *Adv. Mater.* **2010,** *22*, 352-355.

137. Bellido, E.; Miguel, R. D.; Sese, J.; Ruiz-Molina, D.; Lostao, A.; Maspoch, D. Nanoscale positioning of inorganic nanoparticles using biological ferritin arrays fabricated by dip-pen nanolithography. *Scanning* **2010,** *32*, 35-41.

138. Martinez, R. V.; Martinez, J.; Chiesa, M.; Garcia, R.; Coronado, E.; Pinilla-Cienfuegos, E.; Tatay, S. Large-scale nanopatterning of single proteins used as carriers of magnetic nanoparticles. *Adv. Mater.* **2010,** *22*, 588-591.

139. Hu, Y. X.; Chen, D. A.; Park, S.; Emrick, T.; Russell, T. P. Guided assemblies of ferritin nanocages: Highly ordered arrays of monodisperse nanoscopic elements. *Adv. Mater.* **2010,** *22*, 2583-2587.

140. Yamamoto, S.-I.; Okada, T.; Uraoka, Y.; Yamashita, I.; Hasegawa, S. Static and dynamic observation of supermolecular protein, ferritin, using high-speed atomic force microscope. *J. Appl. Phys.* **2011,** *109*, 034901.

141. Allen, S.; Chen, X.; Davies, J.; Davies, M. C.; Dawkes, A. C.; Edwards, J. C.; Roberts, C. J.; Tendler, S. J. B.; Williams, P. M. The application of force microscopy to immunodiagnostic systems imaging and biomolecular adhesion measurements. *Appl. Phys. A* **1998,** *66*, S255-S261.

142. Allen, S.; Chen, X. Y.; Davies, J.; Davies, M. C.; Dawkes, A. C.; Edwards, J. C.; Roberts, C. J.; Sefton, J.; Tendler, S. J. B.; Williams, P. M. Detection of antigen-antibody binding events with the atomic force microscope. *Biochemistry* **1997,** *36*, 7457-7463.

143. Wakayama, J.; Sekiguchi, H.; Akanuma, S.; Ohtani, T.; Sugiyama, S. Methods for reducing nonspecific interaction in antibody-antigen assay via atomic force microscopy. *Anal. Biochem.* **2008,** *380*, 51-58.

144. Mollica, V.; Relini, A.; Rolandi, R.; Bolognesi, M.; Gliozzi, A. Force probing of protein crystals: An atomic force microscopy study. *Eur. Phys. J. E* **2000,** *3*, 315-321.

145. Harada, Y.; Kuroda, M.; Ishida, A. Specific and quantized antigen-antibody interaction measured by atomic force microscopy. *Langmuir* **2000,** *16*, 708-715.

146. Schreiber, S.; Savla, M.; Pelekhov, D. V.; Iscru, D. F.; Selcu, C.; Hammel, P. C.; Agarwal, G. Magnetic force microscopy of superparamagnetic nanoparticles. *Small* **2008,** *4*, 270-278.

147. Hsieh, C. W.; Zheng, B.; Hsieh, S. Ferritin protein imaging and detection by magnetic force microscopy. *Chem. Commun.* **2010,** *46*, 1655-1657.

148. Meldrum, F. C.; Wade, V. J.; Nimmo, D. L.; Heywood, B. R.; Mann, S. Synthesis of inorganic nanophase materials in supramolecular protein cages. *Nature* **1991,** *349*, 684-687.

149. Galvez, N.; Sanchez, P.; Domınguez-Vera, J. M. Preparation of Cu and CuFe prussian blue derivative nanoparticles using the apoferritin cavity as nanoreactor. *Dalton Trans.* **2005,** *15*, 2492-2494.

150. Domınguez-Vera J M; Galvez N; Sanchez P; Mota A J; Trasobares S; C, H. J.; J, C. J. Size-controlled water-soluble Ag nanoparticles. *Eur. J. Inorg. Chem.* **2007**, 4823-4826.

151. Galvez, N.; Fernandez, B.; Valero, E.; Sanchez, P.; Cuesta, R.; Domınguez-Vera, J. M. Apoferritin as a nanoreactor for preparing metallic nanoparticles. *C. R. Chim.* **2008,** *11*, 1207-1212.

152. Galvez, N.; Sanchez, P.; Domınguez-Vera, J. M.; A., S.-P.; Clemente-Leon, M.; Coronado, E. Apoferritin-encapsulated Ni and Co superparamagnetic nanoparticles. *J. Mater. Chem.* **2006,** *16*, 2757-2761.

153. Douglas, T.; Stark, V. T. Nanophase cobalt oxyhydroxide mineral synthesized within the protein cage of ferritin. *Inorg. Chem.* **2000,** *39*, 1828-1830.

154. Clemente-Leon, M.; Coronado, E.; Soriano-Portillo, A.; Galvez, N.; Dominguez-Vera, J. M. Permanent magnetism in apoferritin-encapsulated Pd nanoparticles. *J. Mater. Chem.* **2007,** *17*, 49-51.

155. Ueno, T.; Suzuki, M.; Goto, T.; Matsumoto, T.; Nagayama, K.; Watanabe, Y. Size-selective olefin hydrogenation by a Pd nanocluster provided in an apo-ferritin cage. *Angew. Chem. Int. Ed.* **2004,** *43*, 2527-2530.

156. Kim, J. W.; Choi, S. H.; Lillehei, P. T.; Chu, S. H.; King, G. C.; Watt, G. D. Electrochemically controlled reconstitution of immobilized ferritins for bioelectronic applications. *J. Electroanal. Chem.* **2007,** *601*, 8-16.

157. Tsukamoto, R.; Muraoka, M.; Fukushige, Y.; Nakagawa, H.; Kawaguchi, T.; Nakatsuji, Y.; Yamashita, I. Improvement Of Co_3O_4 nanoparticle synthesis in apoferritin cavity by outer surface PEGylation. *Bull. Chem. Soc. Japan* **2008,** *81*, 1669-1674.

158. Mann, S.; Meldrum, F. C. Controlled synthesis of inorganic materials using supramolecular assemblies. *Adv. Mater.* **1991,** *3*, 316-318.

159. Wong, K. K. W.; Mann, S. Biomimetic synthesis of cadmium sulfide-ferritin nanocomposites *Adv. Mater.* **1996,** *8*, 928.

160. Iwahori, K.; Yamashita, I. Size-controlled one-pot synthesis of fluorescent cadmium sulfide semiconductor nanoparticles in an apoferritin cavity. *Nanotechnology* **2008,** *19*, 495601.

161. Yamashita, I.; Hayashi, J.; Hara, M. Bio-template synthesis of uniform CdSe nanoparticles using cage-shaped protein, apoferritin. *Chem. Lett.* **2004,** *33*, 1158-1159.

162. Iwahori, K.; Yoshizawa, K.; Muraoka, M.; Yamashita, I. Fabrication of ZnSe nanoparticles in the apoferritin cavity by designing a slow chemical reaction system. *Inorg. Chem.* **2005,** *44*, 6393-6400.

163. Warne, B.; Kasyutich, O. I.; Mayes, E. L.; Wiggins, J. A. L.; Wong, K. K. W. Self assembled nanoparticulate Co : Pt for data storage applications. *IEEE Trans. Magn.* **2000,** *36*, 3009-3001.

164. Okuda, M.; Iwahori, K.; Yamashita, I.; Yoshimura, H. Fabrication of nickel and chromium nanoparticles using the protein cage of apoferritin. *Biotechnol. Bioeng.* **2003,** *84*, 187-194.

165. Iwahori, K.; Yoshizawa, K.; Muraoka, M.; Yamashita, I. Fabrication of ZnSe nanoparticles in the apoferritin cavity by designing a slow chemical reaction system. *Inorg. Chem.* **2005,** *44*, 6393-6400.

166. Wang, T.; Choi, H. W.; Yoo, I. S.; Kim, J. S.; Park, S. J. Preparation of two-dimensional array of nanodots by ferritin template. *Mol. Cryst. Liq. Cryst.* **2009,** *505*, 386-395.

167. Kramer, R. M.; Sowards, L. A.; Pender, M. J.; Stone, M. O.; Naik, R. R. Constrained iron catalysts for single-walled carbon nanotube growth. *Langmuir* **2005,** *21*, 8466-8470.

168. Kim, W.; Choi, H. C.; Shim, M.; Li, Y. M.; Wang, D. W.; Dai, H. J. Synthesis of ultralong and high percentage of semiconducting single-walled carbon nanotubes. *Nano Lett.* **2002,** *2*, 703-708.

169. Li, Y. M.; Kim, W.; Zhang, Y. G.; Rolandi, M.; Wang, D. W.; Dai, H. J. Growth of single-walled carbon nanotubes from discrete catalytic nanoparticles of various sizes. *J. Phys. Chem. B* **2001,** *105*, 11424-11431.

170. Durrer, L.; Helbling, T.; Zenger, C.; Jungen, A.; Stampfer, C.; Hierold, C. SWNT growth by CVD on ferritin-based iron catalyst nanoparticles towards CNT sensors. *Sens. Actuators, B* **2008,** *132*, 485-490.

171. Durrer, L.; Greenwald, J.; Helbling, T.; Muoth, M.; Riek, R.; Hierold, C. Narrowing SWNT diameter distribution using size-separated ferritin-based Fe catalysts. *Nanotechnology* **2009,** *20*, 355601.

172. Takagi, D.; Yamazaki, A.; Otsuka, Y.; Yoshimura, H.; Kobayashi, Y.; Homma, Y. Gold-filled apo-ferritin for investigation of single-walled carbon nanotube growth on substrate. *Chem. Phys. Lett.* **2007,** *445*, 213-216.

173. Yuan, Z.; Petsev, D. N.; Prevo, B. G.; Velev, O. D.; Atanassov, P. Two-Dimensional Nanoparticle Arrays Derived from Ferritin Monolayers. *Langmuir* **2007,** *23*, 5498-5504.

174. Yamashita, I. Fabrication of a two-dimensional array of nano-particles using ferritin molecule. *Thin Solid Films* **2001,** *393*, 12-18.

175. Yamashita, I.; Iwahori, K.; Kumagai, S. Ferritin in the field of nanodevices. *Biochim. Biophys. Acta* **2010,** *1800*, 846-857.

176. Hikono, T.; Uraoka, Y.; Fuyuki, T.; Yoshii, S.; Yamashita, I.; Takeguchi, M. Reduction of core in cage protein for application to electron device. *Surf. Sci.* **2006,** *600*, 2817-2822.

177. Miura, A.; Uraoka, Y.; Fuyuki, T.; Yoshii, S.; Yamashita, I. Floating nanodot gate memory fabrication with biomineralized nanodot as charge storage node. *J. Appl. Phys.* **2008,** *103*, 074503.

178. Miura, A.; Tsukamoto, R.; Yoshii, S.; Yamashita, I.; Uraoka, Y.; Fuyuki, T. Non-volatile flash memory with discrete bionanodot floating gate assembled by protein template. *Nanotechnology* **2008,** *19*, 255201.

179. Ohara, K.; Yamashita, I.; Yaegashi, T.; Moniwa, M.; Yoshimaru, M.; Uraoka, Y. Floating gate memory with biomineralized nanodots embedded in high-k gate dielectric. *Appl. Phys. Express* **2009,** *2*, 095001.

180. Banyard, S. H.; Stammers, D. K.; Harrison, P. M. Electron-density map of apoferritin at 2.8 Å resolution. *Nature* **1978,** *271*, 282-284.

181. Bi, X.; Chasteen, N. D. Iron oxidation chemistry in ferritin -increasing Fe/O_2 stoichiometry during core formation. *J. Biol. Chem.* **1991,** *266*, 19965-19970.

182. Ford, G. C.; Harrison, P. M.; Rice, D. W.; Smith, J. M. A.; Treffry, A.; White, J. L.; Yariv, J. Ferritin-design and formation of an iron-storage molecule. *Philos. Trans. R. Soc. London, Ser. B* **1984,** *304*, 551-&.

183. Gossuin, Y.; Roch, A.; Lo Bue, F.; Muller, R. N.; Gillis, P. Nuclear magnetic relaxation dispersion of ferritin and ferritin-like magnetic particle solutions: A pH-effect study. *Magn. Reson. Med.* **2001,** *46*, 476-481.

184. Gossuin, Y.; Roch, A.; Muller, R. N.; Gillis, P. Relaxation induced by ferritin and ferritin-like magnetic particles: The role of proton exchange. *Magn. Reson. Med.* **2000,** *43*, 237-243.

185. Bouaidat, S.; Berendsen, C.; Thomsen, P.; Petersen, S. G.; Wolff, A.; Jonsmann, J. Micro patterning of cell and protein non-adhesive plasma polymerized coatings for biochip applications. *Lab Chip* **2004,** *4*, 632-637.

186. Veiseh, M.; Zareie, M. H.; Zhang, M. Q. Highly selective protein patterning on gold-silicon substrates for biosensor applications. *Langmuir* **2002,** *18*, 6671-6678.

187. Shin, D. S.; Lee, K. N.; Janga, K. H.; Kim, J. K.; Chung, W. J.; Kim, Y. K.; Lee, Y. S. Protein patterning by maskless photolithography on hydrophilic polymer-grafted surface. *Biosens. Bioelectron.* **2003,** *19*, 485-494.

188. Lee, K. N.; Shin, D. S.; Lee, Y. S.; Kim, Y. K. Micromirror array for protein micro array fabrication. *J. Micromech. Microeng.* **2003,** *13*, 474-481.

189. Hook, A. L.; Voelcker, N. H.; Thissen, H. Patterned and switchable surfaces for biomolecular manipulation. *Acta Biomater.* **2009,** *5*, 2350-2370.

190. Hill, R. T.; Lyon, J. L.; Allen, R.; Stevenson, K. J.; Shear, J. B. Microfabrication of three-dimensional bioelectronic architectures. *J. Am. Chem. Soc.* **2005,** *127*, 10707-10711.

191. Kim, E.; Xia, Y. N.; Whitesides, G. M. Polymer microstructures formed by molding in capillaries. *Nature* **1995,** *376*, 581-584.

192. Kim, E.; Xia, Y. N.; Whitesides, G. M. Micromolding in capillaries: Applications in materials science. *J. Am. Chem. Soc.* **1996,** *118*, 5722-5731.

193. Delamarche, E.; Bernard, A.; Schmid, H.; Michel, B.; Biebuyck, H. Patterned delivery of i mmunoglobulins to surfaces using microfluidic networks. *Science* **1997,** *276*, 779-781.

194. Tan, W.; Desai, T. A. Microfluidic patterning of cells in extracellular matrix biopolymers: Effects of channel size, cell type, and matrix composition on pattern integrity. *Tissue Eng.* **2003,** *9*, 255-267.

195. Kane, R. S.; Takayama, S.; Ostuni, E.; Ingber, D. E.; Whitesides, G. M. Patterning proteins and cells using soft lithography. *Biomaterials* **1999,** *20*, 2363-2376.

196. Khademhosseini, A.; Eng, G.; Yeh, J.; Kucharczyk, P. A.; Langer, R.; Vunjak-Novakovic, G.; Radisic, M. Microfluidic patterning for fabrication of contractile cardiac organoids. *Biomed. Microdevices* **2007,** *9*, 149-157.

197. Douglass, D. C.; Cox, A. J.; Bucher, J. P.; Bloomfield, L. A. Magnetic-properties of free cobalt and gadolinium clusters. *Phys. Rev. B* **1993,** *47*, 12874-12889.

198. Bonnemain, B. Superparamagnetic agents in magnetic resonance imaging: Physicochemical characteristics and clinical applications - A review *J. Drug Targeting* **1998,** *6*, 167-174.

199. Berry, C. C.; Curtis, A. S. G. Functionalisation of magnetic nanoparticles for applications in biomedicine. *J. Phys. D: Appl. Phys.* **2003,** *36*, R198-R206.

200. Bulte, J. W. M.; Brooks, R. A. *Scientific and Clinical Applications of Magnetic Carriers*. Plenum Press: New York, 1997.

201. Jurado, R. L. Iron, infections, and anemia of inflammation. *Clin. Infect. Dis.* **1997,** *25*, 888-895.

202. Barton, J. C.; McDonnell, S. M.; Adams, P. C.; Brissot, P.; Powell, L. W.; Edwards, C. Q.; Cook, J. D.; Kowdley, K. V. Management of hemochromatosis. *Ann. Internal Med.* **1998,** *129*, 932-939.

203. Mendler, M.; Turlin, B.; Moirand, R.; Jouanolle, A. M.; Sapey, T.; Guyader, D.; LeGall, J. Y.; Brissot, P.; David, V.; Deugnier, Y. Insulin resistance-associated hepatic iron overload. *Gastroenterology* **1999,** *117*, 1155-1163.

204. Bentley, D. P.; Williams, P. Serum ferritin concentration as an index of storage iron in rheumatoid-arthritis. *J. Clin. Pathol.* **1974,** *27*, 786-788.

205. Cogswell, M. E.; McDonnell, S. M.; Khoury, M. J.; Franks, A. L.; Burke, W.; Brittenham, G. Iron overload, public health, and genetics: Evaluating the evidence for hemochromatosis screening. *Ann. Internal Med.* **1998,** *129*, 971-979.

206. Kalantarzadeh, K.; Hoffken, B.; Wunsch, H.; Fink, H.; Kleiner, M.; Luft, F. C. Diagnosis of iron-deficiency anemia in renal-failure patients during the post-erythropoietin era. *Am. J. Kidney Diseases* **1995,** *27*, 292-299.

207. Adams, P. C.; Deugnier, Y.; Moirand, R.; Brissot, P. The relationship between iron overload, clinical symptoms, and age in 410 patients with genetic hemochromatosis. *Hepatology* **1997,** *25*, 162-166.

208. Ngunjiri, J. N.; Daniels, S. L.; Li, J.-R.; Serem, W. K.; Garno, J. C. Controlling the arrangement of proteins on surfaces using particle lithography. *Nanomedicine* **2008,** *3*, 529-541.

209. Li, J.-R.; Henry, G. C.; Garno, J. C. Fabrication of nanopatterned films of bovine serum albumin and staphylococcal protein A using latex particle lithography. *Analyst* **2006,** *131*, 244-250.

210. Tessier, P.; Velev, O. D.; Kalambur, A. T.; Lenhoff, A. M.; Rabolt, J. F.; Kaler, E. W. Structured metallic films for optical and spectroscopic applications via colloidal crystal templating. *Adv. Mater.* **2001,** *13*, 396-400.

211. Jiang, P.; Bertone, J. F.; Colvin, V. L. A lost-wax approach to monodisperse colloids and their crystals. *Science* **2001,** *291*, 453-457.

212. Li, J.-R.; Garno, J. C. Elucidating the role of hydrosilation for nanopatterning organosilanes via particle lithography. *Nano Lett.* **2008,** *8*, 1916-1922.

213. McLellan, J. M.; Geissler, M.; Xia, Y. N. Edge spreading lithography and its application to the fabrication of mesoscopic gold and silver rings. *J. Am. Chem. Soc.* **2004,** *126*, 10830-10831.

214. Briseno, A. L.; Han, S. B.; Rauda, I. E.; Zhou, F. M.; Toh, C. S.; Nemanick, E. J.; Lewis, N. S. Electrochemical polymerization of aniline monomers infiltrated into well-ordered truncated eggshell structures of polyelectrolyte multilayers. *Langmuir* **2004,** *20*, 219-226.

215. Marquez, M.; Patel, K.; Carswell, A. D. W.; Schmidtke, D. W.; Grady, B. P. Synthesis of nanometer-scale polymeric structures on surfaces from template assisted admicellar polymerization: A comparative study with protein adsorption. *Langmuir* **2006,** *22,* 8010-8016.

216. Choi, D.-G.; Jang, S. G.; Yu, H. K.; Yang, S.-M. Two-dimensional polymer nanopattern by using particle-assisted soft lithography. *Chem. Mater.* **2004,** *16,* 3410-3413.

217. Garno, J. C.; Amro, N. A.; Wadu-Mesthrige, K.; Liu, G. Y. Production of periodic arrays of protein nanostructures using particle lithography. *Langmuir* **2002,** *18,* 8186-8192.

218. Cai, Y.; Ocko, B. M. Large-scale fabrication of protein nanoarrays based on nanosphere lithography. *Langmuir* **2005,** *21*, 9274-9279.

219. Blawas, A. S.; Reichert, W. M. Protein Patterning. *Biomaterials* **1998,** *19*, 595-609.

220. Scouten, W. H.; Luong, J. H.; Brown, R. S. Enzyme or protein immobilization techniques for applications in biosenor design. *Trends. Biotechnol.* **1995,** *13*, 178-185.

221. Zhang, S.; Yan, L.; Altman, M.; Lassle, M.; Nugent, H.; Frankel, F.; Lauffenburger, D. A.; Whitesides, G. M.; Rich, A. Biological surface engineering: A simple system for cell pattern formation. *Biomaterials* **1999,** *20,* 1213-1220.

222. Ravenscroft, M. S.; Bateman, K. E.; Shaffer, K. M.; Schessler, H. M.; Jung, D. R.; Schneider, T. W.; Montgomery, C. B.; Custer, T. L.; Schaffner, A. E.; Liu, Q. Y.; Li, Y. X.; Barker, J. L.; Hickman, J. J. Developmental neurobiology implications from fabrication and analysis of hippocampal neuronal networks on patterned silane-modified surfaces. *J. Am. Chem. Soc.* **1998,** *120*, 12169-12177.

223. Wilcox, D.; Dove, B.; McDavid, D.; Greer, D. *UTHSCSA Image Tool for Windows Version 3.00,* The University of Texas Health Science Center: San Antonio, TX, 1995-2002.

224. Trikha, J.; Waldo, G. S.; Lewandowski, F. A.; Ha, Y.; Theil, E. C.; Weber, P. C.; Allewell, N. M. Crystallization and structural-analysis of bullfrog red-cell L-subunit ferritins. *Proteins Struct. Funct. Genetics* **1994,** *18*, 107-118.

225. Porthun, S.; Abelmann, L.; Lodder, C. Magnetic force microscopy of thin film media for high density magnetic recording. *J. Magn. Magn. Mater.* **1998,** *182*, 238-273.

226. Hehn, M.; Padovani, S.; Ounadjela, K.; Bucher, J. P. Nanoscale magnetic domain structures in epitaxial cobalt films. *Phys. Rev. B* **1996,** *54*, 3428-3433.

227. Belliard, L.; Miltat, J.; Thiaville, A.; Dubois, S.; Duvail, J. L.; Piraux, L. Observing magnetic nanowires by means of magnetic force microscopy. *J. Magn. Magn. Mater.* **1998,** *190*, 1-16.

228. Qin, D. H.; Lu, M.; Li, H. L. Magnetic force microscopy of magnetic domain structure in highly ordered Co nanowire arrays. *Chem. Phys. Lett.* **2001,** *350,* 51-56.

229. Puntes, V. F.; Gorostiza, P.; Aruguete, D. M.; Bastus, N. G.; Alivisatos, A. P. Collective behaviour in two-dimensional cobalt nanoparticle assemblies observed by magnetic force microscopy. *Nature Mater.* **2004,** *3*, 263-268.

230. Zhang, Z.; Hammel, P. C.; Wigen, P. E. Observation of ferromagnetic resonance in a microscopic sample using magnetic resonance force microscopy. *App. Phys. Letts.* **1996,** *68*, 2005-2007.

231. Bausch, A. R.; Ziemann, F.; Boulbitch, A. A.; Jacobson, K.; Sackmann, E. Magnetic-resonance force microscopy. *Rev. Mod. Phys.* **1995,** *67*, 249-265.

232. Sidles, J. A.; Garbini, J. L.; Bruland, K. J.; Rugar, D.; Zuger, O.; Hoen, S.; Yannoni, C. S. Magnetic-resonance force microscopy. *Rev. Mod. Phys.* **1995,** *67*, 249-265.

233. Han, W. H.; Lindsay, S. M.; Jing, T. W. A magnetically driven oscillating probe microscope for operation in liquids. *App. Phys. Letts.* **1996,** *69*, 4111-4113.

234. Leuba, S. H.; Lindsay, S. M. Magnetically driven oscillating probe ("MAC mode") scanning force microscopy (SFM) of chromatin fibers in aqueous buffer. *Biophys. J.* **1998,** *74*, A71.

235. Kienberger, F.; Stroh, C.; Kada, G.; Moser, R.; Baumgartner, W.; Pastushenko, V.; Rankl, C.; Schmidt, U.; Muller, H.; Orlova, E.; LeGrimellec, C.; Drenckhahn, D.; Blaas, D.; Hinterdorfer, P. Dynamic force microscopy imaging of native membranes. *Ultramicroscopy* **2003,** *97*, 229-237.

236. Ge, G.; Han, D.; Lin, D.; Chu, W.; Sun, Y.; Jiang, L.; Ma, W.; Wang, C. MAC mode atomic force microscopy studies of living samples, ranging from cells to fresh tissue. *Ultramicroscopy* **2007,** *107*, 299-307.

237. Florin, E.-L.; Radmacher, M.; Fleck, B.; Gaub, H. E. Atomic force microscope with magnetic force modulation. *Rev. Sci. Instrum.* **1994,** *65*, 639-643.

238. Shi, B. Y.; Xiao, W. Z.; Taylor, J. S. Influences of water treatment process on iron and copper release in distribution system. *J. Environ. Sci. Health, Part A: Toxic/Hazard. Subst. Environ. Eng.* **2006,** *41*, 1667-1683.

239. Dietrich, A. M.; Glindemann, D.; Pizarro, F.; Gidi, V.; Olivares, M.; Araya, M.; Camper, A.; Duncan, S.; Dwyer, S.; Whelton, A. J.; Younos, T.; Subramanian, S.; Burlingame, G. A.; Khiari, D.; Edwards, M. Health and aesthetic impacts of copper corrosion on drinking water. *Water Sci. Technol.* **2004,** *49*, 55-62.

240. Hong, P. K. A.; MacAuley, Y. Y. Corrosion and leaching of copper tubing exposed to chlorinated drinking water. *Water, Air, Soil Pollut.* **1998,** *108*, 457-471.

241. USEPA Lead and Copper Rule: A quick reference guide:. http://www.epa.gov/safewater/lcrmr/pdfs/qrg-lcmr.pdf

242. Ives, D. J. G.; Rawson, A. E. Copper corrosion .4. The effect of saline additions *J. Electrochem. Soc.* **1962,** *109*, 462-466.

243. Xiao, W.; Hong, S.; Tang, Z.; Seal, S.; Taylor, J. S. Effects of blending on surface characteristics of copper corrosion products in drinking water distribution systems. *Corros. Sci.* **2006,** *49*, 449-468.

244. Cong, H. B.; Michels, H. T.; Scully, J. R. Passivity and pit stability behavior of copper as a function of selected water chemistry variables. *J. Electrochem. Soc.* **2009,** *156*, C16-C27.

245. Hayon, J.; Yarnitzky, C.; Yahalom, J.; Bettelheim, A. Surface processes characterization for the corrosion of copper in borate solutions - I. The effect of sodium dodecylsulfate. *J. Electrochem. Soc.* **2002,** *149*, B314-B320.

246. Vargas, I. T.; Alsina, M. A.; Pastén, P. A.; Pizarro, G. E. Influence of solid corrosion by-products on the consumption of dissolved oxygen in copper pipes. *Corros. Sci.* **2009,** *51*, 1030-1037.

247. Merkel, T. H.; Pehkonen, S. O. General corrosion of copper in domestic drinking water installations: scientific background and mechanistic understanding. *Corros. Eng. Sci.Technol.* **2006,** *41*, 21-37.

248. Schock, M. R.; Sandvig, A. M. Long-term effects of orthophosphate treatment on copper concentration. *J. Am. Water Works Assoc.* **2009,** *101*, 71.

249. Shi, B. Y.; Taylor, J. S. Iron and copper release in drinking-water distribution systems. *J. Environ. Health* **2007,** *70*, 29-36.

250. Lewandowski, B. R.; Lytle, D. A.; Garno, J. C. Nanoscale investigation of the impact of pH and orthophosphate on the corrosion of copper curfaces in water. *Langmuir* **2010,** *26*, 14671-14679.

251. Souissi, N.; Triki, E. Modelling of phosphate inhibition of copper corrosion in aqueous chloride and sulphate media. *Corros. Sci.* **2008,** *50*, 231-241.

252. Goh, K. H.; Lim, T. T.; Chui, P. C. Evaluation of the effect of dosage, pH and contact time on high-dose phosphate inhibition for copper corrosion control using response surface methodology (RSM). *Corros. Sci.* **2008,** *50*, 918-927.

253. Dartmann, J.; Sadlowsky, B.; Dorsch, T.; Johannsen, K. Copper corrosion in drinking water systems - effect of pH and phosphate-dosage. *Mater. Corros.* **2010,** *61*, 189-198.

254. Dartmann, J.; Alex, T.; Dorsch, T.; Schevalje, E.; Johannsen, K. Influence of decarbonisation and phosphate dosage on copper corrosion in drinking water systems. *Acta Hydroch. Hydrob.* **2004,** *32*, 25-32.

255. Becker, A. The effect of corrosion inhibitors in drinking water installations of copper. *Mater. Corros.* **2002,** *53*, 560-567.

256. Valcarce, M. B.; Vazquez, M. Phosphate ions used as green inhibitor against copper corrosion in tap water. *Corros. Sci. 52*, 1413-1420.

257. Bertrand, G.; Rocca, E.; Savall, C.; Rapin, C.; Labrune, J. C.; Steinmetz, P. In-situ electrochemical atomic force microscopy studies of aqueous corrosion and inhibition of copper. *J. Electroanal. Chem.* **2000,** *489*, 38-45.

258. Martin, F. A.; Bataillon, C.; Cousty, J. In situ AFM detection of pit onset location on a 304L stainless steel. *Corros. Sci.* **2008,** *50*, 84-92.

259. Li, J.; Lampner, D. In-situ AFM study of pitting corrosion of Cu thin films. *Colloids Surf., A* **1999,** *154*, 227-237.

260. Kleber, C.; Schreiner, M. In situ TM-AFM investigations of the influence of zinc and tin as alloy constituents of copper to the early stages of corrosion. *Appl. Surf. Sci.* **2003,** *217*, 294-301.

261. Lewandowski, B. R.; Lusker, K. L.; LeJeune, Z. M.; Lytle, D. A.; Zhou, P.; Sprunger, P. T.; Garno, J. C. Impact of pH, dissolved inorganic carbon, and polyphosphates for the initial stages of the water corrosion of copper surfaces investigated by AFM and NEXAFS. *Corros. Sci.* **2011**.

262. Jadashecart, A.; Elmorer, A.; Stitou, M.; Bouillot, P.; Legube, B. The chlorine demand of a treated water. *Water Res.* **1992,** *26*, 1073-1084.

263. Klapetek, P.; Necas, D. *Gwyddion*, Czech Metrology Institute: Czech Republic, 2007.

264. http://www.camd.lsu.edu/.

265. Kleber, C.; Rosner, M.; Hutter, H.; Schreiner, M. Influence of increasing zinc contents in brass in the early stages of corrosion investigated by in-situ TM-AFM and SIMS. *Anal. Bioanal. Chem.* **2002,** *374*, 338-343.

266. Wilcox, C. D.; Dove, S. B.; McDavid, W. D.; Greer, D. B. *UTHSCSA Image Tool http://ddsdx.uthscsa.edu/dig/download.html*, Department of Dental Diagnostic Science at The University of Texas Health Science Center: San Antonio, Texas, 2002.

267. Magonov, S. N.; Elings, V.; Whangbo, M. H. Phase imaging and stiffness in tapping-mode atomic force microscopy. *Surf. Sci.* **1997,** *375*, L385-L391.

268. Mayer, R. W.; Melzer, M.; Havecker, M.; Knop-Gericke, A.; Urban, J.; Freund, H. J.; Schlogl, R. Comparison of oxidized polycrystalline copper foil with small deposited copper clusters in their behavior in ammonia oxidation: an investigation by means of in situ NEXAFS spectroscopy in the soft X-ray range. *Catal. Lett.* **2003,** *86*, 245-250.

269. Nachimuthu, P.; Thevuthasan, S.; Kim, Y. J.; Lea, A. S.; Shutthanandan, V.; Engelhard, M. H.; Baer, D. R.; Chambers, S. A.; Shuh, D. K.; Lindle, D. W.; Gullikson, E. M.; Perera, R. C. C. Investigation of copper(I) oxide quantum dots by near-edge X-ray absorption fine structure spectroscopy. *Chem. Mater.* **2003,** *15*, 3939-3946.

270. Papadimitropoulos, G.; Vourdas, N.; Vamvakas, V. E.; Davazoglou, D. Optical and structural properties of copper oxide thin films grown by oxidation of metal layers. *Thin Solid Films* **2006,** *515*, 2428-2432.

271. Das, S. S.; Singh, N. P.; Srivastava, P. K. Ion conducting phosphate glassy materials. *Prog. Cryst. Growth Charact. Mater.* **2009,** *55*, 47-62.

272. Kim, J. W.; Posey, A. E.; Watt, G. D.; Choi, S. H.; Lillehei, P. T. Gold nanoshell assembly on a ferritin protein employed as a bio-template. *J. Nanosci. Nanotechnol.* **2010,** *10*, 1771-1777.

273. Deng, Q. Y.; Yang, B.; Wang, J. F.; Whiteley, C. G.; Wang, X. N. Biological synthesis of platinum nanoparticles with apoferritin. *Biotechnol. Lett.* **2009,** *31*, 1505-1509.

274. Cormode, D. P.; Jarzyna, P. A.; Mulder, W. J. M.; Fayad, Z. A. Modified natural nanoparticles as contrast agents for medical imaging. *Adv. Drug Delivery Rev.* **2010,** *62*, 329-338.

275. Zheng, B.; Yamashita, I.; Uenuma, M.; Iwahori, K.; Kobayashi, M.; Uraoka, Y. Site-directed delivery of ferritin-encapsulated gold nanoparticles. *Nanotechnology* **2010,** *21*.

276. Sakamoto, H.; Kuboi, T.; Nagakura, T.; Hayashi, S.; Hoshi, F.; Mutoh, K.; Watanabe, K.; Orino, K. Characterization of feline serum ferritin-binding proteins: the presence of a novel ferritin-binding protein as an inhibitory factor in feline ferritin immunoassay. *BioMetals* **2009,** *22*, 793-802.

277. Papaefthymiou, G. C. Nanoparticle magnetism. *Nano Today* **2009,** *4*, 438-447.

278. Porti, M.; Meli, S.; Nafria, M.; Aymerich, X. Pre-breakdown noise in electrically stressed thin SiO_2 layers of MOS devices observed with C-AFM. *Microelectron. Reliab.* **2003,** *43*, 1203-1209.

279. Park, J. Y.; Maier, S.; Hendriksen, B.; Salmeron, M. Sensing current and forces with SPM. *Mater. Today* **2010,** *13*, 37-44.

APPENDIX A: LABORATORY PROCEDURES FOR PREPARING COPPER SUBSTRATES IN CORROSION STUDIES

Cleaning Procedure for Copper Substrates

The procedure is based on the American Society of Testing and Materials (ASTM) standard for cleaning copper substrates, modified to suit AFM studies. The ASTM standard procedure suggests that substrates should be cleaned in 0.5% HCL for 30 min. However, AFM images disclosed that the acid-treated substrates altered the morphology of copper surfaces.

1. An unpolished pure copper alloy sheet (110 ASTM B187) from Metal Supermarket (Cincinnati, OH) should be cut into 0.75×0.75 in^2 square coupons. Punch a small hole in one corner of the square coupon.

   a. Pre-rinse the coupons with deionized water.

   b. Prepare a 0.05% dilute solution of Triton-X 100® with deionized water in a 500 mL container.

   c. Transfer 20 mL of the stock solution of Triton-X 100® detergent into a beaker containing the coupon. Sonicate for 5-10 minutes to remove oil and other contaminants from the coupon.

   d. Remove the coupons and rinse with deionized water

   e. Sonicate the coupons again for 5-10 minutes in deionized water.

   f. Rinse the coupons with acetone to remove any remaining organic contaminants and store dry coupons in a petri dish.

2. To prepare the designed test water, add 1000 ml deionized water (18 MΩ) to the reaction cell with a stirring paddle at medium speed.

3. Calibrate the pH meter with buffer solutions (pH 7 and 10). After calibration, place the electrodes in the reaction cell.

4. Adjust the test water to the targeted pH by adding 6N hydrochloric acid and/or sodium hydroxide from stock solution achieve the desired value. Allow the pH to stabilize before adding reagents.

5. Measure 10 mg of sodium bicarbonate ($NaHCO_3^-$) as dissolved inorganic carbon and add to the water. Adjust pH as needed.

6. While continuously stirring, add 120 mg/L of sulfate as sodium sulfate.

7. The chloride ion is added by weight as 60 mg of sodium chloride

8. Add 3 mL of chlorine as sodium hypochlorite acid to the solution.

9. When testing the inhibitor, add 6 mg of orthophosphate as sodium phosphate tribasic.

10. Continue to mix the water solution for 5-10 minutes.

11. Pour 600 ml of the finished water into a 800 ml beaker and place on a stirring plate with a stir bar. Mix slowly.

12. Suspend two clean coupons in the finished drinking water by threading with string.

Figure A.1 Photograph of the reaction cell set-up

13. Cover the reaction cell with parafilm with continuous mixing before removing the coupon after 6 or 24 hours.

14. After removing, dry each coupon in air and store in a desiccator as needed.

15. Take the remaining water, place in a 100 ml amber vial for total inorganic measurements. Add 100 ml to a clear vial to verify the concentrations of sulfate, chloride, chlorine and orthophosphate added to the water.

16. Measure the total free chlorine by taking 10 ml of the finished test water and adding N,N-diethyl-phenylenediamine (DPD) (which should turn deep pink) and analyze with a HACH colorimeter at a wavelength of 530 nm.

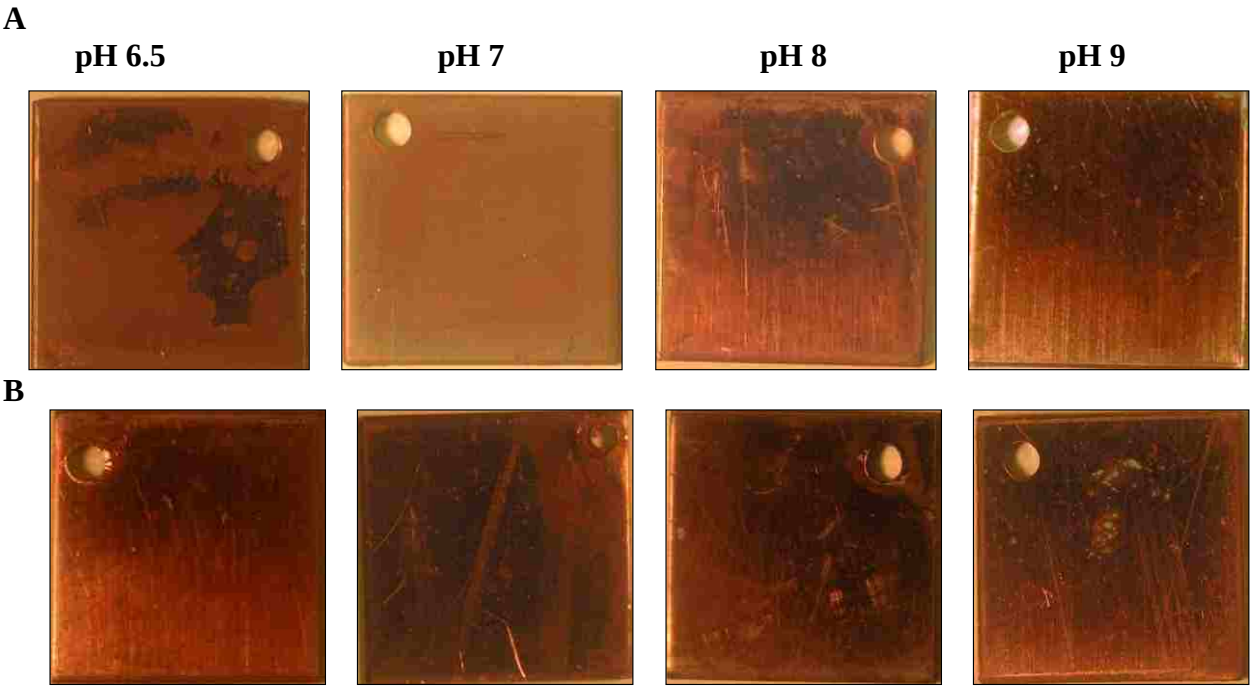

Figure A.2 Photographs of copper coupons after 24 h of immersion time in treated water at various pH. The pH is shown above the column for the two rows. [A] coupons in contact with waters without 6 mg/L of orthophosphate. [B] coupons immersed in test waters with 6 mg/L of orthophosphate.

APPENDIX B. SUPPLEMENTAL XRD SPECTRA FOR TREATED COPPER SAMPLES

Characterizations with x-ray diffraction (XRD) were obtained after 24 h of immersion of the copper coupons in treated water samples at pH 6.5, 7.0, 8.0 and 9.0. The Figures displayed in Appendix B show XRD spectra of coupons without orthophosphate (B.1) and coupons with orthophosphate (B.2).

A Scintag (Scintag, Inc., Santa Clara, CA) XDS-2000 theta theta diffractometer with a copper X-ray tube was used to identify crystalline phases of the deposits formed on the copper surface. The tube was operated at 30 keV and 40 mA for most analyses. Scans were typically performed over a 2-theta range between 5^{o} to 60^{o} with a step of 0.02^{o} with a three-second count time at each step. Pattern analysis was performed generally following ASTM procedures (ASTM 1996) using the computer software Jade (Versions 5-7, Materials Data, Inc.) with reference to the 1995-2002 ICDD PDF-2 data files (International Center for Diffraction Data, Newtown Square, PA). The XRD data was performed at the USEPA in Cincinnati, OH by Dr. Mallikarjuna (Malik) N. Nadagouda.

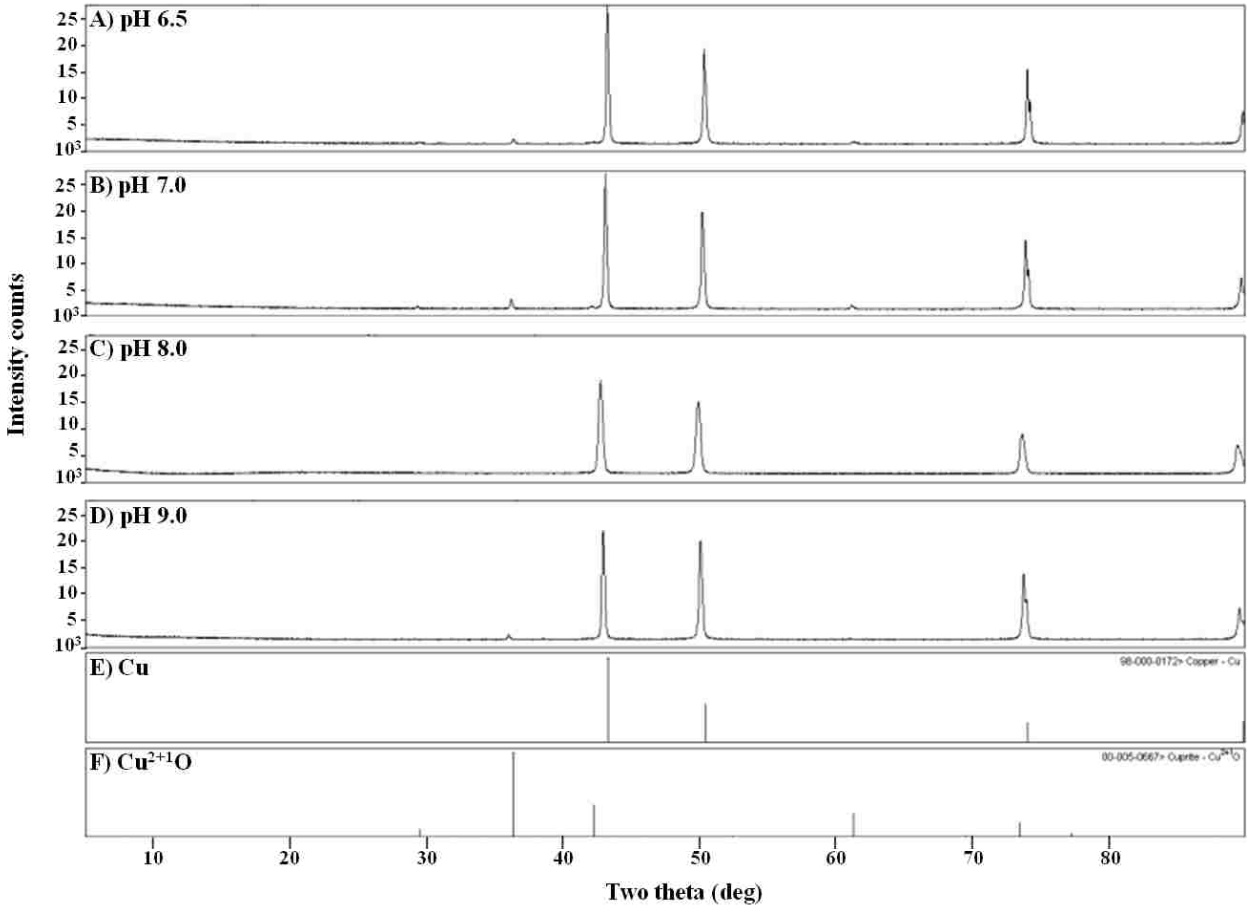

Figure B.1 Analysis of copper surfaces with XRD for samples immersed 24 h in treated water without orthophosphate. [A] pH 6.5; [B] pH 7.0; [C] pH 8.0 [D] pH 9.0; [E] Cu standard and [F] Cu^{2+1}

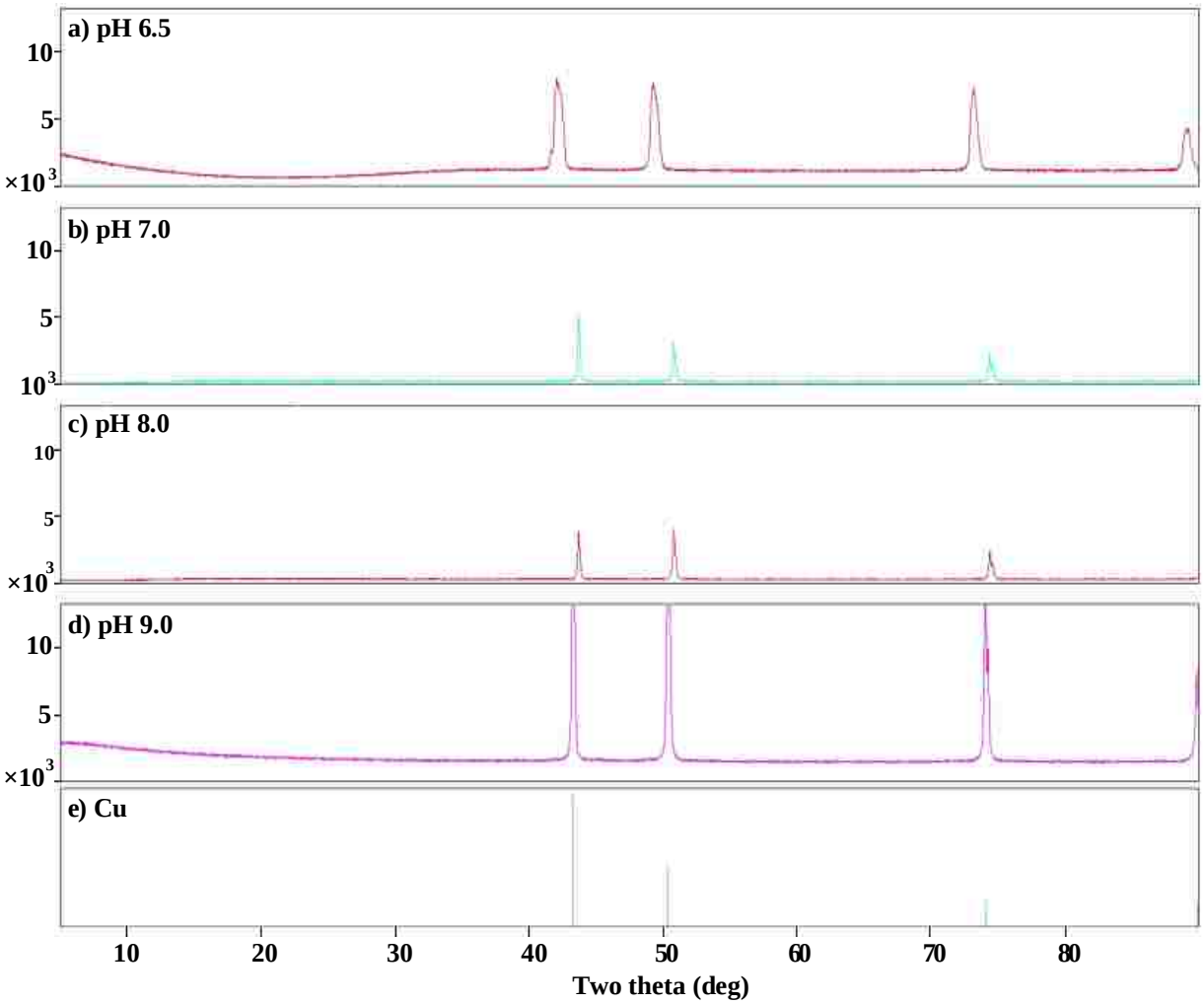

Figure B.2 Analysis of copper surfaces with XRD for substrates immersed for 24 h in treated water with 6 mg/L orthophosphate (PO_4^{3-}). [A] pH 6.5; [B] pH 7.0; [C] pH 8.0; [D] pH 9.0 and [E] Cu standard.

APPENDIX C. SCANNING ELECTRON MICROSCOPY (SEM) AND ENERGY DISPERSIVE X-RAY ANALYSIS (EDS)

Scanning electron microscopy was used as a complementary imaging technique to give a large area view of the changes in surface morphology. The SEM/EDS analyses of the copper coupons were performed at the USEPA with Dr. Mallikarjuna N. Nadagouda. Images with SEM were acquired for a copper substrate immersed 24 h in synthetic drinking water at pH 6.5 with 6 mg/L orthophosphate. The images were taken at two different locations to obtain results that would be representative of the surface. As apparent in the SEM image, there are clear variations in the formation of the copper by-products.

Nearly all scanning electron microscopy images and energy dispersive x-ray analyses were obtained using a JEOL 5300 scanning electron microscope (SEM) (Peabody, MA) with an attached Link Analytical energy dispersive x-ray analyzer (EDX) (Madison, WI). The copper coupons were mounted on 12-mm diameter aluminum studs with double-sided carbon tape. The accelerating voltage was 15 keV, and an average count time of 180 seconds was used to obtain EDX traces. The magnification used ranged from 100x to 3,000x, and EDX results were reported as weight % unless otherwise noted. Prior to elemental analysis, the EDX system was optimized, according to manufacturer's protocol, using an uncoated copper grid. The accuracy for reported elements is approximately 10% relative error, though matrix effects, elemental concentration, and peak overlaps can increase this error; therefore, EDX results should be interpreted accordingly.

A

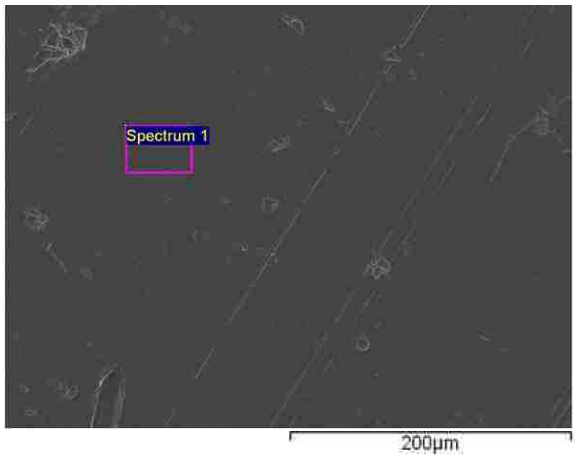

B

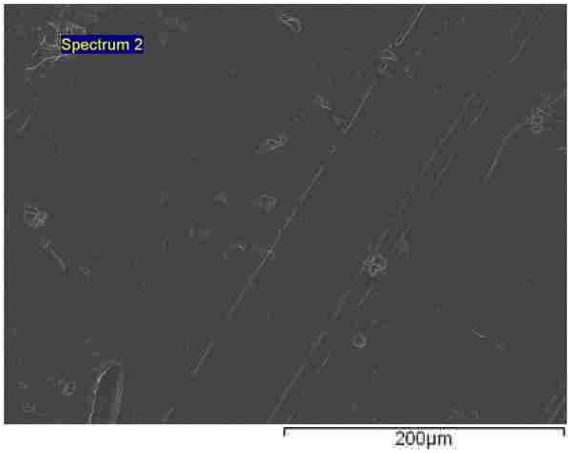

Table C.1 EDS data selected region 1

Element	Wt. %	At. %
Cu K	100	100
Total	100	

Table C.1.1 EDS data selected region 2

Element	Wt. %	At. %
Cu K	100	100
Total	100	

Figure C.1. SEM of a clean copper coupon. [A] 400 × 400 µm ^{2} view of an area of the surface; [B] 400 × 400 µm ^{2} view at a different location.

Table C.1 EDS data of the element composition corresponding to selected area **A.**

Table C.1.1 EDS data of the element composition corresponding to selected **B.**

A

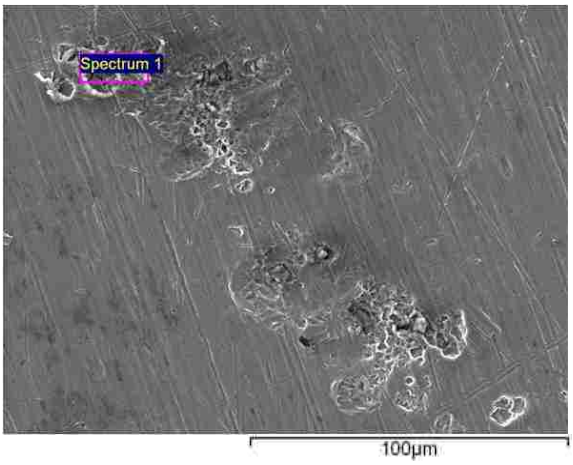

B

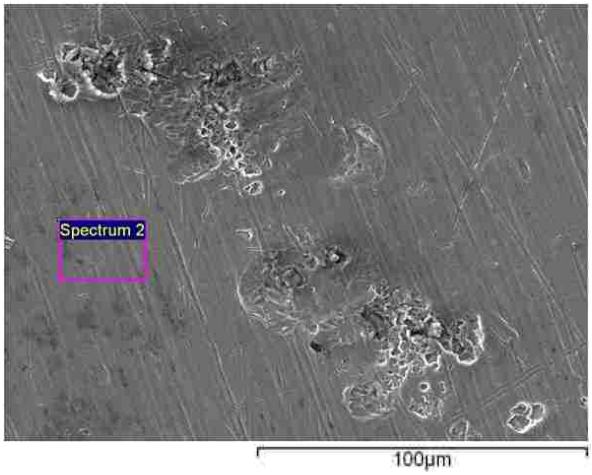

Table C.2 EDS data selected region 1

Element	Wt. %	At. %
Cu K	66.0	35.8
Cl K	0.68	0.67
Fe K	0.18	0.11
Si	3.48	4.27
P	4.38	4.88
Al	0.22	0.28
O K	25.0	53.9
Zr	0.24	0.16
Total	100	

Table C.2.1 EDS data of selected region 2

Element	Wt. %	At. %
Cu K	97.6	91.8
O K	2.14	8.00
Zr L	0.24	0.16
Total	100	

Figure C.2 SEM images of a copper substrate immersed for 24 h in synthetic drinking water at pH 6.5 with 6 mg/L orthophosphate.

Table C.2 Shows EDS data corresponding to image **A** of weight and atomic percent (%) of elements present.

Table C.2.1 Shows EDS data corresponding to image B elemental weight and atomic percent (%) within depicted area.

A

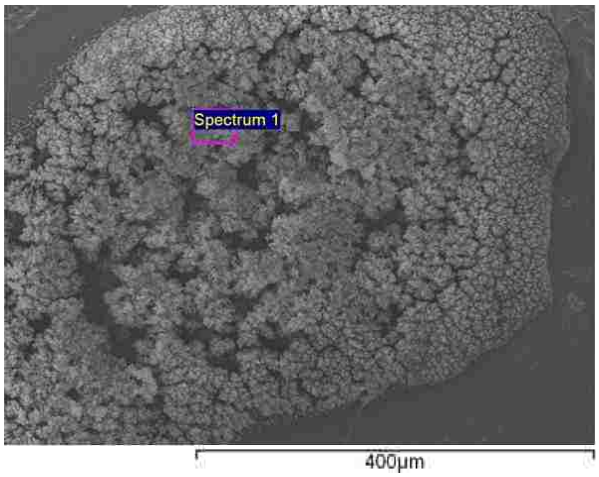

B

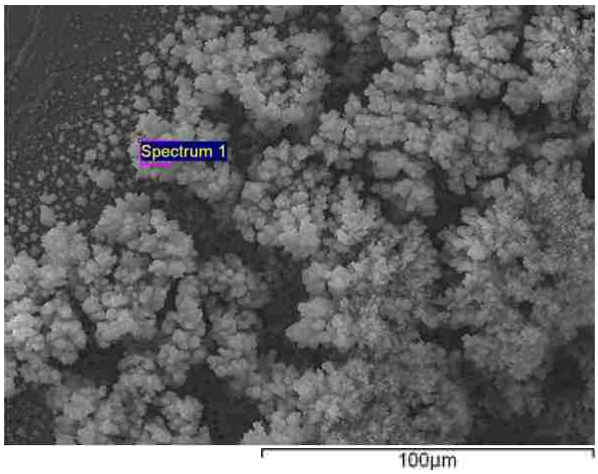

Table C.3 EDS data selected region 1

Element	Wt %	At %
Cu K	69.5	40.0
Fe K	0.20	0.13
P	6.89	8.14
O K	22.4	51.2
Zr	0.96	0.36
Total	100	

Table C.3.1 EDS data selected region 2

Element	Wt %	At %
Cu K	62.2	32.8
Cl K	0.24	0.23
P	7.82	8.47
O K	27.6	57.9
Zr	0.89	0.33
Ta	1.16	0.21
Total	100	

Figure C.3. SEM images of copper coupons treated in water qualities with orthophosphate at pH 9 for 24 h are shown in the top row (**A** and **B**). [A] 600 × 600 µm^2 view; [B] zoom-in view of **A**.

Table C.3 Corresponding EDS analysis for the selected area in **A**.

Table C.3.1 EDS elemental representation analysis of the selected area in **B.**

APPENDIX C. LETTER OF PERMISSION

Order Details

Analytical and bioanalytical chemistry

Billing Status: **N/A**

Order detail ID:	53416217
Article Title:	Investigation of the magnetic properties of ferritin by AFM imaging with magnetic sample modulation
Author(s):	Daniels, Stephanie L.
DOI:	10.1007/S00216-009-2618-Y
Date:	Jan 01, 2009
ISSN:	1618-2650
Publication Type:	e-Journal
Volume:	394
Issue:	1
Start page:	215
Publisher:	Springer-Verlag Berlin/Heidelberg

Permission Status: **Granted**

Permission type: Republish or display content

Type of use: use in a thesis/dissertation

Order License Id: 2645510543382

⊞ View details

Note: This item was invoiced separately through our **RightsLink service.** More info **$ 0.00**

VITA

Stephanie Loletha Daniels was born in Jackson, Mississippi, to her parents, Delois Daniels and Jerry Daniels. She has one sibling, Melanie Daniels and one nephew, Darian Hearn. Stephanie graduated from Wingfield High School in Jackson, Mississippi, in 2000. She continued her education at Jackson State University in Jackson Mississippi, where she graduated with a Bachelor of Science degree in 2004 and Master of Science degree in chemistry in 2006.

In 2006, Stephanie enrolled in the doctoral program at Louisiana State University and A&M College, where she joined Dr. Jayne C. Garno's research group. Stephanie's research included nanoscale measurements of materials using the atomic force microscopy. As a graduate student, Stephanie has published three articles and co-authored five publications. Her work has been presented at local, regional, and international conferences, where she has given three oral presentations, twelve first-author, and nine collaborative poster presentations.

While attending LSU she received several fellowships and awards: The National Science Foundation-Louis Stokes Alliance for Minority Students Bridge to Doctoral Fellowship (LS-AMP/BDP) (2006-2008), Graduate Alliance for Education in Louisiana (GAELA) supplement, the Charles E. Coates and LSU Graduate Student travel awards. In 2009, she completed a ten month internship with the United States Environmental Protection Agency in Cincinnati, Ohio. Her professional affiliations include the American Chemical Society (ACS), the National Organization for the Advancement of Black Chemists and Chemical Engineers (NOBCChE), and Iota Sigma Pi (ISP) National Honor Society of Women in Chemistry. Stephanie will be awarded the degree of Doctor of Philosophy in chemistry from Louisiana State University on May 2011.